Design of a Multifunctional Biomineralized Armor System: The Shell of Chitons

by

Matthew James Connors

B.A., Chemistry & Physics, Rutgers University (2008)

Submitted to the Department of Materials Science and Engineering
in partial fulfillment of the requirements for the degree of

Doctor of Philosophy in Materials Science and Engineering

at the

MASSACHUSETTS INSTITUTE OF TECHNOLOGY

June 2014

Author...
Department of Materials Science and Engineering
May 9, 2014

Certified by..
Christine Ortiz
Morris Cohen Professor of Materials Science and Engineering
Thesis Supervisor

Accepted by...
Gerbrand Ceder
Chair, Departmental Committee on Graduate Students

Design of a Multifunctional Biomineralized Armor System: The Shell of Chitons

by

Matthew James Connors

Submitted to the Department of Materials Science and Engineering on May 9, 2014 in partial fulfillment of the requirements for the degree of Doctor of Philosophy

Abstract

Nature provides many examples of flexible armor systems which may serve as a source of inspiration for materials scientists and engineers. This thesis explores multiscale material and morphological design principles of the shells of chitons (Mollusca: Polyplacophora). The chiton shell consists of eight plates encircled by a structure known as a girdle, which is often covered by scales. The shell provides protection while permitting the flexibility needed to conform to rough substrata, as well as to roll defensively into ball-like conformation to cover its soft ventral side. In typical flat conformations, X-ray micro-computed tomography revealed that the shape and imbrication of the plates results in an overall continuous curvature and constant armor thickness. However, in defensive postures, vulnerable regions exist between the plates due to decreases in plate overlap. In the peripheral scale armor, gradients in the size and overlap of the scales control local levels of flexibility and protection. Scale armor prototypes inspired by the girdle scales were fabricated via multi-material 3D printing. Bending tests demonstrated that the stiffness of the bio-inspired scale armor is highly anisotropic. Remarkably, in certain species, a visual system is integrated within the shell plates. The system contains hundreds of lens eyes, which were found to be capable to forming images. Ray-trace simulations of individual eyes determined that they have a resolution of ~9°, which is consistent with prior behavioral experiments. Unlike the protein-based lenses of most animal eyes, the lenses of chitons, like their shells, are principally composed of aragonite. Chitons are able to tailor the local shape, crystallography, and interfaces of aragonite to achieve a multifunctional armor. However, the integration of lens eyes was found to locally decrease penetration resistance, suggesting a materials-level trade-off between protection and sensation.

Thesis Supervisor: Christine Ortiz
Title: Morris Cohen Professor of Materials Science and Engineering

Acknowledgements

DiNatale, Dr. Alan Schwartzman, Dr. Shiahn Chen, and Dr. Scott Speakman, who were always friendly, knowledgeable, and willing to lend a hand.

I was lucky to have a few incredible roommates during my time at MIT. I am deeply indebted to them for their friendship and support. Thank you Dr. Chris "Little Richy" Ng, Dr. Sam "Jackson" Crawford, my partner in crime in DMSE, Dr. Bill "BP3" Polacheck, our resident lumberjack, and Dr. Alain "AAron" Bauza, a great friend since sixth grade. I will miss our apartment on Webster Avenue and all of our adventures. I thank my first year roommate and fighter pilot Karl Suabedissen for all the free trips between NJ and Boston at light speed. I am also very fortunate to have a great network of friends beyond MIT, and I look forward to reuniting with some of you in NY/NJ.

I would also like to thank Dr. Chris Pirie, Dr. Andrej Kosmrlj, and all former and current players and coaches of the MIT club soccer team. I had a blast training and playing alongside you all.

Finally, I express my deepest gratitude to my family and girlfriend whom I have been dearly missing and am looking forward to spending more time with after graduation. I thank my brother and sister, Stephen and Shannon, for their support. I thank my mother, Abigail, for her love, and my father, Thomas, for his unyielding encouragement. I thank my mahal Elaine for her patience and biweekly refuge.

"I do not know what I may appear to the world, but to myself I seem to have been only like a boy playing on the sea-shore, and diverting myself in now and then finding a smoother pebble or a prettier shell than ordinary, whilst the great ocean of truth lay all undiscovered before me."[1]

Sir Issac Newton (1643 – 1727)

Table of Contents

8

List of Figures

13

List of Tables

1 Introduction

1.1 Motivation

Nature provides a multitude of materials with a variety of different functions which may serve as a source of inspiration for materials scientists and engineers[2]. Compared to the diverse range of engineering materials used today, biological materials consist of relatively few constituent elements. Nevertheless, nature has developed ways, through the process of evolution, to combine these elements to create a wide range of polymers, minerals, and composites with extraordinary functional properties. The fundamental design aspect of biomaterials is their hierarchical structure extending from the nano- to macroscopic length scales[3,4].

One particularly active and fruitful area of biomaterials research over the last fifteen years has been elucidating the design principles of natural armor materials[5,6]. On the materials level, the mechanical properties of natural armor are often amplified by orders of magnitude relative to abiogenic forms of their major constituents, brittle ceramics and compliant macromolecules[7]. The structural origins of the deformation mechanisms which enable this mechanical property amplification have been comprehensively investigated in a few model systems[8,9,10,11]. From an engineering perspective, the ultimate goal of this research is to combine the hierarchical architectures of natural armor materials with advanced synthetic materials to create new state-of-the-art structural and/or protective composites. One well-studied armor material, nacre of mollusk shells, has already inspired the construction of a number of biomimetic composites[12,13].

On the macroscopic scale, there has recently been renewed interest in biomimetic scale armor[14,15,16,17,18], which can provide protection while permitting some desired degree of flexibility. Scale armor was used by humans at some point in the history of most civilizations[19]. The flexibility and tailorability of scale armor enabled it to be used to construct a variety of protective elements for different parts of the body including the head, neck, torso, and extremities[20]. In the animal kingdom, scale armor can be found in an evolutionarily diverse range of organisms such as pangolins[21], fish[5], snakes[22], and even snails[23]. Both ancient synthetic and natural scale armor share the same basic design: many hard armor units attached to each other and/or a soft underlying layer by compliant fibers. Not surprisingly, ancient soldiers and animals faced similar types of mechanical threats such as blunt impacts, sharp impacts, cuts, and stabs. Clearly, the materials used to construct the individual units of ancient human scale armor, predominantly metals[20], are mechanically far superior to the biological polymers and

ceramics of natural analogues. However, the geometrical complexity of natural scale armors in terms of the shape of the individual armor units, their inter-connections (joints), and overlap between units, far exceeds that of the most sophisticated human body armors from all time periods. Moreover, these geometrical aspects are often spatially varied in natural systems to control local levels of protection and flexibility. One objective of biomimetic scale armor research is to explore the aforementioned geometrical aspects of natural armor and identify design principles which can be translated into advanced human body armor. As the fabrication methods of ballistic ceramics and composites improve, we may see a return of human scale armor designed to provide adjustable levels of flexibility/mobility and protection.

One remarkable aspect and perhaps defining characteristic of structural biological materials and systems is their multifunctionality. Numerous examples of biomaterial systems which serve two or more diverse functions have been investigated[24], although this area remains largely unexplored. These natural systems may provide efficient solutions for engineering problems with similar sets of functional requirements and design constraints. In this context, biomaterial systems with functions which engineers commonly assume to contradict each other are of particular interest[25]. From an armor perspective, these may be conflicting mechanical properties (e.g. high strength and toughness[26]) or a combination of a mechanical and a non-mechanical function (e.g. multi-hit capability and optical transparency[11]).

Biomineralized armors, possessing both high strength and damage tolerance, have long been known to be an example of the first scenario. In addition to mechanical robustness, a number of unique biomineralized armors have been reported to exhibit exotic optical properties (Table 1-1). These armors fall into the second class (or perhaps both classes) of biomaterials with conflicting functions. The multifunctional armor systems can be classified into two groups based on the integration of their optical elements. In the first group (A), the armor is a relatively homogeneous material, i.e. the cross-sectional microstructure is uniform. In this case, there is no spatial separation of optical and mechanical functions. In the second group (B), the armor is inhomogeneous. The regions of the shell which serve optical roles differ in geometry and/or constitutive materials compared to the bulk, which is responsible for mechanical robustness. Group B can be further partitioned into two subgroups depending on whether the regions of functional integration are localized (B1) or dispersed over a large area of the shell (B2).

Only about half of the studies referenced in Table 1-1 reveal the relationship between the structure of the armor and the resulting optical property. Furthermore, only L. Li and C. Ortiz[27] take a holistic approach which examines the relationship between the structure and both the resulting optical and mechanical properties. This is a promising

area of materials research since it allows the exploration of how organisms can use one homogeneous protective material for multiple functions (A), or manipulate the same set of constitutive elements to create and integrate different functional elements within one system (B).

Species	Phylum: Class	Calcareous Biomaterial	Optical Property	Proposed Function	Homogeneous Material (A) Integrated Elements (B) Localized (B1) Dispersed (B2)	Ref.
Phacops rana	Arthopoda: Trilobita	Calcite	Focusing via lenses	Spatial Vision (Compound eyes)	B1	28
Notodromas monachus	Arthopoda: Ostracoda	Calcified Cuticle	Focusing via lenses	Photoreception	B1	29,30
Ophiocoma wendtii	Echinodermata: Stelleroidea	Calcite	Focusing via lenses	Photoreception	B2	31
Hinea brasiliana	Mollusca: Gastropoda	Unknown Polymorph of $CaCO_3$	Wavelength-specific diffusion	Communication	A	32
Haliotis glabra	Mollusca: Gastropoda	Aragonite	Photonic color	-	A	33
Patella pellucida	Mollusca: Gastropoda	Calcite	Photonic color	Camouflage via biomimicry	B1	34
Notoacmea persona	Mollusca: Gastropoda	Unknown Polymorph of $CaCO_3$	Translucence	Photoreception	B2	35,36
Corculum cardissa	Mollusca: Bivalvia	Unknown Polymorph of $CaCO_3$	Focusing via "windows" / lenses	Light transmission to endosymbiotic dinoflagellates	B2	37,38
Placuna placenta	Mollusca: Bivalvia	Calcite	High transmittance	Camouflage via transparency	A	27
Acanthopleura granulata	Mollusca: Polyplacophora	Aragonite	Focusing via lenses	Spatial Vision	B1	39

Table 1-1│ Biomineralized armor systems with optical functions.

1.2 Overview

This thesis investigates the material and morphological design principles of a natural multifunctional armor system, the shell of chitons (Mollusca: Polyplacophora). Chitons provide us with a beautiful example of two completely different natural armor designs, with differing levels of protection and flexibility, seamlessly integrated together in one system. The chiton shell consists of eight central plates encircled by a structure known as a girdle, which is often covered by scales. In addition to providing protection, the plates contain a sensory system which is capable of optically detecting threats. In the next section of the introduction, 1.3, I provide additional background information on chitons, including details of their habitat and predators.

The main content of this thesis is organized into four chapters. In chapter 2, I examine the structure and composition of the shell plates of the chiton *Tonicella marmorea*. The plates contain many layers with different microstructures, and their protection mechanisms are discussed. Chapter 3 focuses on the structure/property/performance relationships of the visual system integrated within the plates *Acanthopleura granulata*. Spatial vision is enabled by aragonite-based lens eyes, which we demonstrate to be capable of image formation. To achieve functional integration, *A. granulata* tailors the local geometry, crystallography, and interfaces of its armor material, aragonite. However, as the size and complexity of the integrated sensory elements increases, the local mechanical performance of the armor decreases. In chapter 4, I explore the larger length scale armor design principles of the shell plates of the chiton *Tonicella marmorea*. When threatened, *T. marmorea* is able to defensively roll into a ball-like conformation to cover its soft ventral side. However, this posture creates vulnerable regions between the plates. Chapter 5 elucidates the multiscale armor design principles of the scale armor which covers the girdles of some species of chitons. Chiton scale-inspired armor prototypes were fabricated via multimaterial 3D printing. Bending tests indicate that the bending stiffness of chiton scale armor is highly anisotropic.

1.3 Background Information on Chitons

Chitons (Polyplacophorans) are marine mollusks found worldwide in all seas with more than 940 extant[40,41] and 430 fossil[42] species which extend to the late Cambrian[43], about 500 million years ago. They are one of the earliest diverging groups of living mollusks and are often referred to as "living fossils" since their body plan has not significantly changed for over 300 million years[44]. They are typically oval in shape, bilaterally symmetric, and generally range from a few millimeters to 15 cm in length[45]. The largest species, *Cryptochiton stelleri*, can grow over 30 cm in length and live around 25 years[46]. The habitats of chitons range from the splash zone (e.g. *Acanthopleura*) to deepest parts of the ocean (e.g. *Ferreiraella*)[47].

Chitons generally live on hard substrata[47], which they adhere to using the suction of their broad muscular foot. They are notoriously hard to pry off rocks when stationary. In response to perceived threats, a chiton will rapidly clamp down on the substratum with its foot and girdle[48]. Forward and backward motion is produced by waves of muscular contraction that sweep along the foot[49,50]. A chiton can also pivot laterally by rotating the anterior half of its foot in one direction, and the posterior half in the opposite direction[51]. The average speed of movement ranges between approximately 1-15 mm/min depending on the species and degree of stimulation[52,53,54]. The fastest recorded speed was 30 mm/min over a period of 3 minutes by *Acanthopleura gemmata*[52].

From a materials perspective, chitons are perhaps best known for their teeth, which have provided many insights into the biological processes which control mineralization[55]. The teeth are arranged in a conveyor belt-like structure known as the radula, which is generally used for scraping algae off of rocky surfaces. In 1962, H. Lowenstam, realizing that the teeth should be harder than the substrate, discovered that they are capped with a hard iron oxide mineral called magnetite[56]. A recent study found that these abrasion-resistant magnetite teeth are self-sharpening, and exhibit the largest hardness (9-12 GPa) and stiffness (90-125 GPa) of any biogenic minerals to date[57]. For comparison, the magnetite cap of chiton teeth is about three times harder than human enamel (3.2-4.4 GPa[58]).

Figure 1-1| Wide-field scanning electron microscopy image of the dorsal side of chiton *Rhyssoplax canariensis* overlaid with a light micrograph. The chiton is approximately 2 cm in length. The image was taken with Dr. James Weaver at the Wyss Institute for Biologically Inspired Engineering at Harvard University.

1.3.1 The Shell

As seen in Fig. 1-1, the chiton shell primarily consists of eight overlapping arch-shaped dorsal plates. With the exception of the head plate, each plate has two anterior projections, the apophyses, which underlie the preceding plate[59]. The plates provide protection while still allowing for the flexibility needed to conform to uneven surfaces and to roll defensively into a ball-like conformation. Similar defensive enrolling behaviors are found in a number of animals with exoskeletons including isopods[60], trilobites[61] (extinct), pangolins[62], three-banded armadillos[63], and the armadillo lizard[64]. Enrollment provides immediate coverage and protection of the soft ventral side of the animal, and may facilitate a rolling escape mechanism if the animal is near a slope[65] or water current[66].

The eight dorsal plates of chitons are surrounded by a tough tissue known as the girdle[45]. The dorsal surface of the girdle is often covered by aragonite-based scales (Fig. 1-1), spines, or spicules[59]. The ventral surface is also frequently covered with scales. Despite these rigid elements, the girdle is flexible enough to conform to rough surfaces, as well as to locally wrinkle to form channels that allow water to circulate over the ctendia during respiration[67]. The organization, morphology, and fine structure of the

dorsal girdle scales vary between species and are often used as a taxonomic aid[68]. In some species, the scales overlap significantly[59,69,70]. In a comprehensive study of the genus *Chiton*, R. Bullock provides scanning electron microscopy images of individual scales that have been removed from the girdle[71]. These images reveal that although the scales appear as overlapping discs from above, the lower half of each scale is shaped like a rhombic prism. The transition from the prismatic base to the rounded overlapping upper region creates a "hook" shape.

1.3.2 Evolutionary Stages of Chiton Shell Development

The shells of the first chitons, which likely appeared around the end of the Cambrian period, consisted of several separate spine-like plates[72]. Fossil records indicate that the shell progressed through three distinct evolutionary stages. The first stage was the flattening of the shell, which occurred between the late Cambrian and Devonian periods. B. Sirenko suggests that this was a consequence of increasing predation pressure and the need to hide in narrow refuges[72]. The second stage of development occurred in the Lower Carboniferous. It was here that a new layer of the shell plates, the articulamentum, appeared and plate overlap increased[43]. In modern chitons, the articulamentum forms the apophyses, two anterior projections, and the insertion plates, extensions which connect the plates to the surrounding girdle. B. Sirenko hypothesizes that the development of the articulamentum facilitated an increase in muscle complexity which strengthened the connections between the shell plates, as well as the connections between the shell plates and the girdle. These developments likely increased mobility, enhanced the ability to firmly attach to substrata, and improved defensive capabilities[72]. The third and final stage began at the end of the Jurassic period, and is characterized by the development of the integrated sensory organs, the aesthetes.
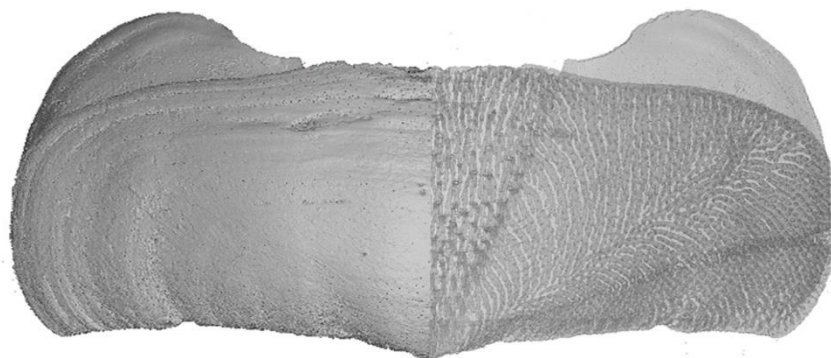
Figure 1-2 | 3D synchrotron micro-computed tomography reconstruction of an intermediate plate of the chiton *Tonicella marmorea*. left half, Dorsal view of the plate. **right half**, Dorsal view with a transparency effect which highlights the interior porosity created by the aesthetes. The plate is ~4.5 mm wide.

1.3.3 The Integrated Sensory Organs

Chitons are the only known group of extant mollusks to have living tissue integrated within the outermost layer of their calcium carbonate-based shells[73]. This tissue fills a complex network of channels (Fig. 1-2) that open dorsally as thousands of sensory and/or secretory organs known as aesthetes[74]. The earliest known description of the aesthete channels was in 1847 by A. von Middendorff[75], who observed pores passing through the entire thickness of intermediate plates in what is now referred to as the jugal area. In 1869, W. Marshall described the bulbous superficial sensory structures (megalaesthetes), which stem from larger channels[76]. About 15 years later, H. Moseley published a detailed account of the aesthetes, complete with beautiful and incredibly accurate illustrations[77]. Most importantly, he discovered that in certain species, the aesthetes contain eyes which each contain a biconvex lens. Remarkably, above the lens, he was able to observe a concavo-convex corneal layer which was circumferentially continuous which the outer shell layer. He correctly identified the cornea as calcareous, but mistakenly deduced that the lenses were composed of soft tissue. In 1907, M. Nowikoff determined that the lenses were probably calcareous, and observed that they were strongly birefringent when viewed with polarized light[78]. His colored illustrations of the cross-sectional structure of the eyes are stunning and my own (seen Chapter 3) pale in comparison. It was not until 1969 that P. Boyle confirmed the presence of photoreceptors in the chambers of the eyes[79]. Recently, in 2011, D. Speiser et al. established that the lenses are composed of aragonite and facilitate spatial vision[80].

Although non-eye aesthete structures have been investigated for well over 100 years, their function remains a matter of debate[81]. J. Blumrich originally proposed a photosensory role 1891[82], and subsequent observations of the phototactic behavior of a number of species[83,84,85] support this hypothesis. Alternative proposed functions include mechanoreception[77], chemoreception[86], production of the periostracum[78], and production of secretions for protection from predators, fouling, and/or desiccation[86]. It is possible that the aesthetes have different functions in different lineages of chitons[74]. Regardless, the high density of aesthetes in the outer shell layer suggests that they are crucial to survivability.

1.3.4 Predators

Chitons have wide variety of known predators including fish[87], lobsters[88], crabs[89], octopi[90], snails[91], starfish[92], and birds[93]. Types of predatory attacks include biting (fish and spiny lobsters), pinching with claws (crabs), drilling (octopi and snails), and insertion of the cardiac stomach underneath or between the shell plates (starfish).

2 Multilayered Structure and Composition of the Armor Plates

This chapter was published as an article in *The Journal of Structural Biology* in 2012[94].

2.1 Introduction

A critical function of natural armor is mechanical protection from predatory attacks including penetration, fatigue, drilling, peeling, and crushing[95]. Resistance to these damaging attacks is provided by the internal, multilayered microstructure of the individual armor units[9]. The principal armor units of chitons, the shell plates, are known to possess one of the most complex multilayered structures seen in Mollusca[96]. The multilayered structure of chiton plates from a number species have been studied[97,98,99,100,101,102,103,104,105,106]. In addition to the periostracum, a thin outer organic layer that is often eroded away on older shells, chiton plates are generally composed of approximately seven aragonite-based[107] layers as follows (described from outer to inner):

1) *Tegmentum*: a granular of irregular simple prismatic layer that contains the aesthetes, an intricate network of tissue-filled channels which open at the dorsal surface as thousands of sensory organs[74].

2) *Dorsal Mesostracum*: a thin crossed-lamellar layer that may be divided dorsoventrally into two sub-layers by a row of aesthete channels.

3) *Articulamentum*: a composite prismatic layer that constitutes that bulk of the apophyses and insertion plates.

4) *Ventral Mesostracum*: a crossed lamellar layer. The dorsal and ventral mesostracum layers are collectively referred to as the *Pallial Myostracum*.

5) *Anterior Myostracum*: a granular or irregular simple prismatic layer which lies in the impression of the transverse muscle.

6) *Hypostracum*: a crossed-lamellar layer that constitutes the bulk of the central callus.

The objectives of this study were: 1) to investigate the composition of the inorganic and organic components of the shell plates, 2) to determine the spatial distribution of the layers present in the intermediate plates, 3) to determine the orientations of the microstructures relative to the macroscopic geometry of the plates, and 4) to elucidate relationships between the internal layers and microstructures of the plates and larger length scale geometric design aspects to better understand the balance between threat protection and flexibility/mobility. To achieve these goals, the shell of the chiton

Tonicella marmorea (Fig. 4-1) was analyzed by a variety of materials characterization techniques. The microstructure of individual intermediate plates was characterized via mercury porosimetry, optical microscopy, scanning electron microscopy (SEM), and X-ray diffraction (XRD). Fourier-transform infrared spectroscopy (FTIR) and amino acid analysis (AAA) were used to identify and compare the composition of organic materials from the girdle, plates, and inter-plate regions. The results expand our current knowledge of evolutionary designs of biomineralized structural materials, and hold potential to inspire developments in the design of advanced load-bearing and/or protective engineering materials[108].

2.2 Materials and Methods

2.2.1 Sample Preparation and Terminology

Tonicella marmorea were purchased alive from Gulf of Maine, Inc. (Pembroke, Maine) and stored frozen until experimentation. Individual plates were carefully separated using forceps and razor blades. Plates were cleaned by sonication (Branson 1510, Danbury, CT) in deionized water twice for 45 seconds.

The chiton shell plate layer nomenclature used was developed by J. Bergenhayn[97], and G. Laghi and F. Russo[100]. The Molluscan microstructure terminology used was defined by J. Taylor and M. Layman[109], or J. Carter and G. Clark[110].

2.2.2 Optical Microscopy and Scanning Electron Microscopy (SEM)

For cross-sectional imaging, plates were embedded in a fast cure epoxy (Loctite, USA) and sectioned with a diamond impregnated saw (Buehler Isomet 5000, Lake Bluff, IL) at 875 rpm. Sectioned samples were polished stepwise with aluminum oxide pads with roughness varying from 9 to 0.1 μm (South Bay Technologies, CA), and then with 500 nm silica nanoparticles on microcloth (Buehler, IL). Some samples were slightly etched with 0.5 M EDTA for 5 min to improve contrast between microstructurally distinct layers. Additionally, some plates were cryofractured by immersing them in liquid nitrogen for 5 min and then breaking them with a hammer. Light micrographs were taken with a Nikon ECLIPSE LV100 optical microscope (Tokyo, Japan). Cross-sectional SEM samples were fixed on a steel support using conductive tape, and then sputter-coated with ~5 nm of gold–palladium in a Denton Vacuum Desk II (Moorestown, NJ). A JEOL JSM 6700 (Peabody, MA) scanning electron microscope was used for imaging at an acceleration voltage 10 kV. Demineralized SEM samples were secured in a holder, covered with carbon for 1 min using an Edwards S150B sputter coater (West Sussex,

United Kingdom) and imaged with an ESEM XL 30 Philips (Amsterdam, Netherlands) or a LEO DSM 982 Gemini (Oberkochen, Germany) scanning electron microscope.

2.2.3 Thermogravimetric Analysis (TGA)

Plates were lightly ground with a pestle and mortar. Samples were then vacuum dried at 110 °C overnight to remove residual water. TGA was carried out from 110 to 500 °C at 2.5 °C/min on a TA Instruments TGA Q50 (New Castle, DE). Weight loss due to the combustion of organic materials was attributed to the temperature range 110–475 °C[111,112].

2.2.4 Mercury Porosimetry

The volume percent porosity of three intermediate plates was measured by a mercury porosimeter (Autopore IV 9500, Micromeritics, USA), which was operated at pressures between 3.7 kPa and 14 MPa, corresponding to pore diameters of 404 and 0.107 µm, respectively. A standard contact angle of 140°, which was used previously by P. Gane. et al. to study the porosity of calcium carbonate structures[113], was assumed in the pore size calculations.

2.2.5 X-ray Diffraction (XRD)

The mineral phase of the plates was verified using a Philips PANalytical X′ Pert PRO diffractometer (Netherlands) with CuKα radiation, operating at 45 kV and 40 mA between 10° and 70° (2θ).

2.2.6 Chitin Isolation and Staining

The organic matrix of chiton plates was isolated by decalcification using a 3 M HCl solution as well as a 7.4 pH Osteosoft (Merck) solution at room temperature. The procedure was monitored using stereo, light, and fluorescence microscopy (BZ-8000, Keyonce, Japan). Immersion of the isolated organic matrix, inter-plate material, and girdle in 2.5 M NaOH at 37 °C led to an immediate loss of brownish pigment and proteins from these specimens. The fibrous colorless materials were then washed with distilled water five times, dialyzed against deionized water on Roth (Germany) membranes with a molecular weight cut-off (MWCO) of 14 kDa for 48 hours at 4 °C, and finally dried at room temperature. Calcofluor White (Fluorescent Brightener M2R, Sigma) was used to confirm the presence of chitin. Samples were placed in a 0.1 M Tris–HCl solution at pH 8.5 for 30 min, stained using a 0.1% Calcofluor White solution for 30

min in darkness, rinsed five times with deionized water, dried at room temperature, and finally observed using fluorescence microscopy[114].

2.2.7 Fourier-Transform Infrared Spectroscopy (FTIR)

Infrared spectra were recorded on a Nicolet 210 FT-IR Spectrometer. Two hundred and fifty scans were recorded at a spectral resolution of 2 cm^{-1}. All spectra were baseline corrected with a two-point linear baseline at 845 and 1890 cm^{-1}. An α-chitin standard from the demosponge *Ianthella basta* was used as a control[115].

2.2.8 Amino Acid Analysis (AAA)

Dry cleaned plates were ground with a pestle and mortar and weighed. The fine powder was suspended in deionized water. In a demineralization step, stoichiometric amounts of 1 M HCl were added dropwise to the solution over the course of 2 days. After complete demineralization, the solution was centrifuged (3000 rpm, 10 min, Eppendorf Centrifuge 5804 R) to separate soluble material from the insoluble, precipitated material. The soluble material was dialyzed exhaustively (Spectra Pro 7 dialysis membranes, 3500 MWCO, part #132112) to remove salts and small molecules. The insoluble material was lyophilized and dried overnight in a vacuum oven at 50 °C. Samples were hydrolyzed for AAA, which was performed using a Waters system with Breeze software by Bio-Synthesis, Inc. (Lewisville, TX).

2.3 Results

2.3.1 The Multilayered Structure of Individual Armor Plates

The intermediate plates of *T. marmorea* are composed of six aragonite-based layers (Fig. 2-1). The dorsal mesostracum was not observed in any plates used in this study, so we refer to the ventral mesostracum simply as the mesostracum. Fig. 2-1a and b contain representative longitudinal and transverse cross sections, which are accompanied by schematic diagrams which illustrate the spatial distribution of the six layers. The key to the schematics (Fig. 2-1d) relates the textures and colors to the microstructures and layers.
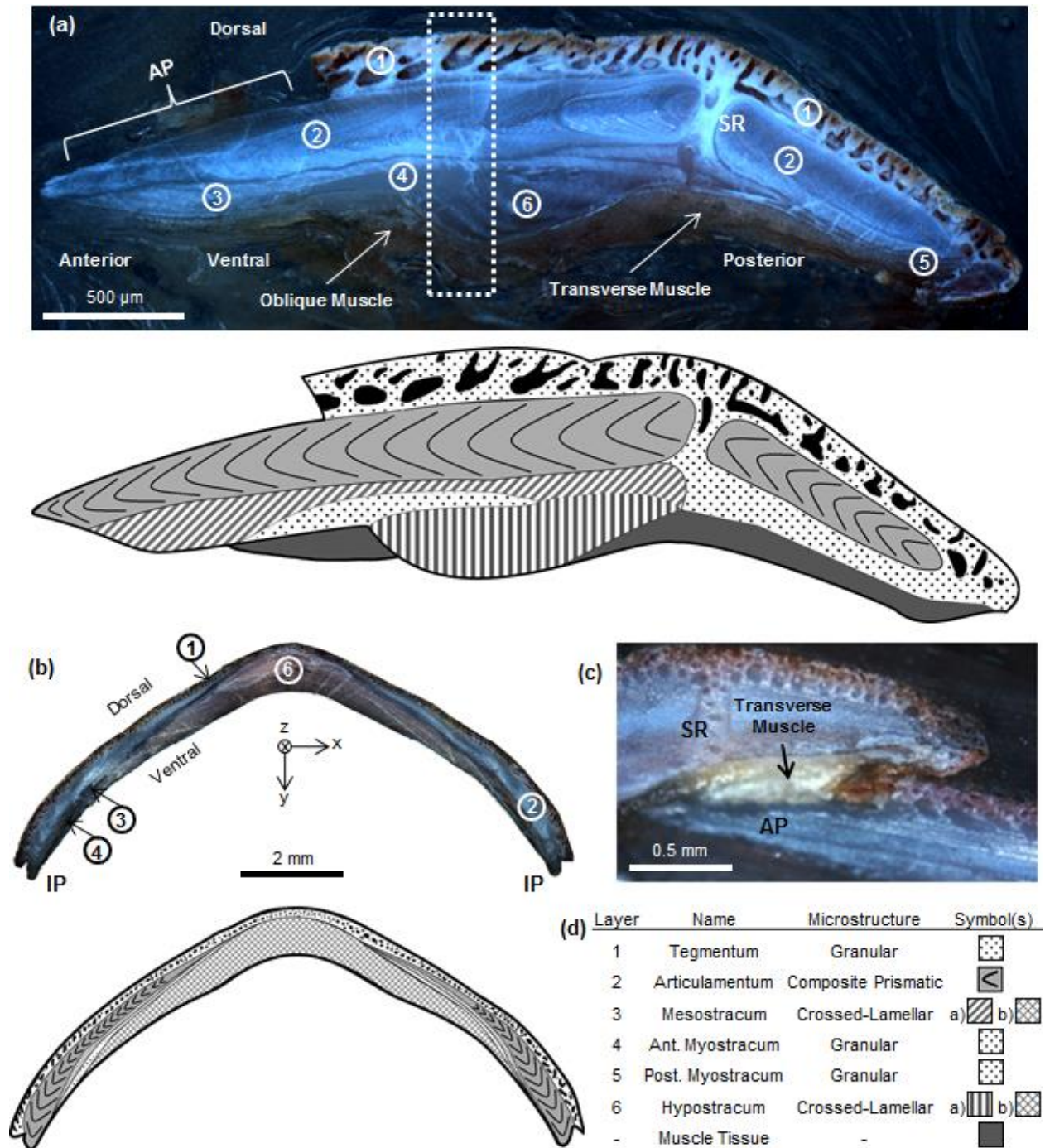
Figure 2-1 | Cross-sectional structure of the intermediate armor plates of the chiton *Tonicella marmorea* via dark field light microscopy. **a** and **b**, Composite images of polished longitudinal and transverse, respectively, cross sections and complementary schematic diagrams. **c**, Longitudinal cross-section displaying the transverse muscle between two adjacent intermediate plates. **d**, Table relating colors and textures of the schematics to layers and microstructures. Abbreviations: AP, apophyses; IP, insertion plate; SR, slit ray.

The outermost layer of the intermediate shell plates, the tegmentum, has a uniform thickness of 155 μm and is infiltrated with the aesthete canal system (Fig. 2-1a), which constitutes ~7.5% of each plate by volume, as measured by mercury porosimetry. Main aesthete channels in the tegmentum run roughly longitudinally and are separated by ~20 μm. They each have a diameter of ~40 μm, which lies in the lower end of the range (40–75 μm) found across the genus *Tonicella*[74]. Scanning electron microscopy revealed that the tegmentum has a fine-grained homogeneous microstructure (Fig. 2-2b and g). X-ray diffraction of the dorsal shell surface found no preferred grain orientations (Fig. 2-3a). Grains are approximately 1 μm in diameter, but are slightly elongated along one axis ventrally, below the main aesthete channels. Slit ray and jugal aesthete channels that begin in the tegmentum, pass though the underlying layers, and exit on the ventral shell surface are insulated by a fine-grained homogeneous layer which is a couple of microns thick. Posteriorly, the tegmentum folds underneath the plate and becomes the posterior myostracum (layer 5), which lies in the impression of the transverse muscle (Fig. 2-1a). The transverse muscle, which runs longitudinally from the anterior eave of the tegmentum to the tip of the apophyses, fills the gap between overlapping plates and binds them together (Fig. 2-1c). The thickness of the transverse muscle ranges from ~100 to ~250 μm.

The second layer, the articulamentum, has a composite prismatic microstructure (Fig. 2-2c and h). Bundles of prisms fan out dorsoventrally from the center of the layer. The length of the prism bundles ranges from approximately 3 to 10 μm. Individual building blocks are shaped like square prisms with an edge length of ~300 nm. The thickness of the articulamentum ranges from 0 mm in the jugal area to ~0.9 mm laterally, in the insertion plates.

The articulamentum is followed by the mesostracum, which has a simple crossed-lamellar microstructure (layer 3) (Fig. 2-2d and i). It branches off from the hypostracum near the body diagonal, along which the slit ray aesthete channels run (Fig. 2-1a). The long axes of the first order lamellae are oriented at approximately a 45° angle relative to the ventral plate surface, and are 1-2 μm wide. The layer lacks well-defined second order lamellae. Third order lamellae are shaped like square prisms and have approximate dimensions 15 × 0.3 × 0.3 μm. Thus, each first order column is about 3-6 third order lamellae wide. The angle between sheets of third order lamellae in adjacent first order columns is ~40°. Third order lamellae on the interface between adjacent first order columns possess a "wavy" surface topography, which has a wavelength approximately equal to their width (~300 nm) (Fig. 2-2i, inset). The periodic surface elevations on one side of the interface align with surface depressions on the opposite side.
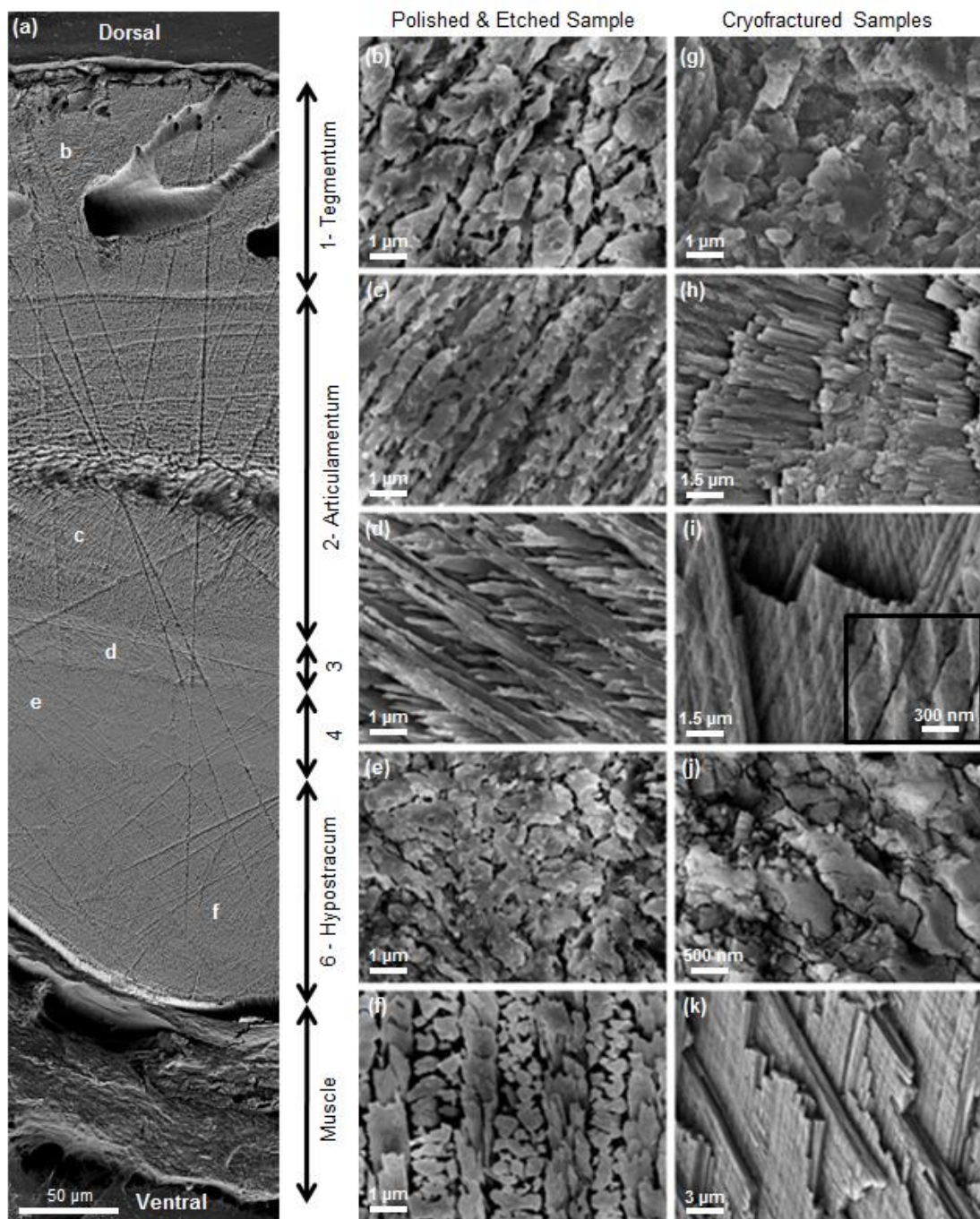
Figure 2-2| Microstructure of the intermediate armor plates of the chiton *Tonicella marmorea* via scanning electron microscopy. a, Composite image of the boxed region (formed by white dashes) of the longitudinal cross section of Fig. 2-1a, which was etched with 0.5 M EDTA for 5 min to increase contrast. (**b-f**) correspond to magnified regions of (a) and preserve microstructure orientation relative to the geometry of the cross section. (**g-k**) were obtained from cryofractured samples, preserving the true form of each microstructure. **b** and **g**, Tegmentum (layer 1, granular). **c** and **h**, Articulamentum (layer 2, composite prismatic). **d** and **i**, Mesostracum (layer 3, crossed-lamellar). **e** and **j**, Anterior myostracum (layer 4, granular). **f** and **k**, Hypostracum (layer 6, crossed-lamellar).

31

The anterior and posterior myostracum, layers 4 and 5, respectively, both have a fine-grained homogeneous microstructure with grains roughly 1 μm in diameter (Fig. 2-2e and j). The anterior myostracum stems from the impressions of the oblique muscles while the posterior myostracum lies in the impression of the transverse muscle. Together, the articulamentum, mesostracum, and anterior myostracum form the apophyses (Fig. 2-1a). The bottom layer, the hypostracum, has a simple crossed-lamellar microstructure identical to that of mesostracum, except that the long axes its first order lamellae are oriented perpendicular to the ventral plate surface (Fig. 2-2f and k). This was supported by XRD of the ventral shell surface, which found two preferred orientations corresponding to the two lamellar dip directions (Fig. 2-3a). First order columns often slightly deviate from the perpendicular orientation, become thinner and disappear, or become thicker and branch. In transverse cross sections, the thickness distribution of the hypostacum is the inverse of that of the articulamentum; the hypostracum is approximately 0.9 mm thick in the jugal area and absent laterally, at the start of the insertion plates (Fig. 2-1b). Longitudinally, the hypostracum composes the bulk of the central callus and is absent from the apophyses and insertion plates.
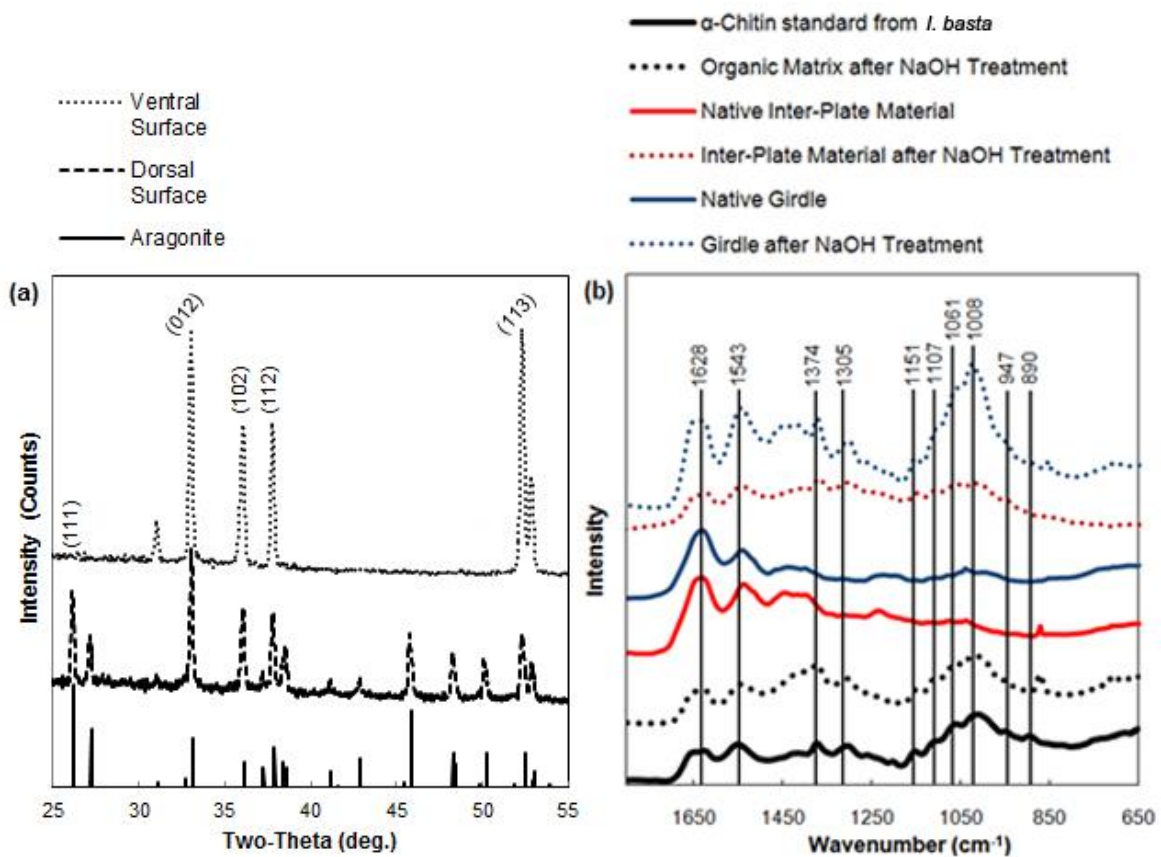
Figure 2-3 | Chemical composition of the plates of the chiton *Tonicella marmorea*. a, X-ray diffraction patterns of the dorsal and ventral surfaces of an intermediate plate. **b**, Infrared spectra of the intra-plate organic matrix, girdle, and inter-plate material before and after NaOH treatment to remove proteins.

2.3.2 Composition of the Intra-, Inter-, and Ambi-Plate Organic Materials

The intermediate plates of *T. marmorea* were determined to have an organic matrix content of ~2.6 weight percent (aragonite content of ~97.4 weight percent) by thermogravimetric analysis. The organic matrix, which was obtained after a 24 h gentle demineralization using Osteosoft™ solution at room temperature, showed a strong resistance to alkali treatment (Fig. 2-4a). It remained stable after submersion in 2.5 M NaOH at 37 °C for 30 days. The girdle and inter-plate material displayed similar properties. After alkali dissolution of their proteinaceous components, Calcofluor White staining (Fig. 2-4b) and FT-IR spectroscopy (Fig. 2-3b) indicated the presence of α-chitin within the shell plate organic matrix, girdle, and inter-plate material. Amino acid analysis of the intra-plate organic matrix revealed that the amount of protein in the shell plates is approximately ~0.17% by weight (Fig. 2-5b).

Figure 2-4| Organic matrix of the plates of the chiton *Tonicella marmorea*. a, Light micrograph of the organic matrix of the head plate after demineralization with HCl for 1 hour. **b,** Fluorescence micrograph of the organic matrix after complete decalcification with Osteosoft™, NaOH treatment to remove proteins, and Calcofluor White staining. **c,** SEM image of the organic matrix after partial decalcification with Osteosoft™.

Amino Acid Composition

(a)
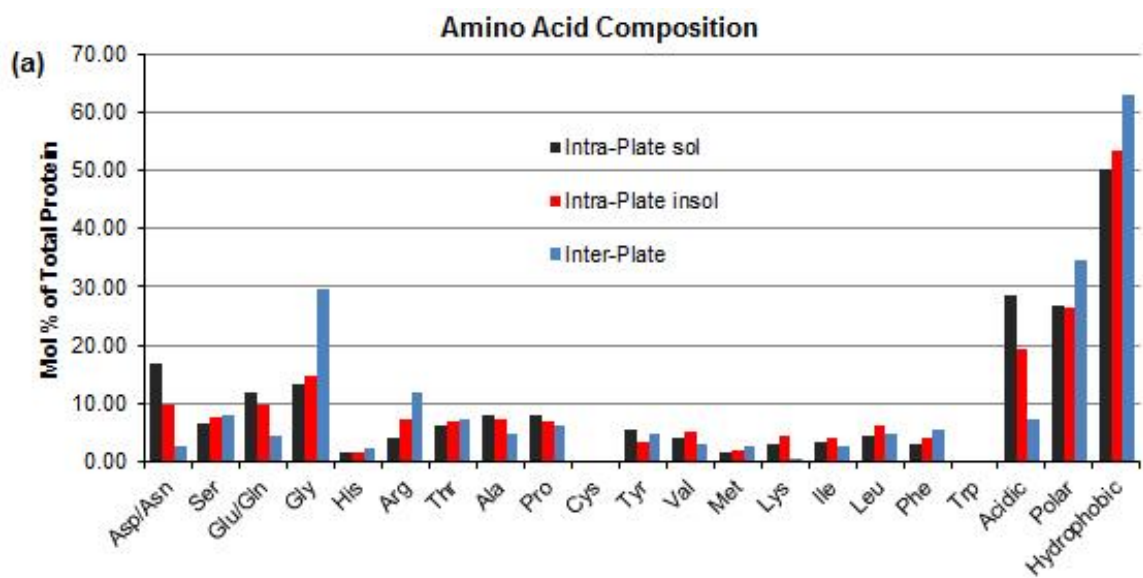
Amino Acid	Intra-Plate		Inter-Plate
	sol	insol	
Asp/Asn	16.64	9.63	2.73
Ser	6.53	7.56	7.97
Glu/Gln	11.81	9.73	4.51
Gly	13.24	14.50	29.74
His	1.63	1.38	2.25
Arg	4.06	7.22	11.99
Thr	6.02	6.87	7.18
Ala	8.08	7.23	4.64
Pro	7.93	6.98	6.01
Cys	0.00	0.00	0.00
Tyr	5.51	3.27	4.60
Val	3.91	5.06	2.89
Met	1.39	1.83	2.45
Lys	3.02	4.28	0.45
Ile	3.14	4.00	2.45
Leu	4.27	6.32	4.83
Phe	2.83	4.15	5.32
Trp	0.00	0.00	0.00
Acidic	28.4	19.4	7.2
Polar	26.8	26.3	34.4
Hydrophobic	50.3	53.3	62.9
wt% protein relative to plate	0.036	0.13	
	0.17		
wt% protein relative to organic matrix	6.7		4.8

(b)

Figure 2-5 | Amino acid composition of the proteins of the intra-plate organic matrix and inter-plate material of the chiton *Tonicella marmorea*. a, Bar graph comparing the amino acid composition of the soluble and insoluble proteins. **b**, Table including the weight percentage of intra-plate organic matrix proteins relative to the matrix and entire intermediate plate.

34

2.4 Discussion

2.4.1 Comparison of the Shell Microstructures of Chitons and Mollusks

The mesostracum was originally named by J. Bergenhayn[97] for its position between the tegmentum and articulamentum in *Acanthopleura spinigera*. He observed that it was similar in structure to the hypostracum, which is now recognized as having a simple crossed-lamellar microstructure. The mesostracum has been observed lining both the dorsal and ventral sides of the articulamentum in *Chiton olivaceous*[100,103], *Leopidopleurus cajentanus*[101], *Liolophura gainardi*[103], and *Liolophura japonica*[106]. However, I only observed it lining the articulamentum ventrally in *T. marmorea*, and J. Baxter and A. Jones did not observe it at all in *Lepidochitona cinereus*[102]. In addition, B. Kreusch observed the mesostracum within the articulamentum, instead of lining it dorsoventrally, in *Cryptochiton stelleri*[103]. G. Laghi and F. Russo[100,101], as well as B. Kreusch[103], note that in species which contain the dorsal mesostracum, it is split dorsoventrally into two sub-layers by a row of aesthete channels. Thus, while the intermediate plates of *T. marmorea* have six layers, those of other chitons may be regarded as having 7 or 8. Some authors refer to the dorsal and ventral mesostracum layers collectively as the pallial myostracum[100,101,103,116]. With the sole exception of the dorsal mesostracum, the 3D spatial distribution of microstructures in the intermediate plates of *T. marmorea*, *C. olivaceous*[100], *C. tuberculatus*[98], and *L. gainardi*[103] are very similar. E. Poulicek and B. Kreusch[116] note that in the evolutionary series of chitons, the tegmentum becomes thinner (disappearing almost completely in the more evolved *Cryptochiton*), the articulamentum becomes thicker, and the hypostracum, mesostracum, and myostracal layers show little variation in proportions. Interestingly, J. Sulanowski observed that the hypostracum is absent in *Cryptoplax larvaeformis*[98].

Similar orientation, thickness, and branching irregularities of the first order lamellae of the crossed-lamellar layers of the shell plates of *T. marmorea* have also been reported in the shells of other mollusks[117,118,119]. The width of the first order lamellae in the crossed-lamellar layers of the shell plates of chitons (1-5 µm)[99] lies in the extreme lower end of the range found in crossed-lamellar microstructures across Mollusca (1-40 µm)[110,119]. The simple crossed-lamellar structures present in chiton shell plates do no possess well-defined second order lamellae. The width of the third order lamellae is typically around 300 nm. The angle between the two dip directions of third order lamellae in adjacent columns of first order lamellae in *T. marmorea* is approximately 40°, which is similar to the dip angles previously observed in *Chiton olivaceus* (~50°)[100], *Lepidopleurus cajetanus* (~45°)[101], and *Acanthopleura brevispinosa* (32–45°)[119], and much less than the range (60–85°) observed by W. Haas[99] in a number of species.

2.4.2 Constitution of the Organic Matrix of the Armor Plates

The intermediate plates of *T. marmorea* were determined to have an organic matrix content ~2.6 weight percent by TGA. E. Poulicek and B. Kreusch[116] found that the shell plate organic matrix ranged from 0.48 to 1.55 weight percent in 11 species (greatest in *Tonicella lineata*). However, they only considered the insoluble portion of the matrix in their measurements. In contrast to the proteinaceous composition of organic matrices of other mollusk shells, those of chiton shell plates possess a very large amount of the aminopolysaccharide chitin[120]. An earlier study determined the range of the weight percent of chitin in the insoluble portion of the shell plate organic matrix, girdle, and organic matrix of the girdle spicules to be 16–41, 1.6–16, and 0.2–15, respectively[116]. In addition, the shell plate organic matrix of *Acanthopleura villantii* was found to contain a chitin/protein ratio of 6.9, which is over a hundred times larger than that found in shells of other mollusks, specifically bivalves[120]. Our results are consistent with these studies. Because of its resistance to alkali treatment, it is easy to isolate chitinous material from most composite biomaterials, including cases where chitin is bound to proteins or pigments[121,122]. After alkali treatment, the shell plate organic matrix, girdle, and inter-plate material of *T. mamorea* displayed FTIR spectra very similar to an α-chitin standard from the demosponge *I. basta* (Fig. 2-3b). The protein content (0.17 weight percent) of the shell plates of *T. marmorea* is similar to the range found in the composite prismatic spines and scales (0.07–0.23 weight percent) of *Acanthopleura vaillantii*, *Acanthopleura spinigera*, *Nuttalina fluxa*, and *Ischnochitonina sp*[123]. This is consistent with the results of J. Taylor and M. Layman[109], who found that non-nacreous microstructures, including crossed-lamellar, composite prismatic, and granular types, generally have a protein content less than 0.4 weight percent. The amino acid profile of the shell plate organic matrix of *T. marmorea* (Fig. 2-5) is consistent with those of *Chiton marmoratus* and *Acanthopleura granulata*[99], with the sole exception of glycine content, which is about 8 mol percent greater in *C. marmoratus* and *A. granulata*. Calcification of the shell plates is likely controlled by the templating activity of acidic proteins[124], which may be attached to the chitinous network of the organic matrix (Fig. 2-4c).

2.4.3 The Biomechanical Role of the Microstructure of the Armor Plates

The multilayered structure of individual armor units plays a significant role in resistance to the complex multiaxial loading configurations caused by predatory attacks[125]. The sequence and spatial heterogeneity of the layers of the intermediate plates of *T. marmorea* suggests a structural response to different loading conditions experienced by different regions of the plates. The transverse distribution of the crossed-lamellar hypostracum (~900 μm thick in the jugal area, decreasing to 0 μm laterally, Fig. 2-1b) and orientation of its first order lamellae (parallel to the "x"-"y"

plane) may function to resist transverse bending (about the ''z''-axis). Three-point bending tests by J. Curry and A. Kohn[117] on samples of *Conus spp.* showed that the flexural strength of the crossed-lamellar microstructure is highly anisotropic. They determined the flexural strength to be ~70 MPa in the axial direction (perpendicular to long axes of first order lamellae) and ~200 MPa in the transverse direction (parallel to long axes of first order lamellae). Bending in the axial direction can break the layer by simply pulling the first order lamellae apart from each other (interface failure), while bending in the transverse direction cannot break the layer without breaking each first order lamellae across its long axis. The bending tendency of the plates will depend on the boundary conditions at the base of the shell[126]. Possible "abutment" effects of the girdle and substratum, as well as ''tie rod'' effects of the muscular system, will both increase the bending tendency.

Multiple ''channel'' cracking between first order lamellae is known to be important to the overall damage tolerance of shells with inner crossed-lamellar layers[127,128], and is likely an important energy dissipation mechanism in the shell plates of *T. marmorea* during longitudinal bending deformation. The lateral area of the plates, which likely experiences the largest longitudinal bending deformations, contains two middle layers (the articulamentum and mesostracum) whose first order interfaces differ in orientation from those of the hypostracum. This arrangement permits crack deflection and bridging in the middle layers, a mechanism which is responsible for a large portion of the energy dissipated during fracture of the shell of *Strombus gigas*[128,129]. The aforementioned surface waviness of the third order lamellae may generate a strain hardening mechanism similar to that found in nacre, in which the ''dovetails'' of individual nacre tablets produce a progressive tablet locking in tension that is responsible for a strain at failure (~1%) that is an order of magnitude greater than that of non-biogenic aragonite[130].

The transverse thickness distribution of the composite prismatic articulamentum layer (~900 μm thick laterally, decreasing to 0 μm centrally in the jugal area) suggests that it functions to resist circumferential tensile stress, as well to provide a stiff, hard layer to resist side penetration and pinching. The prism bundles in the articulamentum are aligned parallel to the interfaces of adjacent layers in the middle of the articulamentum, and perpendicular to theses interfaces at the layer junctions. This likely serves to provide discrete inter-prism structural pathways for cracks to propagate ventrally for easy arrest by the crossed-lamellar layers. The inner articulamentum and hypostracum layers may also function to resist drilling attacks. *Chiton tuberculatus* has been observed alive with drill holes that bore through the tegementum, but left the inner layers intact[152].

In contrast to the inner shell plate layers, the outer tegmentum's primary role is likely sensory rather than mechanical in nature. The aesthetes, a complex sensory network of tissue-filled channels, are embedded in the tegmentum. In a secondary mechanical role, the tegmentum may operate as a brittle outer shield, in which the main aesthete channels act as sacrificial stress concentrators which can distribute a concentrated load (e.g. a biting attack) over a larger area of the plate. As previously proposed by W. Haas[131], the fine-grained homogeneous myostracal layers' location in the impressions of the latero-pedal, oblique, and transverse muscles suggests that the fine-grained homogeneous microstructure may be best suited for muscle attachment.

3 The Visual System Integrated within the Armor Plates

3.1 Introduction

The design of structural materials with integrated functions including energy storage[132], sensing[133], and self-healing[134] is an emergent field which holds great potential for a diversity of engineering applications. Nature provides a multitude of multifunctional structural materials from which we can acquire design strategies. However, current research on these materials often focuses on the structure/property relationships of one function. The materials relationships and trade-offs between multiple functions are largely unexplored. Here we elucidate the multifunctional design and performance of the aragonite-based armor of the chiton *Acanthopleura granulata* (Fig. 3-1), which contains an integrated visual system. Chitons are the only known group of extant mollusks to have soft sensory tissue integrated within the outermost layer of their shells[73]. This tissue forms a complex network of channels that open dorsally as sensory organs known as the aesthetes. In certain species, the aesthetes include hundreds of lens eyes[77] which are capable of spatially resolving objects[80]. Unlike the protein-based lenses of most animal eyes, the lenses of chitons, like their shells, are principally composed of aragonite. *A. granulata* is able to tailor the local geometry, crystallography, and interfaces of aragonite to achieve a multifunctional armor.
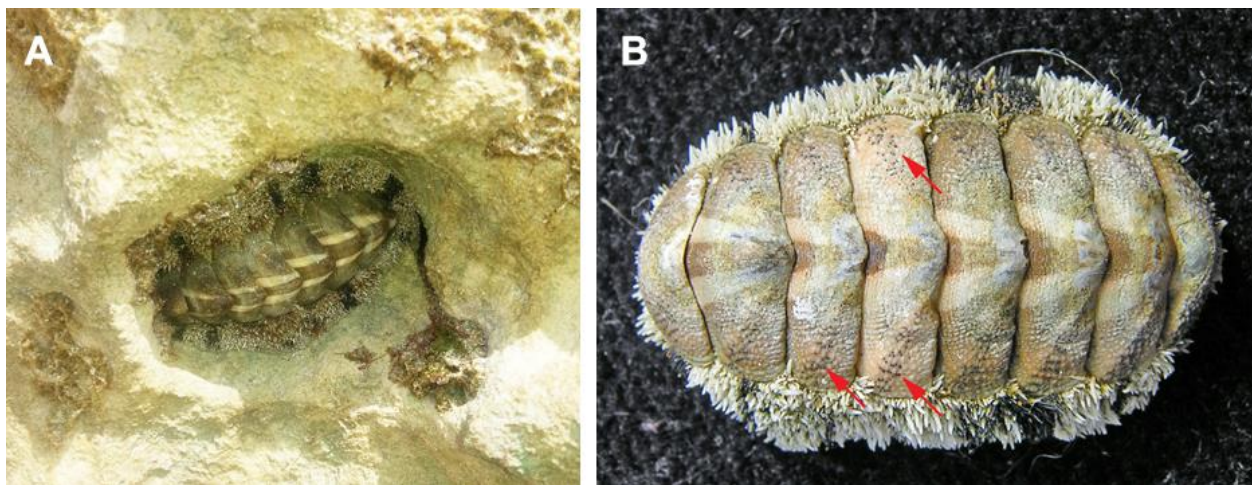
Figure 3-1| Photographs of *Acanthopleura granulata*. a, *A. granulata* on the rocks of Macao Beach, Dominican Republic in May 2013. Photograph was taken by Elaine Belmonte. **b**, Photograph of a dried shell by Bruno Anseeuw. Red arrows indicate regions of the shell that contain eyes. The dark pigmented areas that surround each eye are visible.

3.2 Materials and Methods

3.2.1 Sample Collection & Preparation

Acanthopleura granulata were collected from Tavernier, FL in August of 2011 and stored in a 70% ethanol solution until experimentation. To create cross-sectional samples for polarized light microscopy, nanoindentation, and electron backscattered diffraction, dried valves were first embedded in a room temperature curing epoxy. After curing for ~24 hours, samples were sectioned with a diamond saw (IsoMet 5000, Buehler, Lake Bluff, IL), polished (Model 920, South Bay Technology, CA) stepwise with aluminum oxide pads (15 μm, 5 μm, 3 μm, and 1 μm), and then finely polished with 50 nm silica nanoparticles on cloth (MultiTex, South Bay Technology, CA).

3.2.2 Light Microscopy

An Olympus SZX16 (Tokyo, Japan) microscope was used to image areas of the dorsal shell surface containing multiple eyes. Polished cross-sectional samples were imaged with polarized light using a Nikon Eclipse L150 (Tokyo, Japan).

3.2.3 Micro-Computed Tomography (μCT) & Morphometric Measurements

Dried fractured pieces, approximately 1 mm^3 in size, of *A. granulata* valves were scanned with an energy of 18 keV and a resolution of 0.74 μm/voxel at beamline 2-BM of the Advanced Photon Source of Argonne National Laboratory. Mimics (Materialise, Belgium) was used for image segmentation and construction of three-dimensional triangulated surface meshes (binary STL format). Cross-sectional meshes were created using the cut function of the simulation module Mimics. For figure creation, meshes were reduced in file size as needed via the smooth, reduce, and remesh functions of 3-matic (Materialise, Belgium) and rendered using Blender (www.blender.org). Open-source image analysis software ImageJ[157] was used to make all morphometric measurements. The curvatures of the top and bottom surfaces of the longitudinal and transverse cross-sections of the lens region were fit from the aggregation of data from 7 lenses. 29 points were collected from each surface of each lens, for a total 203 points/surface.

3.2.4 Focused Ion Beam Milling (FIB) & Electron Microscopy

Dried fractured pieces of *A. granulata* valves were fixed on a scanning electron microscopy (SEM) aluminum holder with carbon tape. Samples were coated with

carbon to minimize charging effects. A Helios Nanolab 600 Dual Beam (FEI, OR) was used for SEM imaging at an accelerating voltage of 2-4 kV and a working distance of ~4 mm. Several cross-sectional and transmission electron microscopy (TEM) samples were prepared with FIB milling using the same system. Do to the large size and complex geometry of the eyes, a protocol for preparing TEM samples was developed: 1) A platinum protective layer (~0.5 μm) was first deposited on top of the lens region of an individual eye; 2) A second platinum protective layer (~3 μm) was deposited on top of the rectangular region of interest (approximately 20 μm × 100 μm), which was to be milled out; 3) Four trenches surrounding the rectangular region were milled by FIB (30 kV, 9.5 nA), creating a cross-sectional slab of the lens region. The slab was attached to an in situ OMNI probe via platinum deposition and lifted out; 5) the slab was transferred via FIB and platinum deposition from the OMNI probe to a tungsten needle that was fixed to an SEM holder with carbon tape; 6) Multiple TEM samples of the lens region with a variety of orientations were prepared using the following procedure: 6.1) deposition of a protective platinum layer (~3 μm); 6.2) Stepwise FIB milling from 30 kV to 2kV; 6.3) Lift-out via an in situ OMNI probe; 6.4) Attachment to a copper TEM grid and final FIB thinning and polishing (2 kV, 28 pA). Bright field TEM imaging and SAED were carried out using a JEOL 2011 operated at 120 kV to minimize beam damage. The image magnification and camera constants were calibrated using a standard sample (MAG*I*CAL, Electron Microscopy Sciences, PA, USA). A field emission JEOL 2010F, operated at 200 kV, was used for HRTEM imaging.

3.2.5 Energy-Dispersive X-ray Spectroscopy (EDX)

EDX measurements of the lens region were conducted on FIB-polished cross sections with a Helios Nanolab 600 Dual Beam (FEI, OR) equipped with an INCA EDX system (Oxford Instruments) at an accelerating voltage of 20 kV.

3.2.6 Electron Backscattered Diffraction (EBSD)

Finely polished cross-sectional samples were coated with an ultra-thin layer of carbon and mounted on a 70° pre-tilted stage. EBSD was carried out using a Helios Nanolab 600 Dual Beam system (FEI, OR) equipped with the HKL Technology "Channel 5" system. EBSD patterns were generated using a working distance of 6 mm, a step size of 1 μm, an accelerating voltage of 20 kV, and a beam current of 2.7 nA.

3.2.7 Ray-Trace Simulations

The ray-tracing program was written in IGOR Pro (WaveMetrics) by Prof. Mathias Kolle (Department of Mechanical Engineering, MIT). Each 2D simulation was repeated

for each cross section of the lens region (longitudinal and transverse), refractive index of the lens (ordinary and extraordinary rays), and external environment (air and seawater). Thus eight (2 × 2 × 2) measurements were made for each optical quantity.

3.2.8 Refractive Indices Used in Ray-Trace Simulations

The refractive indices used for air and seawater were 1 and 1.336, respectively. Since the cornea is continuous with granular microstructure of the non-sensory regions, which has a weak texture, it was given a refractive index of 1.632, the average of the three indices of aragonite. Although aragonite is a biaxial crystal, the pseudo-hexagonal symmetry about its c-axis allows it to be approximated as uniaxial with n_o = 1.683 and n_e = 1.530[135]. The optical properties of uniaxial crystals are only dependent on the polar angle θ that the incident wave vector forms with the optical axis, and not on the azimuthal angle[136]. While n_o does not vary with θ, n_e is given by[136]:

$$n_e(\theta) = \left(\frac{n_o n_e}{\left[n_e^2 \cos^2(\theta) + n_o^2 \sin^2(\theta) \right]^{1/2}} \right)$$

Since the c-axis is oriented ~45° below the surface normal, the refractive indices of the lens were approximated as n_o = 1.683 and $n_e(45°)$ = 1.601, assuming normal incidence. The thin organic layer underneath the lens, *L1*, was modeled as chitin (n = 1.435[137]), which is a major component of the organic matrix of chiton shells[94]. Since *L2* is calcified and amorphous, it was given a refractive index of 1.58, a value which lies in the experimentally determined range of ACC, 1.579-1.583[138], and has been used to calculate the focal length of ACC microlenses[139]. The photoreceptive region was given a refractive index of 1.36, which has been used to model the retinal receptors of jellyfish eyes[140].

3.2.9 Rear Focal Point (F)

The rear focal points of the lens region were measured by ray tracing. Simulations included 37 normally incident rays centered about the optical axis with a ray-ray separation distance of 1 μm. The incident spot size, 36 μm, reflects the minimum simulated entrance pupil diameter, *D*. The location of the rear focal points were measured to the nearest micron by plotting the constructive overlap of the refracted rays in image space. In each simulation, the 1 um^2 region with the greatest intensity was considered to be position of the rear focal point, *F*.

3.2.10 Rear Principal Point (P)

The locations of the rear principal points were measured to the nearest micron via ray tracing by considering a single incident ray, parallel to and 15 μm away from the optical axis of the lens, which focuses on the rear focal point (Fig. 3-16). The emerging ray appears to be singularly refracted at an imaginary surface located at the position of the rear principal point, P[141].

3.2.11 Rear Focal Length (f)

The rear focal length, f, was calculated using the thick lens equation:

$$f = F + P$$

3.2.12 Field of View (α)

The field of view, α, was measured to the nearest 2.5 degrees via ray tracing using an incident spot size of 25 μm and a ray-ray separation distance of 1 μm. We define the field of view as the maximum incidence angle of light, α, relative to the optical axis, that is capable of being focused a distance d orthogonally away from the optical axis such that $d \leq (w_c{}^T/2)$, where $w_c{}^T$ is the maximum width of the chamber in the transverse cross section (Fig. 3-2). This criterion ensured that we selected the largest value of α that can produce a rear focal point inside the chamber of the eye.
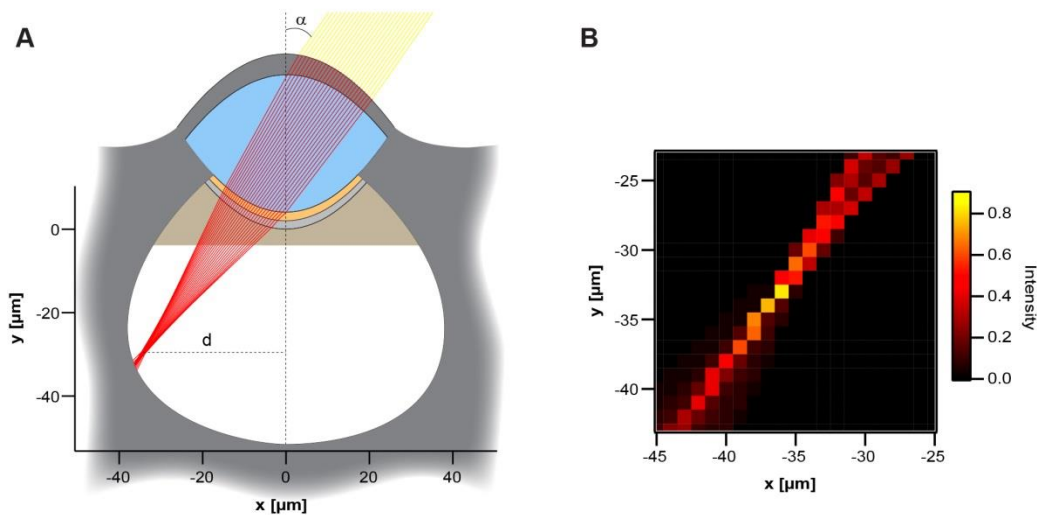
Figure 3-2| Illustration of the criterion used to determine the field of view of an individual eye. a and **b**, Schematic diagram and corresponding intensity plot, respectively, derived from a ray-trace simulation. We define the field of view as the maximum incidence angle of light, α, relative to the optical axis, that is capable of being focused a distance d orthogonally away from the optical axis such that $d \leq (w_c{}^T/2)$, where $w_c{}^T$ is the maximum width of the eye chamber in the transverse cross section.

43

3.2.13 Angular Resolution (Δψ)

The photoreceptors within the eye chamber were assumed to be contiguous, which makes the angular resolution approximately equal to the inter-receptor angle, $\Delta\phi$. The interceptor angle is given by[142]:

$$\Delta\varphi = \tan^{-1}\left(\frac{s}{f}\right)$$

where s is the photoreceptor spacing, which is ~7 μm in *A. granulata*.

3.2.14 Entrance Pupil Diameter (D)

The entrance pupil diameter, D, was measured via ray tracing to the nearest micron. We define D as the largest width (spot size) of normally incident light, centered about the optical axis, which can be focused by the lens system into the chamber below without producing any total internal reflections.

3.2.15 F-number

The F-number is defined as (f/D)[141], where D is the entrance pupil diameter and f is the rear focal length. In general, (F-number)$^{-2}$ is proportional to image brightness[142].

3.2.16 Sensitivity (S)

The chiton *Acanothopleura granulata* is an intertidal animal, so we estimated the sensitivity, S, of its eyes using a formula appropriate for eyes operating under broad spectrum "white" light[143]:

$$S = \left(\frac{\pi}{4}\right)^2 D^2 (\Delta\rho)^2 \left(\frac{kl}{2.3 + kl}\right)$$

where D is the entrance pupil diameter, $\Delta\rho$ is the angle in space over which each receptor accepts light, k is the absorption coefficient, and l is the length of the rhabdoms of the microvillous photoreceptors. For single-chamber eyes such as those of chitons, $\Delta\rho$ is approximately equal to the inter-receptor angle, $\Delta\phi$. For *A. granulata*, l is ~8 μm[80], which is consistent with P. Boyle's work on *Onithochiton neglectus*, in which l is ~10 μm[144]. Note that this length refers to the length of the photoreceptive region of the photoreceptors (the rhabdoms), not to the entire length of the photoreceptors. We approximated k as 0.0067 μm^{-1}, a value which is based on measurements of the absorption of photoreceptors from the lobster *Homarus americanus*[145], and is often used to calculate the sensitivity of rhabdomeric photoreceptors of invertebrates[143]. The actual sensitivity will also depend on spatial summation, temporal summation, wavelength-

specific absorption, and the spectral composition of the light environment of *A. granulata*.

3.2.17 Image Formation and Focal Length Measurements

Valves of *A. granulata* were carefully fractured with tweezers to obtain small fragments of the outer shell layer in which the bottom surfaces of lenses were revealed. These fragments were mounted on a small needle on a 3-axis stage positioned beneath a 63× water immersion objective. A chrome mask containing printed objects of known size derived from the 1951 USAF resolution test chart (http://www.efg2.com/Lab/ImageProcessing/TestTargets/#USAF1951) was placed below each sample. Each sample was oriented such that the dorsal shell surface was facing, and approximately parallel to surface of the underlying chrome mask. Next, a small drop of water was placed on the chrome mask, and then the sample was lowered into the water. To locate the ventral surface of individual lenses, the 63× immersion objective was brought into focus using illumination from the microscope. To create objects, the chrome mask was illuminated from below through a 10× objective using a ThorLabs (Newton, NJ) L2-1 source. Images of these objects formed by individual lenses were brought into focus using the 63× immersion objective. To calculate the focal length of each lens, the object distance was varied using the "z"-translation stage of the sample. At each object distance, the image size was measured independently by three researchers, and an average image size was calculated. Since the object sizes were known, we were able to calculate the magnification, $M = (h_i/h_o)$, where h_i and h_o are the heights of the image and object, respectively. The object distance and magnification data were fit to the linear thick lens equation:

$$\frac{1}{M} = \frac{z}{f} + \left(\frac{z_o + P^*}{f} - 1\right)$$

where z_o is the initial object distance, z is the distance away from z_o, and P^* is the front principal point distance. The rear focal length, f, was calculated from the slope. To calculate the position of the rear focal point via $F = f - P$, the average value of P determined from ray-trace simulations in seawater, 15.5 µm, was used.

3.2.18 Nanoindentation

Nanoindentation experiments were conducted on finely polished cross-sectional samples in ambient conditions using a TriboIndenter (Hysitron, MN, USA). Blunt Berkovich (trigonal pyramid, semi-angle = 65.3°) and sharp conospherical (tip radius ~ 1 µm, semi-angle = 30°) diamond probe tips were used to obtain quantitative material properties (E_{O-P} and H_{O-P}) and investigate fracture behavior, respectively. Typical load

functions included loading (10 s) to the maximum load (5 mN), holding (20 s), and unloading (10 s). The Oliver-Pharr (O-P) methodology[146] was used to quantify material properties, i.e. indentation modulus ($E_{O\text{-}P}$) and hardness ($H_{O\text{-}P}$). The probe tip area function $A(h_c)$, which is the projected area of the indentation tip as a function of contact depth, h_c, and frame compliance were calibrated prior to each set of experiments using a fused quartz sample.

3.2.19 Microindentation

Microindentation experiments on intact shell plates were conducted in ambient conditions using an instrumented microindenter (MicroMaterials). A flat punch tip (diameter of the bottom surface ≈ 80 μm) was used to compress the eyes, megalaesthetes, and protruding non-sensory regions. Typical load functions included loading (30 s) to a maximum load (~1 N), holding (5 s), and unloading (30 s). The post-indentation residues were imaged via SEM using a Helios NanoLab 600 Dual Beam (FEI, OR).

3.3 Results

3.3.1 Structure of the Integrated Sensory System

The two main sensory structures of the shell of *A. granulata* (Fig. 3-1) appear on the surface as small bumps ~50 μm in diameter (Fig. 3-3a and b). The more numerous megalaesthetes, which are common to most chitons, are capped with a pore and maintain the same color as non-sensory regions. As seen in Fig. 3-3a, the eyes are distinguished by their translucent lens, which is encircled by a dark pigmented area (outer diameter 86 ± 3 μm). Scanning electron microscopy (SEM) revealed that the surfaces of the eyes are much smoother than those of the neighboring megalaesthetes and non-sensory protrusions (Fig. 3-3b, inset). Both sensory structures are located within the valleys formed by protruding non-sensory regions, as revealed by a 3D stereographic reconstruction of the shell surface (Fig. 3-4a and b).
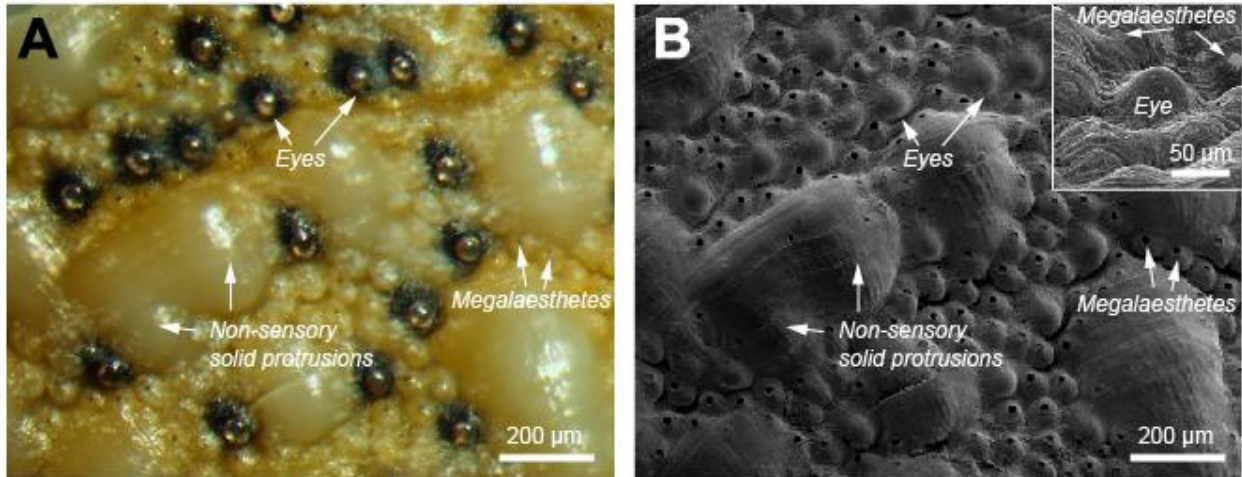
Figure 3-3 | Dorsal surface of an intermediate plate of *A. granulata*. a, Light micrograph of an area containing multiple sensory structures: lens eyes (unique to twos lineages) and megalaesthetes (common to most chitons). **b**, SEM image corresponding in position to (**a**).
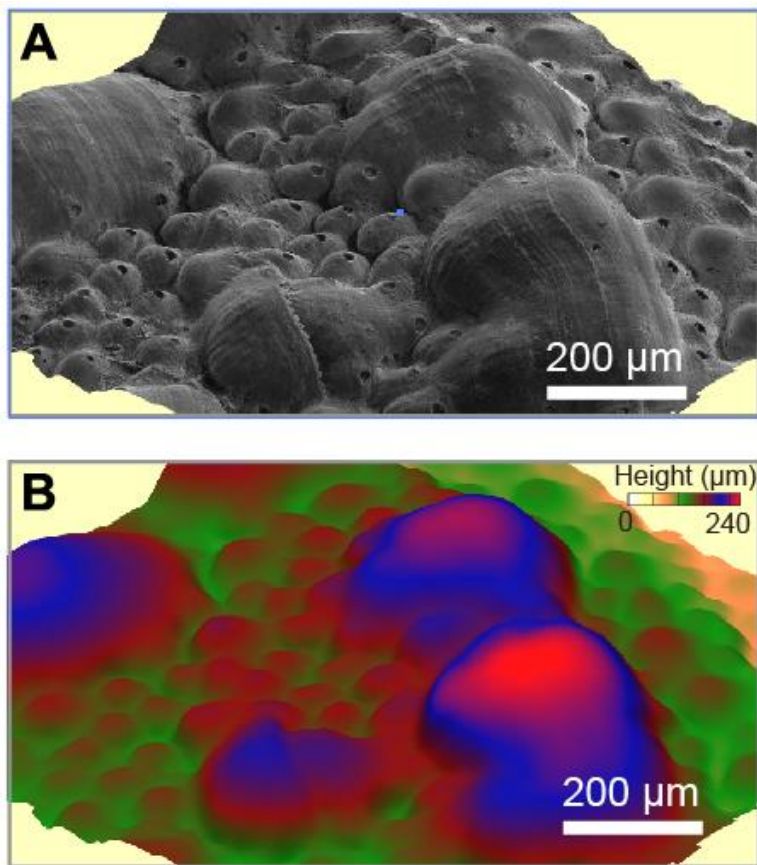
Figure 3-4 | Roughness of the dorsal surface of an intermediate plate of the chiton *A. granulata*. a, SEM-derived stereographic reconstruction of the shell surface. **b**, Height map corresponding to (**a**).

Synchrotron μCT was used to investigate the 3D morphology of the megalaesthetes and eyes (Fig. 3-5). In contrast to the cylindrical chambers of the megalaesthetes, which have diameters around 40 μm, the specialized eye chambers are pear-shaped and have a depth and width of ~55 μm and ~75 μm, respectively. This results in an eye chamber volume that is approximately five times greater that of the megalaesthete. Detailed morphometric measurements from 7 eyes can be found in Fig. 3-6. Numerous small sensory pores, known as micraesthetes, were observed branching from the chambers of the eyes and megalaesthetes to the shell surface (Fig. 3-5f and g). The lens region of each eye is ~38 μm thick and slightly elongated in the direction of the optic canal, which we denote as the longitudinal direction (Fig. 3-7a). Fig. 3-7b illustrates the average cross-sectional shape of the lens region in the longitudinal and transverse planes. The bottom surfaces were generally best fit with parabolic curvatures (Fig. 3-7c), which may function to reduce spherical aberration.

Interestingly, highly X-ray absorbent structures were discovered within the chambers of both the megalaesthetes and eyes (Fig. 3-5a-d). These structures were found to contain calcium (discussed later), so I denote them as intra-chamber calcified material (ICCM). In megalaesthetes, the ICCM consist of rod-shaped structures. The long axes of the rods are approximately parallel to the long axis of the megalaesthete chamber (Fig. 3-5c and e). In eyes, the ICCM forms a "c"-shaped pocket which presumably encircles the retina (Fig. 3-5d). ICCM was probably not uncovered earlier for two reasons. First, prior studies of the interior structure of megalaesthetes and eyes focused on living tissues, so samples were decalcified[80,144]. Secondly, ICCM is easily destroyed by polishing, and perhaps other common sample preparation techniques. Selected area electron diffraction (SAED) revealed that the ICCM is amorphous (Fig. 3-11). Therefore, we hypothesize that the ICCM is composed primarily of amorphous calcium carbonate (ACC). Although to date the only mineral component found in chiton shell plates has been aragonite[123], a number of organisms produce stable ACC[147].
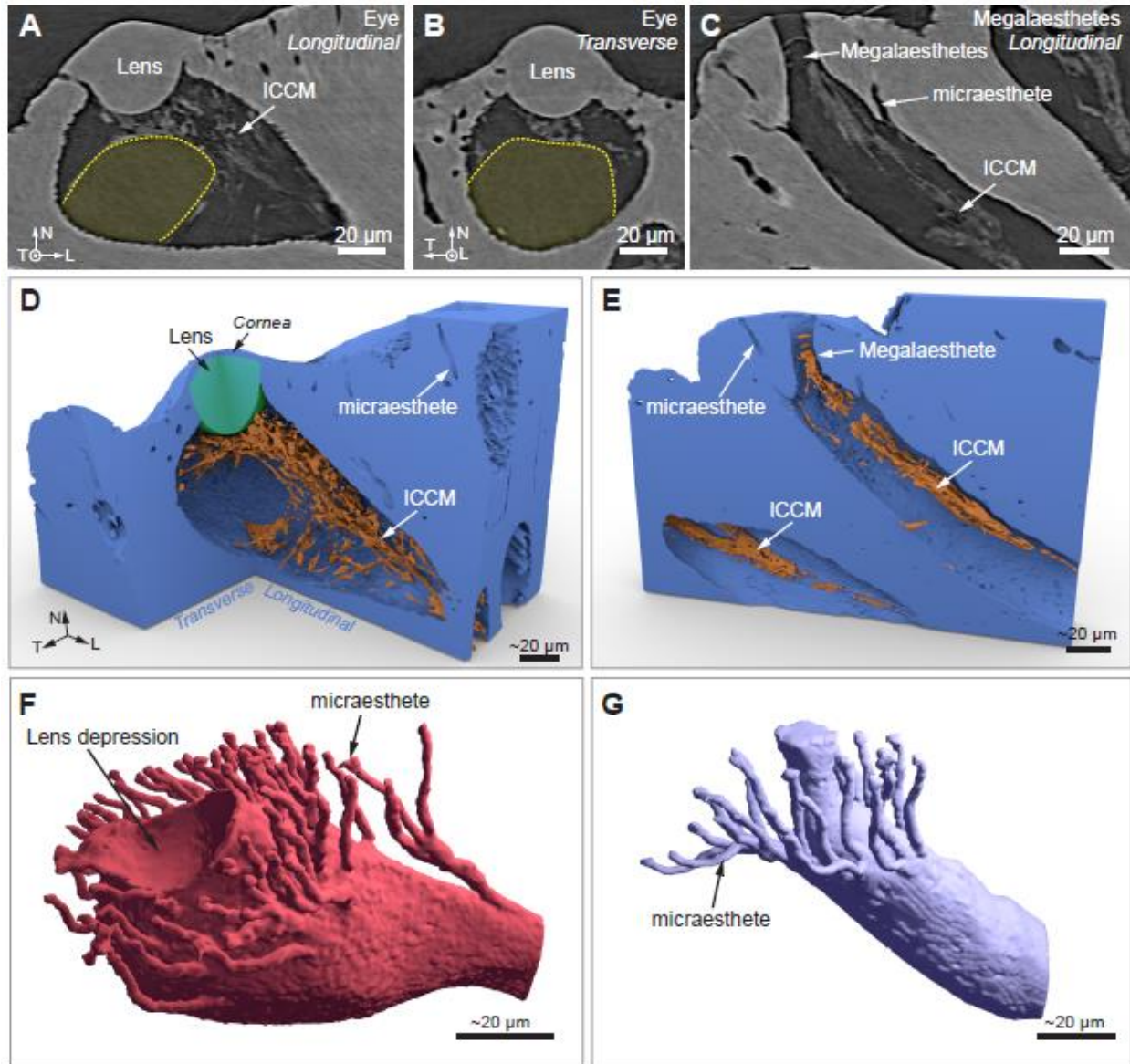
Figure 3-5 | Synchrotron μCT reconstructions of the sensory structures integrated within the outer shell layer of *A. granulata*. a and **b**, Transverse and longitudinal, respectively, tomographic slices of an eye. Highlighted areas indicate regions which likely contain the photoreceptors. **c**, Longitudinal cross-sectional slice of a megalaesthete. Highly X-ray absorbent material is clearly visible inside the chambers of both sensory structures. This material was found to be calcified, so I refer to it throughout this thesis as intra-chamber calcified material (ICCM). **d** and **e**, 3D reconstructions of a megalaesthete and an eye, respectively, highlighting the calcified structures: outer shell layer and cornea (blue), ICCM (orange), and lens (green). **f** and **g**, 3D reconstructions of the non-calcified (minimally X-ray absorbent) volumes of the megalaesthetes and eyes, respectively. These volumes represent the chambers which contain soft sensory tissues. Numerous small sensory structures, micraesthetes, branch from these chambers to the shell surface. Axes of eye coordinate system: N, surface normal (parallel to the optical axis); L, longitudinal; T, transverse.
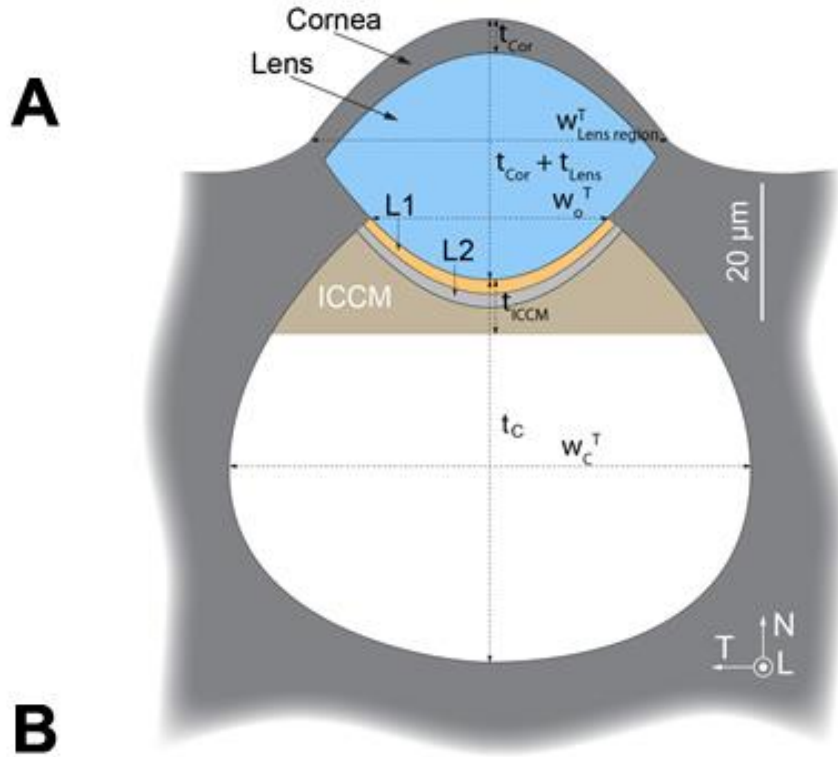
Symbol	Description	Measurement (µm)	Method
t_{Cor}	Thickness of Cornea	~5	OM
$t_{Cor} + t_{Lens}$	Thickness of Cornea and Lens	38 ± 2	µCT
t_{L1}	Thickness of Layer L1	~2	SEM
t_{L2}	Thickness of Layer L2	~2	SEM
t_{ICCM}	Depth of ICCM Below Lens	8 ± 1	µCT
d_C	Distance from Bottom of Lens to Back of Chamber	56 ± 7	µCT
w_C^L	Maximum Width of Chamber in "L" Cross Section	108 ± 7	µCT
w_C^T	Maximum Width of Chamber in "T" Cross Section	76 ± 5	µCT
w_o^T	Width of Bottom of Lens in "T" Cross Section	35 ± 2	µCT
$w_{Lens\ region}^T$	Width of Lens Region in "T" Cross Section	~52	µCT and fitting
$w_{Lens\ region}^L$	Width of Lens Region in "L" Cross Section	~56	µCT and fitting

Figure 3-6 | Morphometric measurements of the eyes of the chiton *A. granulata*. a, Schematic diagram defining the morphometric dimensions. **b**, Table displaying the average (± standard deviation) values of measurements from 7 eyes. Abbreviations: T, Transverse; L, Longitudinal; ICCM, Intra-chamber calcified material.

50

		Spherical $y = r - (r^2 - x^2)^{0.5}$		Parabolic $y = Ax^2$	
		r (Avg. $\pm$ SD μm)	R^2	A (Avg. $\pm$ SD μm^{-1})	R^2
Top Curvature	Longitudinal	38.4 $\pm$ 0.4	0.926	-0.0145 $\pm$ 0.000163	0.939
	Transverse	25.6 $\pm$ 0.2	0.931	-0.0259 $\pm$ 0.000271	0.951
Bottom Curvature	Longitudinal	24.6 $\pm$ 0.2	0.731	0.0339 $\pm$ 0.00058	0.870
	Transverse	21.2 $\pm$ 0.2	0.895	0.0298 $\pm$ 0.00049	0.891
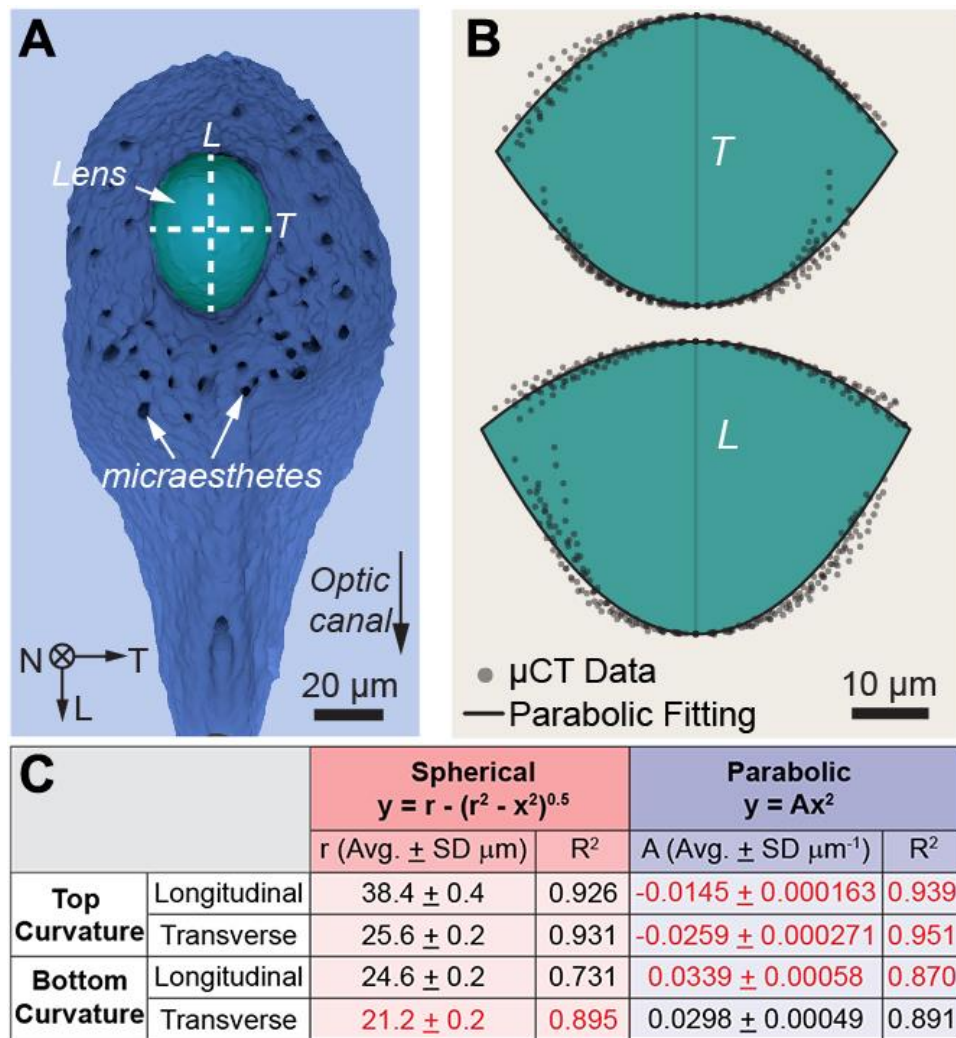
Figure 3-7 | Geometry of the lenses of the eyes of the chiton *A. granulata*. a, Bottom view of the lens region of the eye displayed in Fig. 3-4d showing the axially asymmetric lens surrounded by the pores of small branching micraesthetes. **b,** Average curvatures of the biconvex lens in the transverse (T) and longitudinal (L) cross sections measured via synchrotron μCT and fit with parabolic curves.

3.3.2 Fine Structure, Composition, and Crystallography of the Lens Region

Next, we compared the fine structure, composition, and crystallography of the lens region of the eyes to the granular microstructure which makes up the bulk of the calcified portion of the outer shell layer. Viewing polished cross sections of eyes under cross-polarized light (Fig. 3-8a) showed that the lenses have a relatively uniform grayscale level compared to the surrounding granular microstructure, which is known to have no preferred grain orientations in the chiton *Tonicella marmorea*[94]. This suggested that the lens is either a single crystal or is polycrystalline with highly aligned grains. The clear boundaries between the lens and granular microstructure in Fig. 3-8a indicate a delicate control of crystallography in the lens region. A thin (~5 μm thick) concavo-convex corneal layer covers the lens and is continuous with the surrounding granular microstructure. Sectioning an eye by focused ion beam (FIB) milling revealed the presence of additional two layers, *L1* and *L2*, underlying the lens (Fig. 3-8b). Energy-dispersive X-ray spectroscopy (EDX) indicated that *L1* is mainly composed of organic materials, while *L2* contains calcium (Fig. 3-7c). Many struts dorsally branch from *L2* to the chamber walls (Fig. 3-9). This ICCM corresponds in size, shape, and location to the aforementioned X-ray absorbent structures observed in the chamber with μCT (Fig. 3-3d).
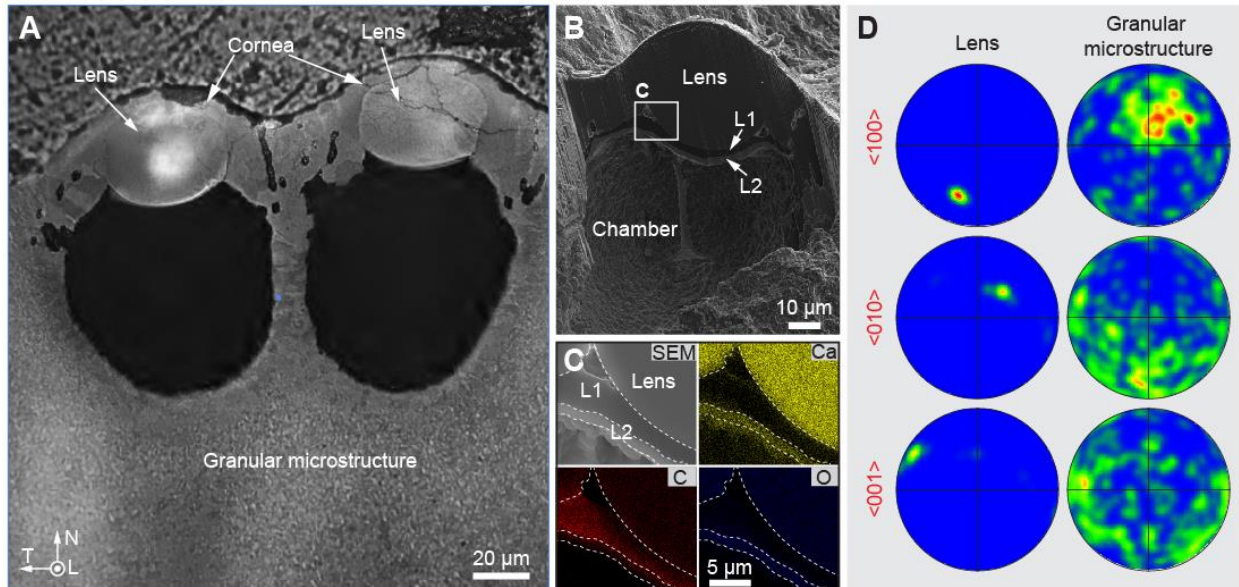
Figure 3-8 | Structure, composition, and crystallography of the lens region of the eyes of *A. granulata*. **a**, Polarized light micrograph of a polished transverse cross section containing two adjacent eyes. **b**, SEM image of a FIB-cut cross-section of an eye. **c**, EDX mapping of a FIB-polished cross-section of the lens and underlying layers *L1* and *L2*. **d**, EBSD pole figures from a lens and surrounding granular microstructure.
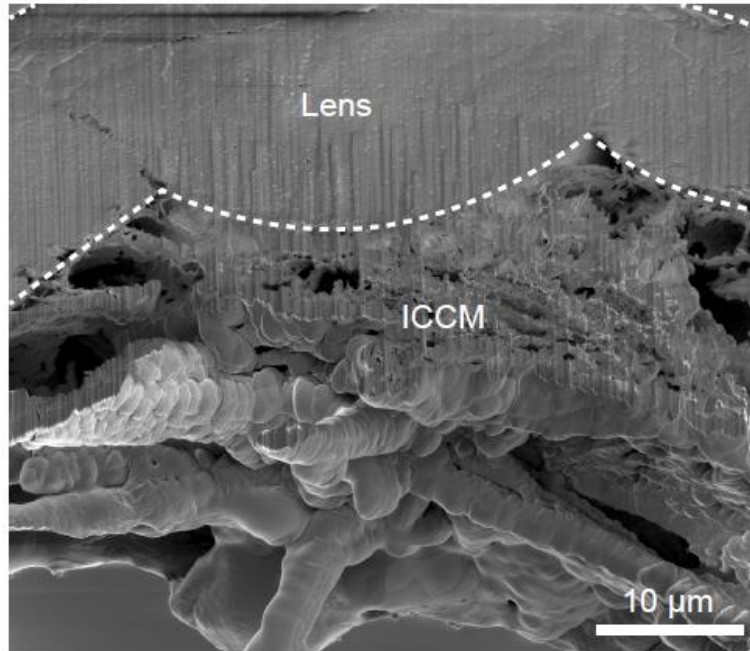
Figure 3-9│ SEM image of a FIB-prepared cross section of the lens region of an eye of the chiton *A. granulata*. Intra-chamber calcified material (ICCM) is abundant below the lens.
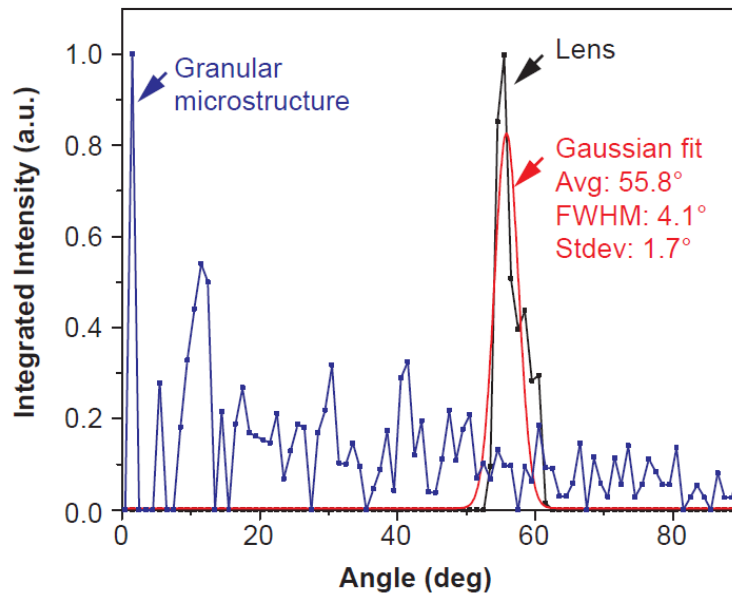
Figure 3-10│ Integration distribution of the tilt angle of the aragonite c-axis in the lens (black) and adjacent granular microstructure (blue) with respect to the normal of the cross section. A light micrograph of the cross section is displayed in Fig. 3-8a. The red curve represents a Gaussian fit of the data from the lens.

Further characterization indicated that the lens is structured to minimize light scattering. The crystallographic pole figures obtained with electron backscattered diffraction (EBSD) in Fig. 3-8d confirmed that the lens has a strong texture, indicated by the regions of localized intensity, which is in stark contrast to the weak texture of the surrounding granular region. Integrating the c-axis from the pole figure of the lens shows that the full width at half maximum is ~4°, which indicates that the c-axes of the grains are highly aligned (Fig. 3-10). The high-resolution transmission electron microscopy (TEM) image and corresponding Fast Fourier Transformation pattern from the lens (Fig. 3-11a), and the bright field TEM image and corresponding SAED pattern of the granular microstructure (Fig. 3-11b) further highlight the small and large crystallographic mismatch between grains in the lens and granular microstructure, respectively. EBSD showed that the lens has an average grain size of roughly 10 μm (Fig. 3-12a), which is approximately an order of magnitude greater than that of the surrounding granular microstructure. High resolution SEM images of polished cross sections (Fig. 3-13) show that lens and surrounding granular region possess very faint and easily discernable grain boundaries, respectively. Furthermore, high-resolution TEM images (Fig. 3-14) suggest that the lens may possess less intracrystalline organic material than the surrounding granular microstructure. The large grain size, sharp grain boundaries, relatively low amount of intragranular organic material, and uniform crystallographic orientation of the lens likely serve to minimize the scattering of light, improving the optical quality of the eyes.

EBSD and SAED of multiple lenses demonstrated that the polar angle θ between the c-axis and optical axis was consistently ~45°, while the orientations of the a- and b-axes were inconsistent. Since aragonite is a pseudo-uniaxial crystal, the non-normal orientation of the c-axis should generate double refraction, which is consistent with observations that the lenses are birefringent when viewed with polarized light[78,80].
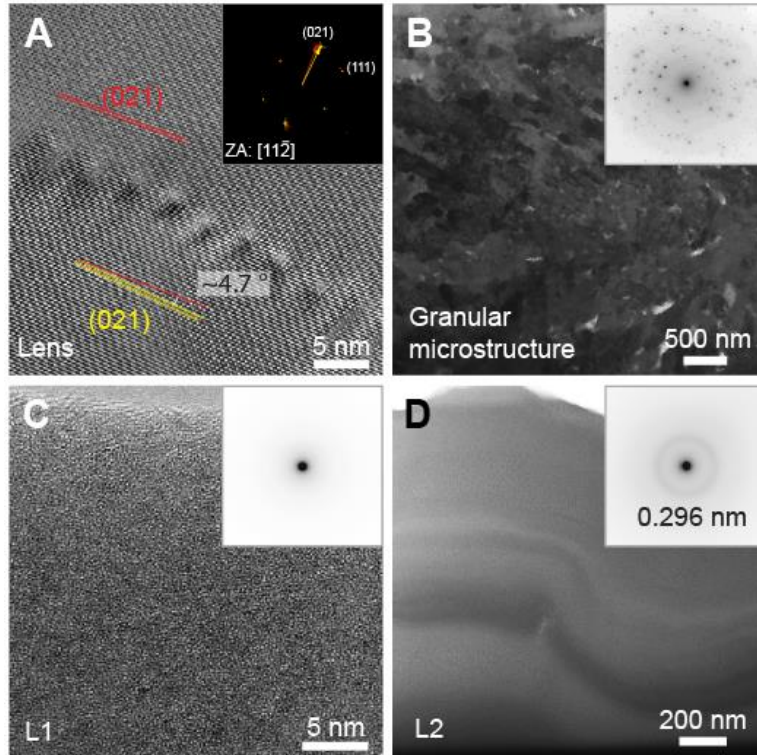
Figure 3-11 | Fine structure of the lens region. **a**, HRTEM image of two adjacent aragonite grains in the lens with a small misorientation angle (~4.7°). **Inset**, Corresponding FFT pattern with a zone axis of [11$\bar{2}$]. **b-d**, Bright field TEM images and SAED patterns (**insets**) of the granular microstructure, *L1*, and *L2*, respectively.
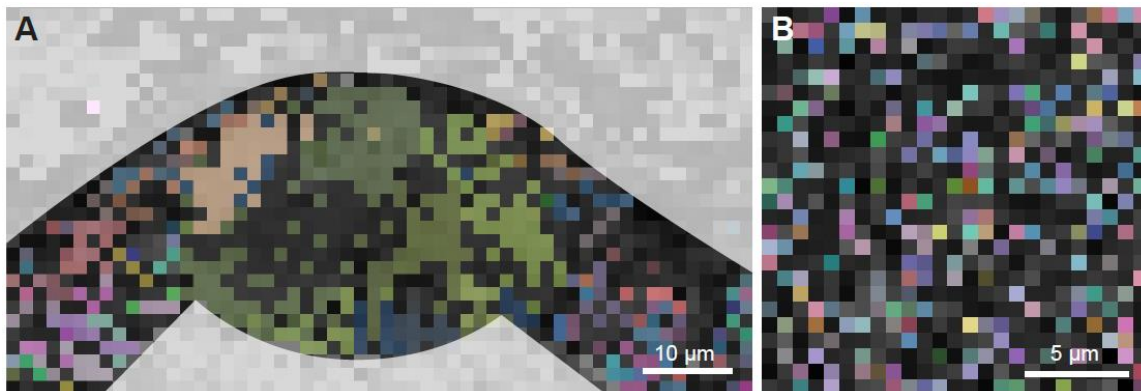
Figure 3-12 | EBSD maps from a lens and non-sensory region of the outer shell layer of the chiton *A. granulata*. a, Map of the lens region illustrating the large grains of the lens. **b**, Map of a non-sensory region showing the small grain size of the granular microstructure.
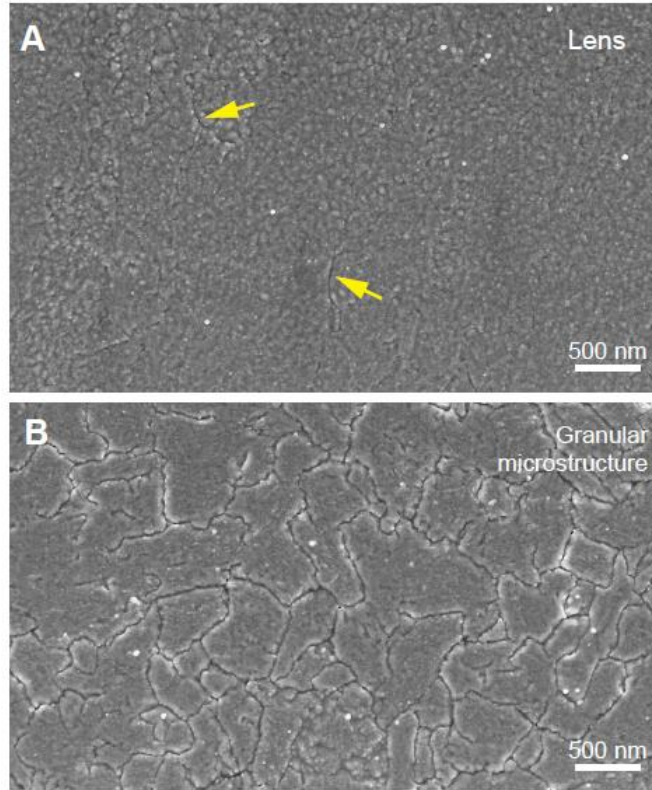
Figure 3-13| **SEM images from a polished cross section of the outer shell layer of the chiton** *A. granulata*. **a**, Lens of an eye. Yellow arrows indicate the faint grain boundaries. **b**, Granular microstructure of the non-sensory regions.
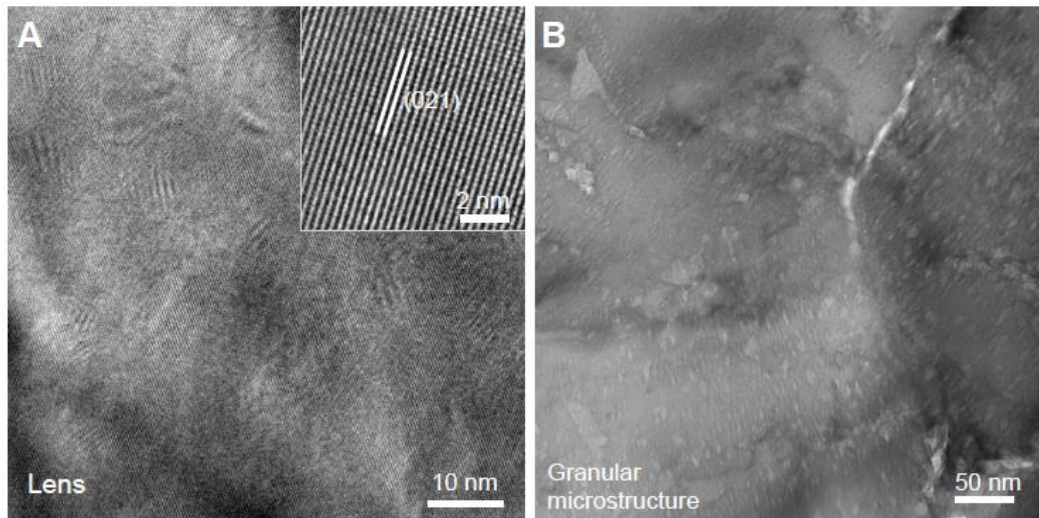
Figure 3-14| **TEM images of a lens and granular microstructure of the non-sensory regions**. **a**, High-resolution TEM image of a lens. **b**, Bright field TEM image of the granular microstructure of the non-sensory regions, which shows distributed nanoscopic inclusions within the small crystalline grains. Notice that the orientations of the inclusions are different in adjacent grains, which is probably related to their crystallographic misorientation.

3.3.3 Optical Performance of the Eyes

The optical performance of individual eyes of *A. granulata* was investigated via both theoretical modeling and experimental measurements. First, key elements of the geometry, composition, and crystallography of the lens region were combined in 2D ray-trace simulations (see methods 3.2.7 – 3.2.16 for details) to investigate the location of the rear focal points, *F*. *A. granulata* is an intertidal animal, so it is necessary to consider external environments of both air and seawater. For each environment, the rear focal points of the ordinary and extraordinary rays were calculated in two orthogonal extremes, the transverse and longitudinal cross sections (Fig. 3-15). The results are illustrated in the left half of Fig. 3-18. The ranges of *F* in air and seawater, 8-28 μm and 25-51 μm below *L2*, respectively, lie within the maximum allowed photoreceptor range, ~4-52 μm, which is constrained above by ICCM and below by the end of the chamber. Interestingly, if *θ* were 0° or 90° instead of 45°, the maximum values of *F* in seawater would be 35 μm or 71 μm, which means the chamber would be unnecessarily large or small, respectively. Thus, the geometry of the chamber is highly consistent with *θ* ≈ 45°. The positions of *F* within the allowed range of photoreceptors suggests that *A. granulata* is not required to use different polarizations of light to form images in air and seawater as was previously hypothesized[80], unless the actual photoreceptor range is much smaller than that which is geometrically permitted. In this context, since birefringence would not increase functionality, it is puzzling why *θ* is not 0°, which would eliminate double refraction aberrations as in the lenses of trilobites[28] and brittlestars[31].

Ray-tracing was used to measure location of rear principal points, *P*, which was needed to calculate the rear focal lengths, *f*, via $f = F + P$[141]. Fig. 3-15 illustrates the relationship between *F*, *P*, and *f*. The rear focal lengths were used to quantify the resolution of an individual eye. Assuming that the photoreceptors within the eye chamber are contiguous, we approximated the angular resolution as the inter-receptor angle. The inter-receptor angle, *Δϕ*, was calculated using $\Delta\phi = \tan^{-1}(s/f)$[142], where *s* is the average distance between the centers of adjacent retinal cells, which is ~7 μm in *A. granulata*[80]. We determined that *Δϕ* ranges between 8-13° in air and 6-9° in seawater (Table 3-1). These results are consistent with behavioral experiments, in which *A. granulata* responded to dark targets with an angular size of 9° in both air and seawater, but was not able to detect targets with an angular size of 6°[80].
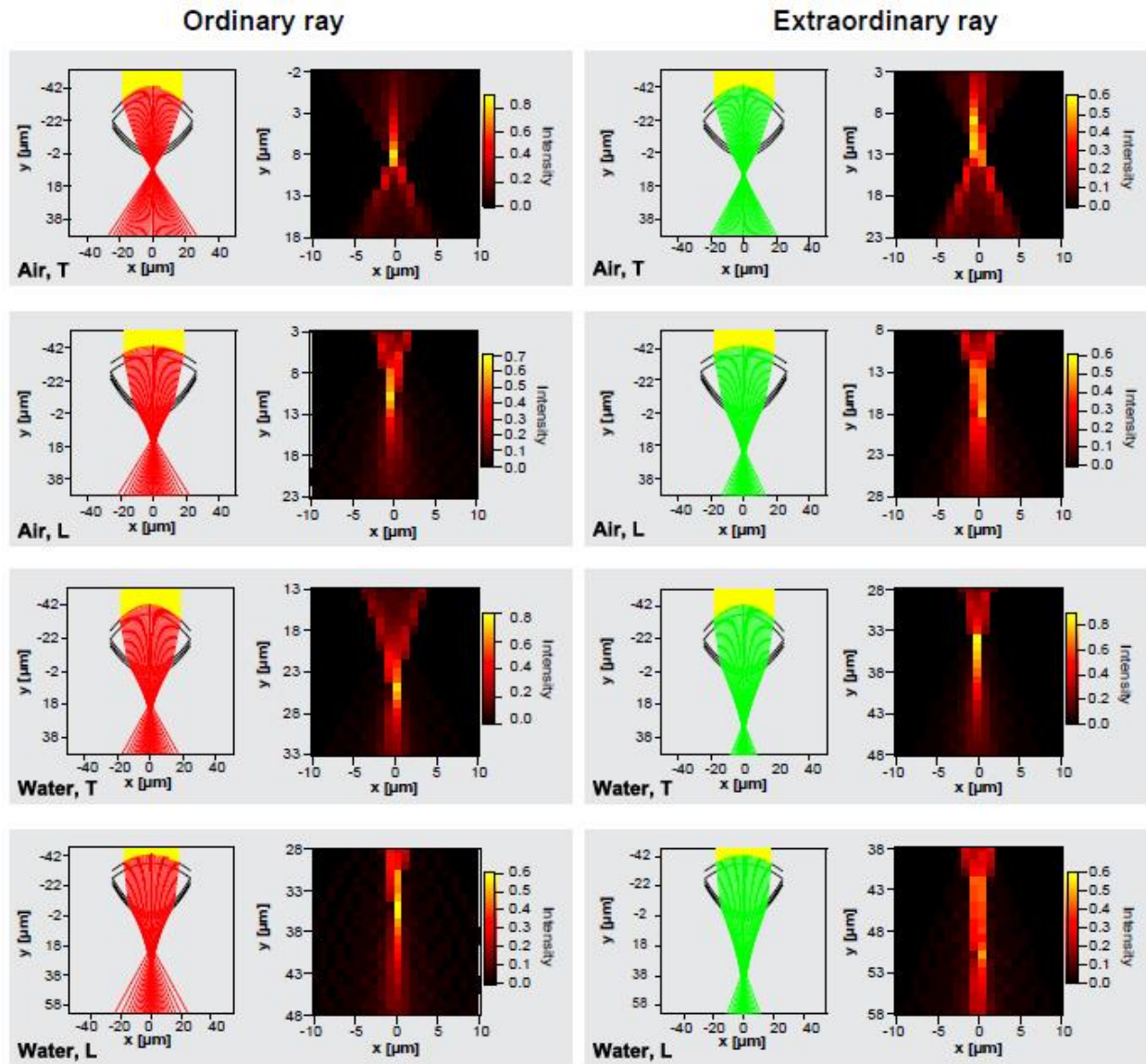
Figure 3-15 | 2D ray-trace simulations of an eye of the chiton *A. granulata*. "Air" and "Water" indicate external environments of air and seawater, respectively. "T" and "L" indicate transverse and longitudinal cross-sectional geometries, respectively.
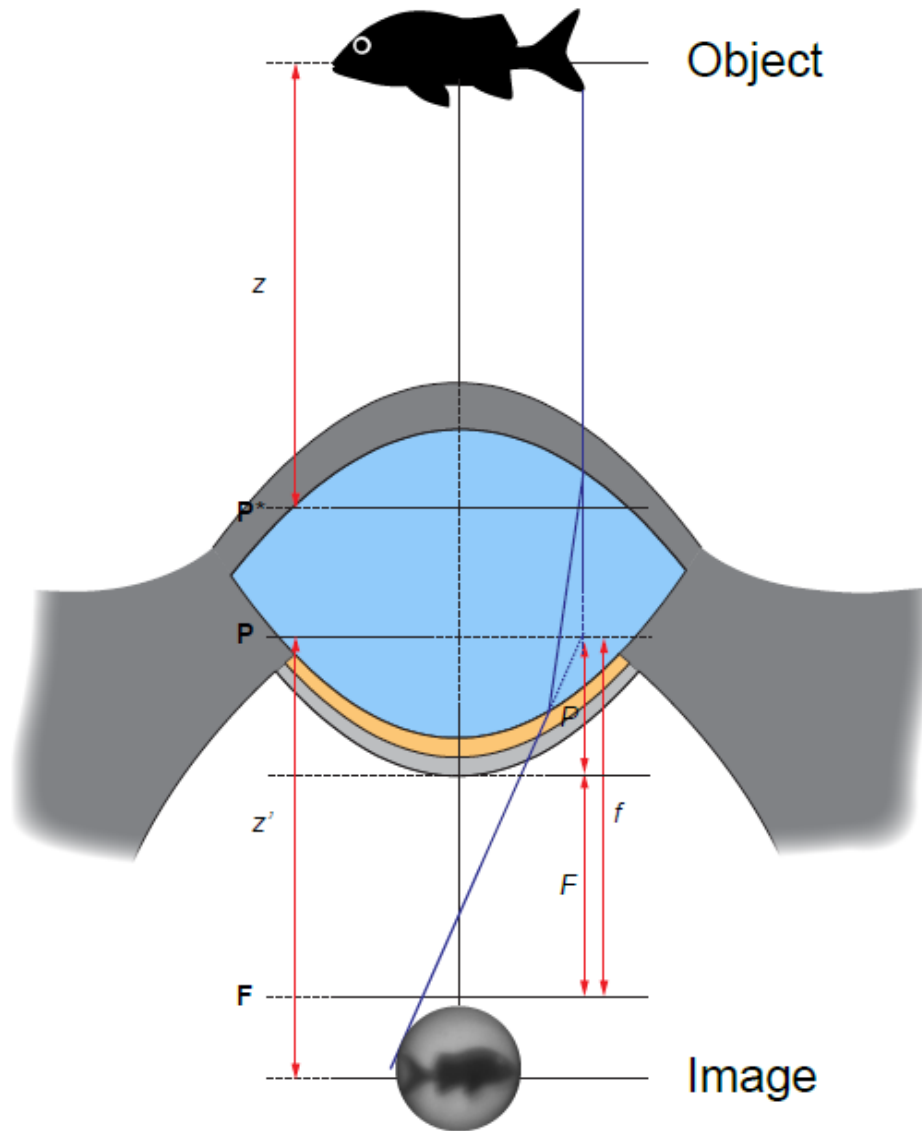
Figure 3-16| Schematic diagram of the thick lens system of an eye. Abbreviations: *F*, rear focal point; *f*, rear focal length; *P*, rear principal point; *P**, front principal point; *z'*, image distance; *z*, object distance.

The entrance pupil diameter of the lens, *D*, was determined to be ~40 μm by means of ray-tracing (Table 3-1). *D* was used to calculate the F-number of an individual eye via F-number = f/D[141], where *f* is the rear focal length. The average resultant F-number, ~1.2, is similar to that of common fish eyes[148]. We also determined the sensitivity, *S*, to be between 0.2-1.2 μm² sr (see method 3.2.16). This range is typical of diurnal shore-dwelling invertebrates such as the crab *Leptograpsus*[142]. Ray-tracing was also used to calculate the field of view of an individual eye (see method 3.2.12 and Fig. 3-2). The full-angle field of view, 2α, ranges between 60-75°. All the metrics of optical performance derived from ray-trace simulations are summarized in Table 3-1.

Cross Section, Polarization	F (µm)	Astigmatism (µm)	P (µm)	f (µm)	2α (°)	s($\Delta\phi$=9°) (µm)	$\Delta\phi$(s=7 µm) (°)	D (µm)	F-number	S (µm² sr)
In Air:										
Transverse, Ordinary	8		23	31	70	5	13	41	0.8	1.2
Longitudinal, Ordinary	21	13	18	39	75	6	10	38	1.0	0.6
Transverse, Extraordinary	12		25	37	70	6	11	38	1.0	0.7
Longitudinal, Extraordinary	28	16	21	49	70	8	8	37	1.3	0.4
In Seawater:										
Transverse, Ordinary	25		17	42	70	7	9	40	1.1	0.6
Longitudinal, Ordinary	35	10	13	48	75	8	8	38	1.3	0.4
Transverse, Extraordinary	34		18	52	60	8	8	40	1.3	0.4
Longitudinal, Extraordinary	51	17	14	65	60	10	6	38	1.7	0.2

Table 3-1| Metrics of the optical performance of individual eyes of the chiton *Acanthopleura granulata* derived from 2D ray-trace simulations. Abbreviations: F, rear focal point; P, rear principal point; f, rear focal length; α, half-angle field of view; s($\Delta\phi$=9°), photoreceptor spacing required to generate an angular resolution of 9°; $\Delta\phi$(s=7 µm), angular resolution assuming a photoreceptor spacing of 7 µm; D, entrance pupil diameter; S, sensitivity.

Since the small size of the eyes[73], which range in diameter from approximately 25 to 75 μm in the genus *Acanthopleura*[149], and perceived curvature of the lenses[144] have cast doubt on their ability to form images, I decided to experimentally investigate. Images representative of side profiles of potential predators were projected through individual lenses (Fig. 3-17a). The middle image of Fig. 3-17a demonstrates that the lenses can indeed form clear images. This image is analogous to that which would be produced by a 20 cm long fish that is 30 cm away from the chiton. However, the bottom pixelated image of Fig. 3-17a represents what each eye is physiologically capable of resolving, since image quality is constrained by the width of each photoreceptor, s, which is ~7 μm[80]. This suggests that the maximum distance at which *A. granulata* can spatially resolve a 20 cm object is ~2 m, since at this object distance the image will be approximately the size of a single photoreceptor.

The clear images produced by individual lenses allowed us to test the accuracy of our ray-trace simulations. We determined the rear focal length, f, by measuring the dimensions of images produced from a known object at a variety of object distances (Fig. 3-17b). Submerging the lenses in water, we obtained $f = 72 \pm 17$ μm, which is comparable to maximum value of f, 65 μm, determined from ray-trace simulations (Fig. 3-18).

Double refraction was clearly observed during image formation experiments (Fig. 3-19), but not consistently. This may be because the optical axes of the lens and microscope were not aligned parallel in each trial. Similarly, the extent of astigmatism observed was variable, presumably because we did not know the orientation of the transverse and longitudinal directions of each lens relative to the horizontal and vertical lines of our test objects. However, the maximum astigmatism observed, $\Delta F = 19$ μm, is consistent with the maximum, $\Delta F = 17$ μm, predicted by our ray-trace simulations.

$$\frac{1}{M} = \frac{z}{f} + \left(\frac{z_o + P^*}{f} - 1 \right)$$
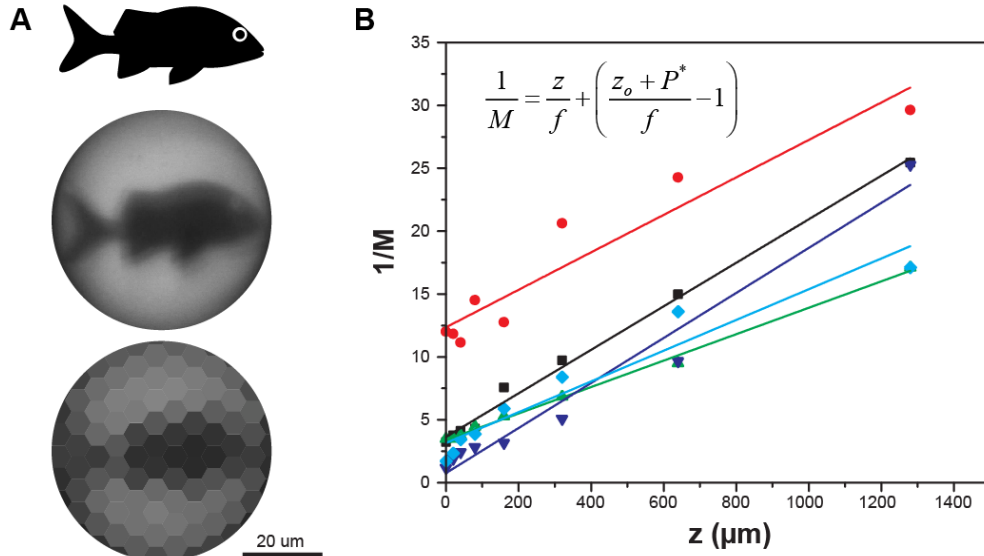
Figure 3-17| Image formation capacity and focal length measurements of individual eyes. **a**, Image formation ability of a single lens. Top, the object (mask) used, which represents the side profile of a predatory fish. Middle, raw image formed by a lens. Bottom, physiological image resolution. Each hexagonal pixel is approximately the size of a single photoreceptor. **b**, Experimental measurements of the rear focal length, *f*, of 5 individual lenses derived from the slope of inverse magnification, 1/M, vs. object distance, z.
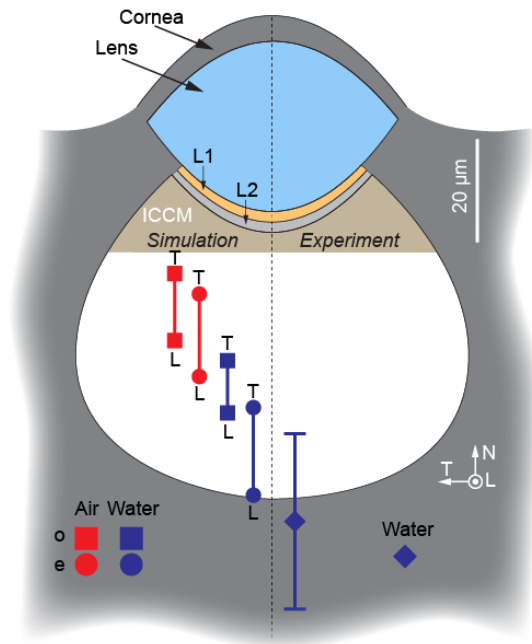
Figure 3-18| Comparison of the locations of the rear focal points of an individual eye determined from ray-trace simulations and experiments. Simulated and experimentally measured values are on the left and right of the optical axis, respectively. The red or blue color of each point signifies an external environment of air or water, respectively. "T" and "L" indicate the cross-sectional geometry simulated. The square and circle symbols correspond to the ordinary, "o", and extraordinary, "e", rays, respectively.

62
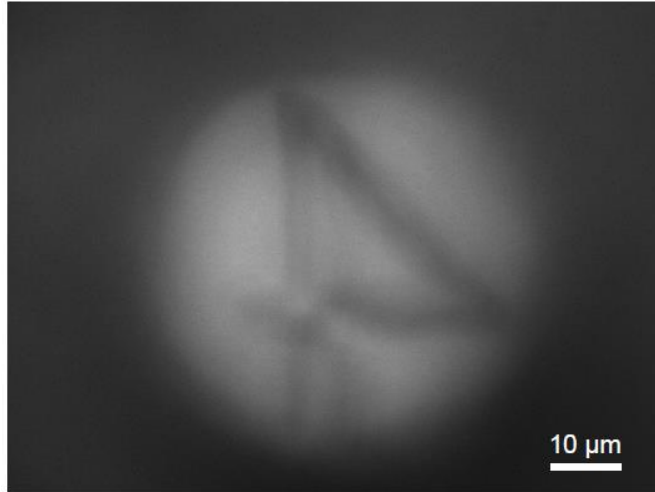
Figure 3-19| Double image of the number "4" produced by the birefringent lens of an eye of the chiton *A. granulata.*

3.3.4 Mechanical Performance of the Multifunctional Armor

The integration of sensory structures introduces large, localized volumes of soft sensory tissue of the outer shell layer, and modifies its aragonite-based granular microstructure at the intrinsic material level. We hypothesized these changes might affect the mechanical robustness of the shell, which is surely critical to the survival of *A. granulata*. To test this hypothesis, we investigated the mechanical behavior of the sensory and non-sensory regions of outer shell layer with instrumented indentation at two length scales (Fig. 3-20). At the ~5 μm scale, although both the lens and surrounding granular microstructure exhibit a similar indentation modulus (E_{O-P} ~70 GPa) and hardness (H_{O-P} ~5 GPa) (Fig. 3-21), nanoindentation with a sharp conospherical tip induces radial cracking in the lens, but not in the granular microstructure (Fig. 3-20a and b). To probe the mechanical behavior on the scale of the entire sensory structures (~50 μm), we used a flat punch tip to perform "crush" experiments on the eyes, megalaesthetes, and solid non-sensory regions (Fig. 3-20c). As illustrated by the load-depth curves in Fig. 3-20d, compression of eyes first induced gradual fracture of the protective corneal layer (Fig. 3-20d, inset), and eventually led to catastrophic failure by pushing the entire lens into the chamber of the eye, as shown in the post-test SEM image (Fig. 3-20e). The average load for catastrophic failure was slightly less than 1 N (0.84 ± 0.11 N, n = 5). Using a maximum load of 1 N, the megalaesthetes exhibited step-wise micro-fracture up to the maximum load without catastrophic failure (Fig. 3-20f). Identical indentation experiments on the solid non-sensory protrusions induced relatively small amounts of permanent deformation, demonstrating their greater mechanical integrity (Fig. 3-20g).
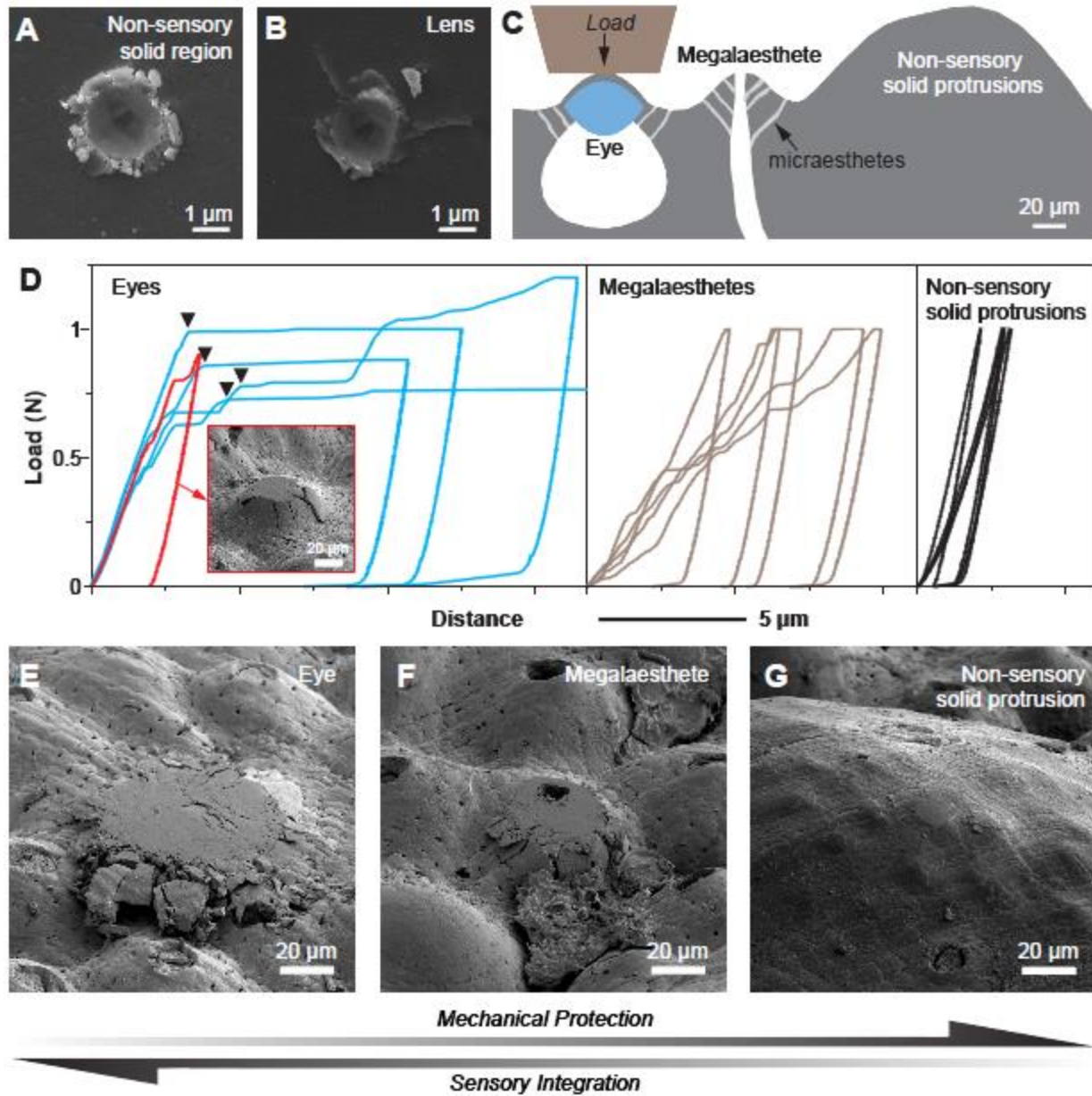
Figure 3-20| Trade-offs between mechanical protection and sensory integration. **a** and **b**, SEM images of residual indents in a non-sensory region and lens, respectively, after nanoindentation with a conospherical tip. **c**, Schematic diagram of the three areas of the outer shell layer tested via microindentation: non-sensory regions, megalaesthetes, and eyes. **d**, Microindentation force vs. depth curves for the eyes, megalaesthetes, and non-sensory regions. The relative size and geometry of the indenter is shown in (**c**). The SEM inset shows the onset of plastic deformation in an eye region, where the cornea fractures radially. **e**-**g**, SEM images of residual indents in an eye, megalaesthete, and non-sensory region, respectively, after microindentation.
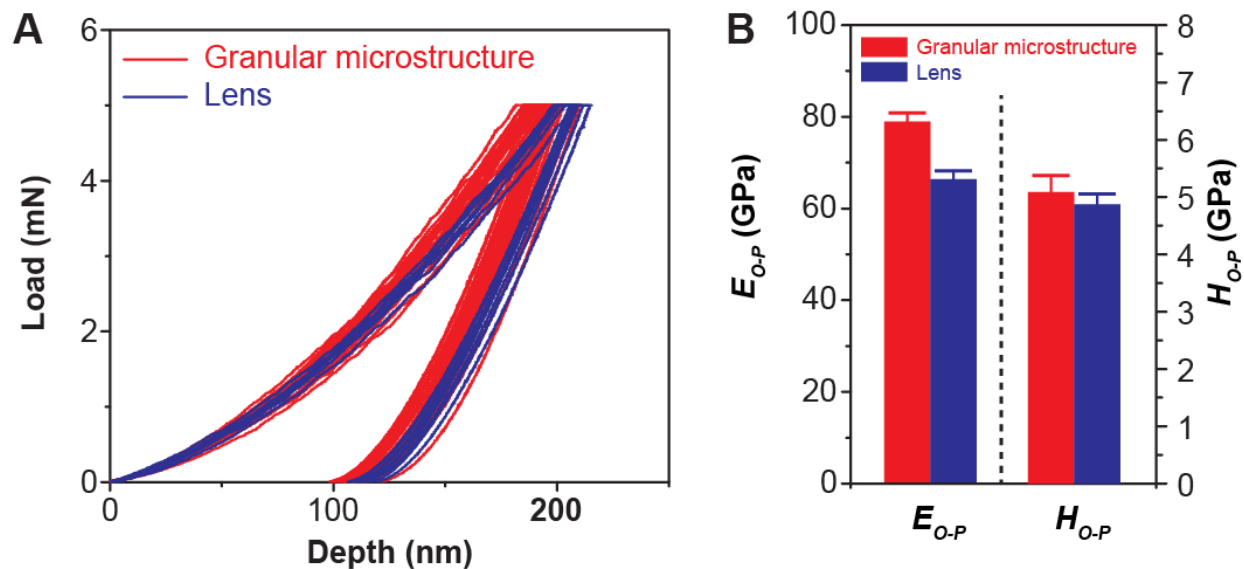
Figure 3-21| Mechanical behavior of the lens of an eye and the granular microstructure of the non-sensory regions of the outer shell layer of the chiton *A. granulata*. a, Force-depth nanoindentation curves using a Berkovich tip. SEM images of typical post-indentation residues are shown in Fig. 3-20a and b. **b**, Reduced modulus and hardness derived from the nanoindentation tests of (**a**) using the Oliver-Pharr method.

3.3.5 Trade-offs: Mechanical Protection vs. Sensory Integration

Organisms often need to perform multiple tasks that contribute to their fitness, resulting in trade-off situations[150]. These trade-offs have traditionally been discussed in the context of phenotype morphologies, e.g. the size and shape of the beaks of Darwin's finches. Our study of the structure/property/performance relationships of the shell of the chiton *A. granulata* demonstrates that trade-offs are also fundamentally present at the materials level within a single organism. The shells of chitons have evolved to satisfy two conflicting design requirements: protection and sensation. Three design aspects are fundamental to the functional integration of the sensory structures within the armor: 1) the incorporation of soft sensory tissue (creation of a porous network), 2) modification of the geometry of the armor material, and 3) material-level alteration of the armor material, which in this case is aragonite-based.

Sensory integration necessitates the incorporation of living tissue, which creates porosity. This degrades the mechanical robustness of the armor, which is seen by comparing the mechanical performance of the megalaesthetes and solid non-sensory regions. Depending on the species, megalaesthetes may serve a variety of functions including mechano-, chemo-, and/or photoreception[74]. Increasing the integrated optical

functionality from simple photoreception to spatial vision (in other words, advancing from light-sensitive megalaesthetes to eyes) requires a much larger volume of sensory tissue per sensory unit, as well as the modification of the local geometry of the armor material to form a lens. Although the eyes provide distinct optical advantages over megalaesthetes, e.g. the ability distinguish dark objects from uniform decreases in illumination, they further degrade the penetration resistance of the armor. This was demonstrated by the microindentation experiments, in which the megalaesthetes exhibited step-wise micro-fractures while the eyes failed catastrophically at less than 1 N. Furthermore, at the material-level, increasing the grain size and alignment in the lenses relative to the granular microstructure of the non-sensory regions reduces scattering and improves its ability to focus light. However, these material-level changes cause the lens to fracture radially upon nanoindentation, which is in stark contrast to the relatively isotropic, localized damage observed in the non-sensory regions. These mechanical disadvantages may constrain the size of the eyes, which could improve in both resolution and sensitivity if larger[142]. In summary, as the size and complexity of the integrated sensory elements increases, the local penetration resistance decreases.

Although functional integration decreases the overall mechanical performance of the outer shell layer, *A. granulata* has developed strategies to compensate for its vulnerabilities. First, the mechanically weak sensory regions are strategically located in the valleys created by the protruding, mechanically robust non-sensory regions. This likely protects the delicate sensory structures from blunt impacts. The protrusions may also discourage fouling to ensure that the sensory regions are not covered. Secondly, it's possible that chitons compensate for the mechanical weakness of the entire outer shell layer by having thick, hard underlying layers. This is consistent with observations of living chitons which had oyster-drill scars that penetrated the outer shell layer, but did not pierce the inner layers[152]. Lastly, the apparent redundancy of the eyes will help to reduce the impact of partial shell damage. Eyes in older parts of the shell are often damaged by erosion, and replacements are continually grown at the shell margin[77]. From a visual performance perspective, redundancy also allows *A. granulata* to simultaneously monitor the entire hemisphere for threats, which is important since the eyes are static structures and chitons can take several minutes to turn around. Redundancy can also potentially improve signal-to-noise ratio, and help *A. granulata* to distinguish false alarms from real threats[151].

4 Passive and Defensive Conformations of the Armor Plate Assembly

This chapter was published as an article in *The Journal of Structural Biology* in 2012[94].

4.1 Introduction

Chitons are of great interest from a biomechanical perspective because instead of a single continuous shell, they possess an assembly of eight dorsal aragonite-based plates (Fig. 4-1a). The first (head) and eighth (tail) plates are semicircular in outline while the intermediate plates are butterfly-shaped. These plates provide protection while allowing for the flexibility needed to traverse uneven surfaces, as well as to roll defensively into a ball-like conformation (Fig. 4-1b) if dislodged from a surface. In many species, the head plate nearly touches the tail plate in the rolled state[95]. This defensive conformation covers and protects the soft ventral side of the chiton from imminent predation, and may allow it to be carried out of harm's way by a passing wave to a more favorable location to right itself[48,152]. The curvature of the plate assembly is most often convex, although less frequent concave curvatures have been observed. Convex flexure is provided by the ''enrolling'' muscle, which encircles the plates[153]. Plates 2–8 possess two anterior projections, the apophyses, which overlap with the ventral surface of the adjacent anterior plate. Transverse muscles lie in the overlapping regions between neighboring plates and connect them together[154].

The objectives of this study were: 1) to quantify the three-dimensional geometry of the shell plate assembly of a chiton, 2) to investigate the conformational transition of the assembly from a passive state (flattened or slightly curved, attached to a surface) to a defensive state (rolled, detached from a surface), and 3) to gain insights into the functional and physiological consequences resulting from the structure of the segmented (structurally speaking, not biologically) exoskeleton. To accomplish these goals, the chiton *Tonicella marmorea* was analyzed by X-ray micro-computed tomography (μCT) to quantify biomechanically-relevant features such as the 3D morphology of individual plates, the inter-plate connections and overlap, and the curvature and continuity of the entire plate assembly. 3D printing was employed to create a scaled-up macroscopic model directly from μCT data to better visualize the inter-plate articulation. The results are discussed in the context of other articulating segmented armor systems found in nature. Particularly, we discuss the balance between local protection mechanisms of the individual armor units and larger length scale design principles which enable the flexibility of the assembly. The new scientific information obtained holds potential for future comparative morphometric analyses of

chitons, as well as for the development of improved biologically-inspired body armor[155], especially for protection of extremities.

4.2 Materials and Methods

4.2.1 Sample Preparation and Terminology

Chitons were purchased alive from Gulf of Maine, Inc. (Pembroke, Maine) and stored frozen until experimentation. The chitons were identified as *Tonicella marmorea* and distinguished from *Tonicella rubra* by the height/width aspect ratio of the fourth plate (~0.44 vs. ~0.29), and appearance of the girdle (leathery to the naked eye vs. densely covered with club-shaped calcareous corpuscles), respectively[156]. The morphological terminology used was defined and/or standardized by E. Schwabe[59].

4.2.2 Micro-Computed Tomography (μCT)

The complete shells (plates 1-8 and girdle) of *T. marmorea* were scanned with a micro-computed tomography system (μCT40, Scanco Medical AG, Switzerland) operated at 70 kV and 114 μA. Tomographic slices were recorded every 10 μm and were reconstructed with 10 × 10 μm voxels in a plane. For the chiton displayed in Fig. 4-1a, the 3D information of the plate assembly was partitioned into contributions from each individual plate using the threshold and contour functions of Scanco MicroCT Software. For the chiton displayed Fig. 4-1b, the 3D information of the plate assembly was segmented using the threshold and region growth functions of image processing software package Mimics (Materialise, Belgium). Mimics was also used to create all three-dimensional images, including those with transparency effects. The geometric information of the plate assemblies was converted into three-dimensional triangulated surface meshes (binary STL format) using Scanco MicroCT Software for the chiton presented in Fig. 4-1a, and Mimics for the chiton presented in Fig. 4-1b. Meshes were reduced in size as needed using the smooth, reduce, and remesh tools of 3-matic (Materialise, Belgium). Cross-sectional images were created from the surface meshes using the cut function of the simulation module of Mimics. Open source image analysis software ImageJ[157] was used to make all morphometric measurements from cross-sectional images. The spatial distribution of thickness of each individual plate and of the entire plate assembly (Fig. 4-3a and b, respectively) of the chiton presented in Fig. 4-1a was calculated using a spherical method in which each point in 3D space is assigned a thickness value corresponding to the diameter of the largest sphere centered on that point which can fit within the boundaries of the object[158].

4.2.3 Calculations of Plate-to-Plate Overlap and Curvature

In Fig. 4-2f, overlap was quantized using aerial projections (in the ''y''–''z'' plane) of the plates and plate-to-plate overlapping (darkened) regions of Fig. 4-2d and e. For each intermediate plate, the total overlap percentage was calculated by summing the projected areas of the two overlapping regions (anterior and posterior), and expressing the sum as a percentage of the projected area of the entire plate which encompasses them. For the first and eighth plates, the total overlap percentage was calculated by expressing the projected area of the single overlapping region (the overlapping region of plates 1 and 2, and plates 7 and 8, respectively) as a percentage of the projected area of the entire plate. The transverse radii of curvature of individual plates and the longitudinal radii of curvature of the plate assemblies were calculated using open source ''Circle Fit (Pratt Method)'' MatLab (MathWorks, MA) code (http://www.mathworks.com/matlabcentral/fileexchange/22643) written by N. Chernov based on an algorithm developed by V. Pratt[159].

4.2.4 3D Printing

A scaled-up macroscopic prototype of the chiton shell plate assembly was fabricated using a three-dimensional printer (ZPrinter 310 Plus, ZCorporation, USA) with a plaster powder (ZP 131 powder, ZCorporation, USA). 89 μm-thick layers were laid down using a commercially available binder (ZCorporation, USA) at a vertical build speed of 25 mm/hour. After printing, the prototype was immersed in a wax bath to ensure a smooth surface.

4.3 Results

The three-dimensional structure of the shells of two representative specimens of *T. marmorea* (Fig. 4-1a and b) was derived from reconstructions of μCT data. In their curved states, the plate assemblies of the chitons seen in Fig. 4-1a and b have approximate dimensions 1.7 × 0.95 × 0.45 cm and 1.66 × 1.4 × 1.38 cm (length (''z''-direction) × width (''x''-direction) × height (''y''-direction)), respectively. The girdle, musculature, and other soft tissues of the chitons were non-mineralized and consequently did not absorb X-rays well enough to be clearly visible in the μCT data.
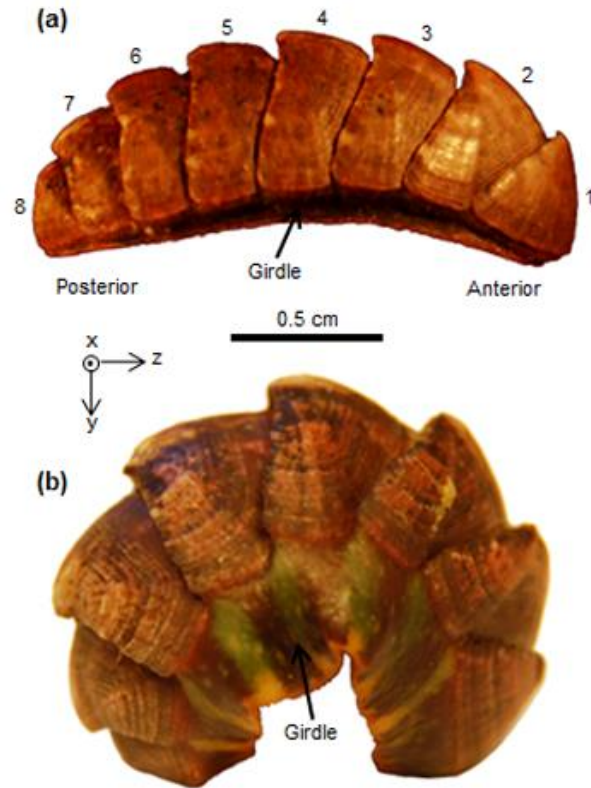
Figure 4-1 | **Side views of the chiton *Tonicella marmorea*.** **a**, Light micrograph of a dried shell in a passive state. **b**, Photograph of a recently thawed chiton in a defensive, curved posture.

Fig. 4-2a and b display dorsal and ventral views, respectively, of a μCT reconstruction of the plate assembly of the chiton seen in Fig. 4-1a, along with complementary transparent images highlighting plate-to-plate overlap (darkened regions). The broad ''u''-shape of the overlapping regions results from each plate's (with the exception of the first plate) two anterior projections, the apophyses, which each imbricate with the adjacent anterior plate and are separated by a sinus. Side profiles of μCT reconstructions of the chitons seen in Fig. 4-1a and b are shown Fig. 4-2d and e, respectively, and are accompanied by transparent images. As illustrated by the transparent image of Fig. 4-2d, in the passively conformed plate assembly with a smaller longitudinal curvature (about the "x"-axis), plate-to-plate overlap is not limited solely to the apophyses. Rather, a portion of each intermediate plate's jugal area is also involved in overlap. In contrast, overlap in the jugal areas of each intermediate plate is absent or greatly reduced in the defensively conformed plate assembly, which has a greater longitudinal curvature (Fig. 4-2e). The average total plate overlap of the defensively conformed assembly, $48.0 \pm 9.1\%$, is less than that of the passively conformed assembly, $62.3 \pm 11.5\%$ (Fig. 4-2f). In both conformations, plate-to-plate overlap decreases approximately linearly along the intermediate plates, from plate 2 to 7.
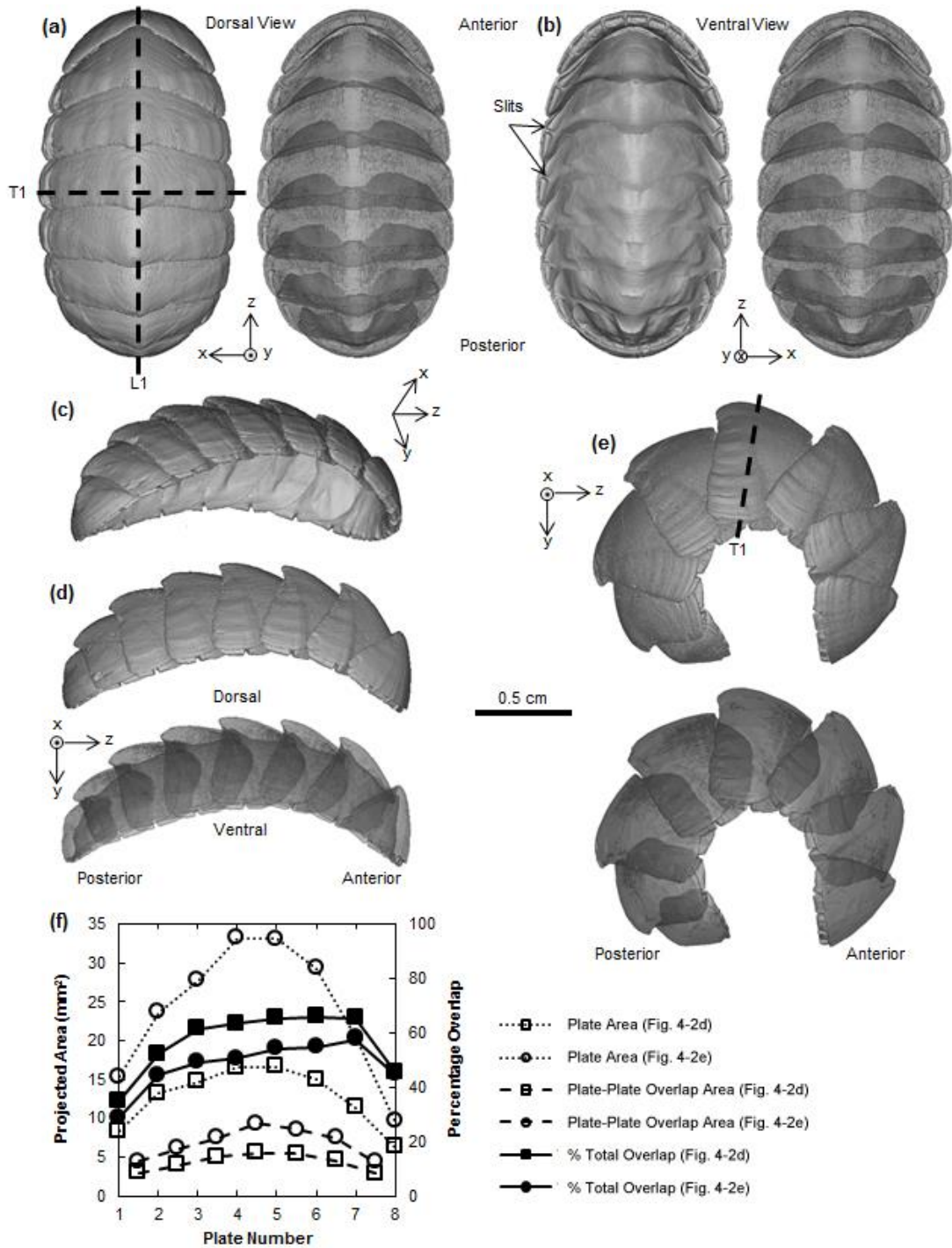
Figure 4-2| 3D μCT reconstructions of the armor plate assembly of the chiton *Tonicella marmorea* in passive and defensive conformations. **a**, Dorsal view the passive conformation displaying the positions of cross sections L1 and T1. **b**, Ventral view of the passive conformation. **c**, Side/ventral view of the passive conformation. **d**, Side view of the passive conformation. **e**, Side view of the defensive conformation displaying the position of cross section T1. (**a**-**d**) correspond to the chiton seen in Fig. 4-1a while (**e**) corresponds to the chiton seen in Fig. 4-1b. **f**, Projected area in the "y"-"z" plane (open circle and square symbols) vs. overlap percentage (filled circle and square symbols) vs. plate number. The total overlap percentage for each intermediate plate includes contributions from both neighboring plates.

71

The intermediate plates of the plate assembly of *T. marmorea* have similar spatial distributions of thickness, in which the central non-overlapping regions are thickened (~0.85 mm) relative to the anterior and posterior overlapping areas (~0.4 mm) and apophyses (~0.2 mm) (Fig. 4-3a). The thin (green) and thick (red) regions of the plate assembly (Fig. 4-3b) correlate with its overlapping and non-overlapping regions, respectively, which are highlighted in the transparent image of Fig. 4-2a. Although the thickness distribution of each plate is similar, there is an asymmetric trend in plate volume (Fig. 4-3c). The head plate is ~40% larger than the tail plate by volume. The width/height aspect ratio (average = 2.3 ± 0.2) and jugal angle (average = 103.6 ± 0.2) of the intermediate plates show little variation across the assembly.

Additional morphometric measurements of the individual plates and entire assembly are available in tables 4-1 and 4-2, respectively. The anatomical terminology and morphometric parameters of the individual plates are illustrated in Fig. 4-4. Visualization of the shape of the individual plates and their imbrication was facilitated using a scaled-up macroscopic 3D printed model of the plate assembly (Fig. 4-5). As shown in the close-up of Fig. 4-5b, a raised "hook" feature called the ventral tegmental callus lines the ventral posterior edge of each plate. This hook may prevent catastrophic separation of the intermediate plates in instances of extreme curvature.
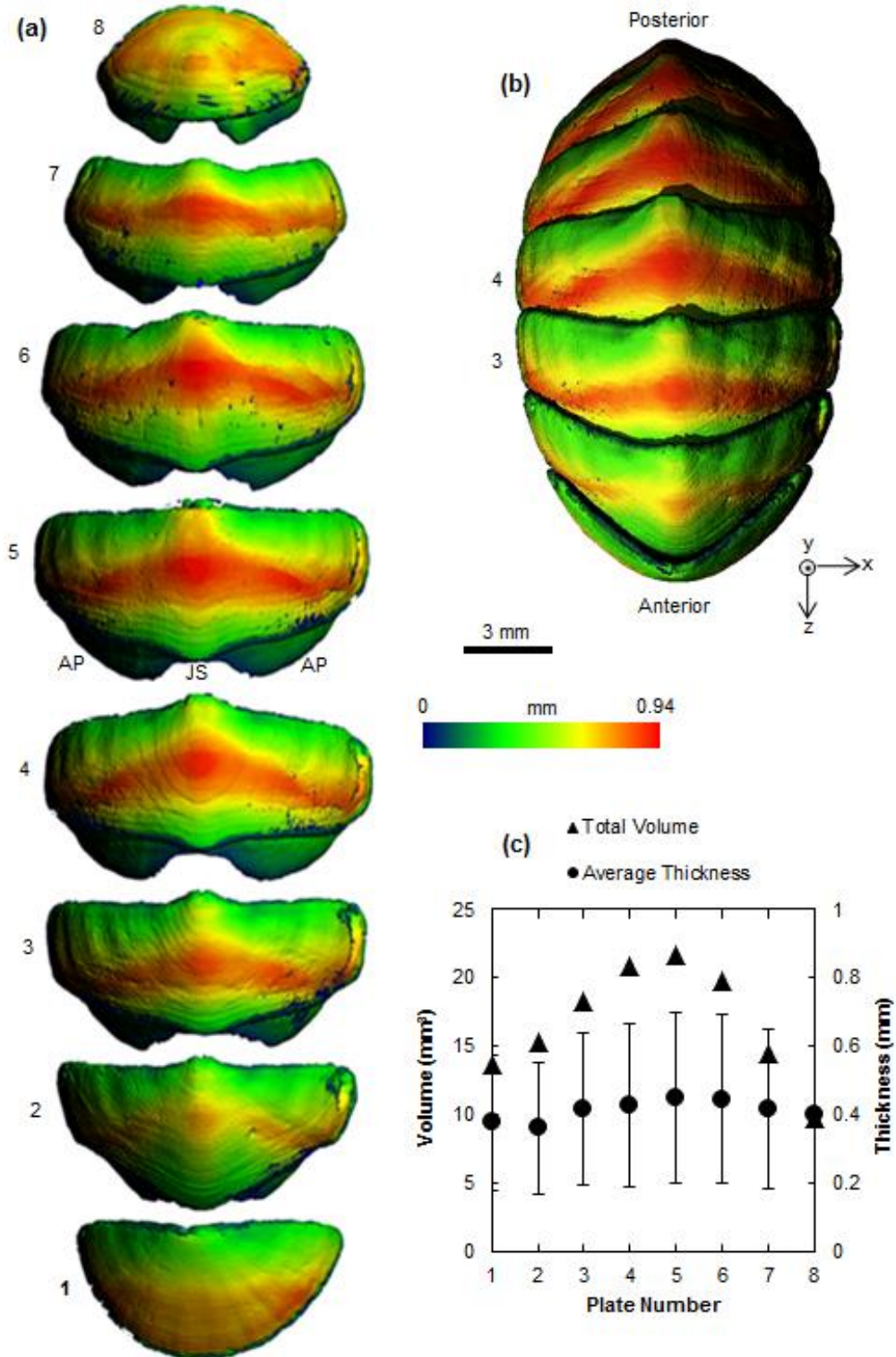
Figure 4-3 | Thickness distribution of the armor plate assembly of the chiton *Tonicella marmorea*. a and **b**, Dorsal view of the spatial distribution of thickness for each plate 1-8 and of the entire plate assembly, respectively, of the chiton seen in Fig. 4-1a. **c**, Total volume (triangle symbols) and average thickness (circle symbols) as a function of plate number. Error bars in (**c**) refer to standard deviations of the dataset. Abbreviations: AP, apophyses; JS, jugal sinus.
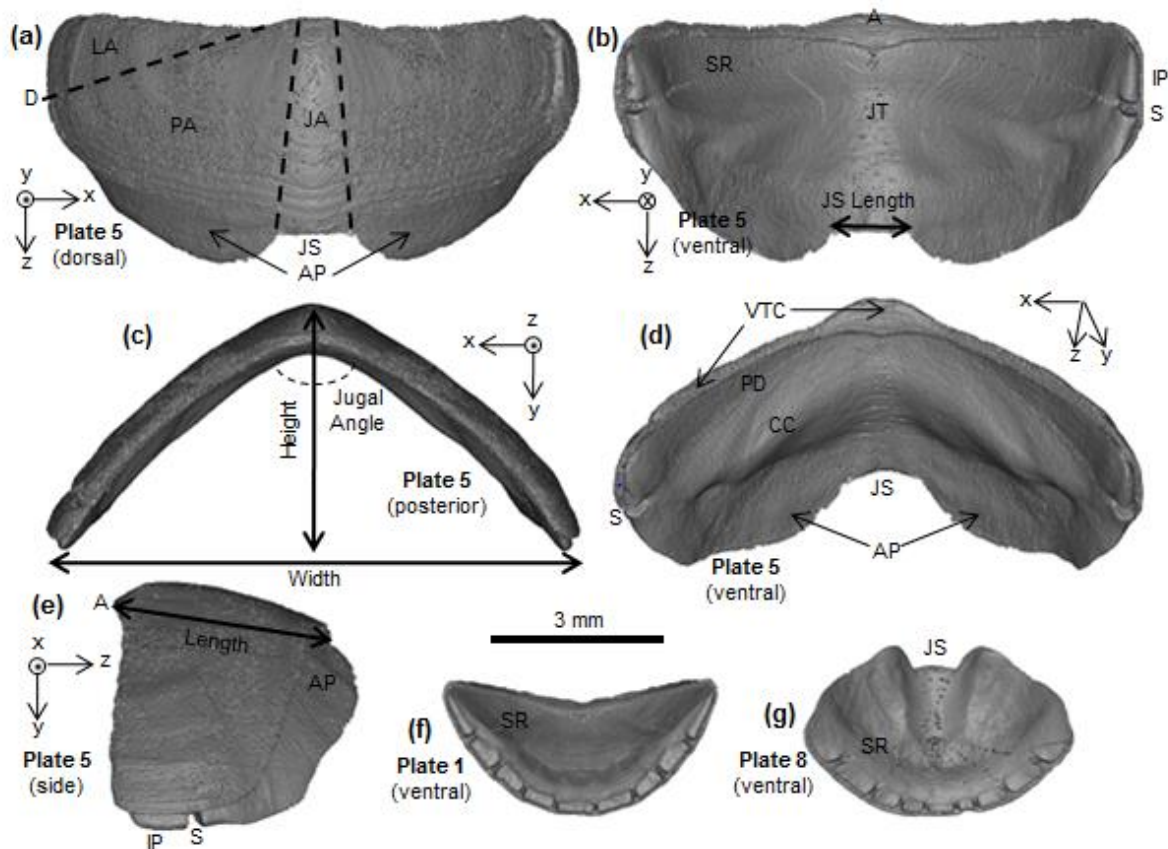
Figure 4-4| Illustrations of the anatomical terminology and morphometric parameters of the individual armor plates of the chiton *Tonicella marmorea*. a, Dorsal view of plate 5. **b**, Ventral view of plate 5. **c**, Posterior view of plate 5. **d**, Ventral/posterior view of plate 5. **e**, Side view of plate 5. **f**, Ventral view of plate 1. **g**, Ventral view of plate 8. Terminology: AP, Apophyses; CC, Central Callus; D, Diagonal; JA, Jugal Area; JS, Jugal Sinus; JT, Jugal Tract; LA, Lateral Area; PA, Pleural Area; PD, Posterior Depression; S, Slit; SR, Slit Ray; VTC, Ventral Tegmental Callus.

Plate #	Average Thickness (µm)	Total Volume (mm³)	Surface Area (mm²)	Width (mm)	Height (mm)	Length (mm)	Jugal Sinus Length (mm)	Jugal Angle (deg.)
1	376 ± 200	13.60	92.21	7.50	3.12	3.85	-	104.4
2	361 ± 192	15.29	140.73	8.73	3.92	4.17	2.51	103.6
3	416 ± 224	18.24	163.95	9.33	4.30	3.60	2.00	100.6
4	428 ± 237	20.86	191.53	9.67	4.51	3.96	1.53	100.4
5	447 ± 249	21.59	196.61	9.66	4.51	3.98	1.50	102.4
6	445 ± 246	19.79	172.30	9.16	4.27	3.93	1.53	104.3
7	416 ± 232	14.41	122.59	8.10	3.58	3.22	1.15	109.7
8	400 ± 199	9.69	67.59	5.97	2.22	3.17	0.97	-

Table 4-1| Morphometric measurements of the individual armor plates of the chiton *Tonicella marmorea*. Measurements were made from a µCT reconstruction of the chiton seen in Fig. 4-1a.

Thickness (µm)	411 ± 31
Thickness SD (µm)	222 ± 23
Total Volume (mm³)	16.68 ± 4.13
Surface Area (mm²)	143.44 ± 46.62
Width (mm)	8.52 ± 1.28
Height (mm)	3.80 ± 0.80
Length (mm)	3.79 ± 0.36
Aspect Ratio (Height/Width)	0.44 ± 0.03
Jugal Angle (deg.)	103.6 ± 3.1

Table 4-2 | Average morphometric measurements of the eight armor plates of the chiton *Tonicella marmorea*. Measurements were made from a µCT reconstruction of the chiton seen in Fig. 4-1a.
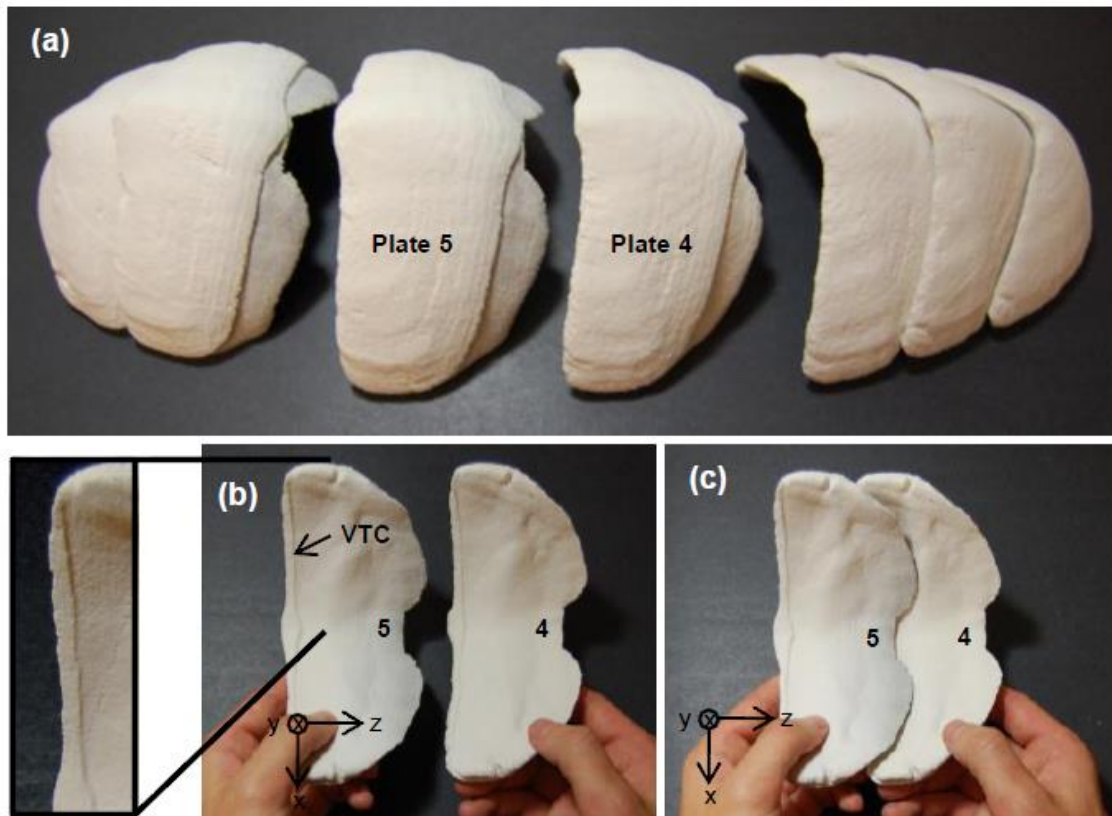
Figure 4-5 | 3D printed model of the armor plate assembly of the chiton *Tonicella marmorea*. a, Dorsal/side view of the assembly with plates 4 and 5 separated. **b,** Ventral view of plates 4 and 5 separated, including a close-up of the ventral tegmental callus. **c,** Ventral view of the overlap between plates 4 and 5. The model was printed using µCT data of the chiton presented in Fig. 4-1a. Abbreviations: VTC, ventral tegmental callus.

Fig. 4-6a and b show the L1 cross sections of the plate assembly of *T. marmorea* in passive and defense conformations, respectively. L1 bisects the jugal sinus of plates 2–8, so the apophyses are absent from the cross sections. In the passive conformation of the plate assembly (Fig. 4-6a), which has a smaller longitudinal curvature, the heterogeneous cross-sectional geometry of the plates results in relatively uniform thickness and continuous curvature of the plate assembly as a whole. To approximate the longitudinal (about the ''x''-axis) radii of curvature, 16 landmark points were selected from each assembly: the two end points of each of the eight plates in the L1 cross section. As illustrated in Fig. 4-6c and d, circles were fit to these sets of points using a direct least squares fitting algorithm[159]. The longitudinal radii of curvature of the L1 cross sections of the plate assemblies of *T. marmorea* in passive (Fig. 4-6c) and defensive (Fig. 4-6d) conformations were 9.2 and 7.4 mm, respectively. The transverse (about the ''z''-axis) radius of curvature of the fourth plate of each assembly was approximated using the same method. Eleven landmark points from cross section T1 were used to fit each plate: the midpoint of cross section L1, the midpoints of cross sections L2–L5 on the left side of the plate and their analogous midpoints on the right side, and the left and right base points of the insertion plates (Fig. 4-7a and b). The transverse radii of curvature of the T1 cross sections of the fourth plates seen in Fig. 4-7a and b were 4.6 and 6.7 mm, respectively. To compare the curvatures of the two plate assemblies and account for the size disparity, two curvature indices were defined (Fig. 4-6f). The first index, the longitudinal curvature index (L.C.I), is defined as the length of plate 4 divided by the longitudinal radius of curvature of the plate assembly in cross section L1. This definition yields L.C.I values of 0.43 and 0.70 for the passive and defensive conformations, respectively. The second index, the transverse curvature index (T.C.I), is defined as the width of plate 4 divided by its transverse radius of curvature in cross section T1. This definition yields T.C.I. values of 0.48 and 0.50 for the fourth plates seen in Fig. 4-7a and b, respectively.
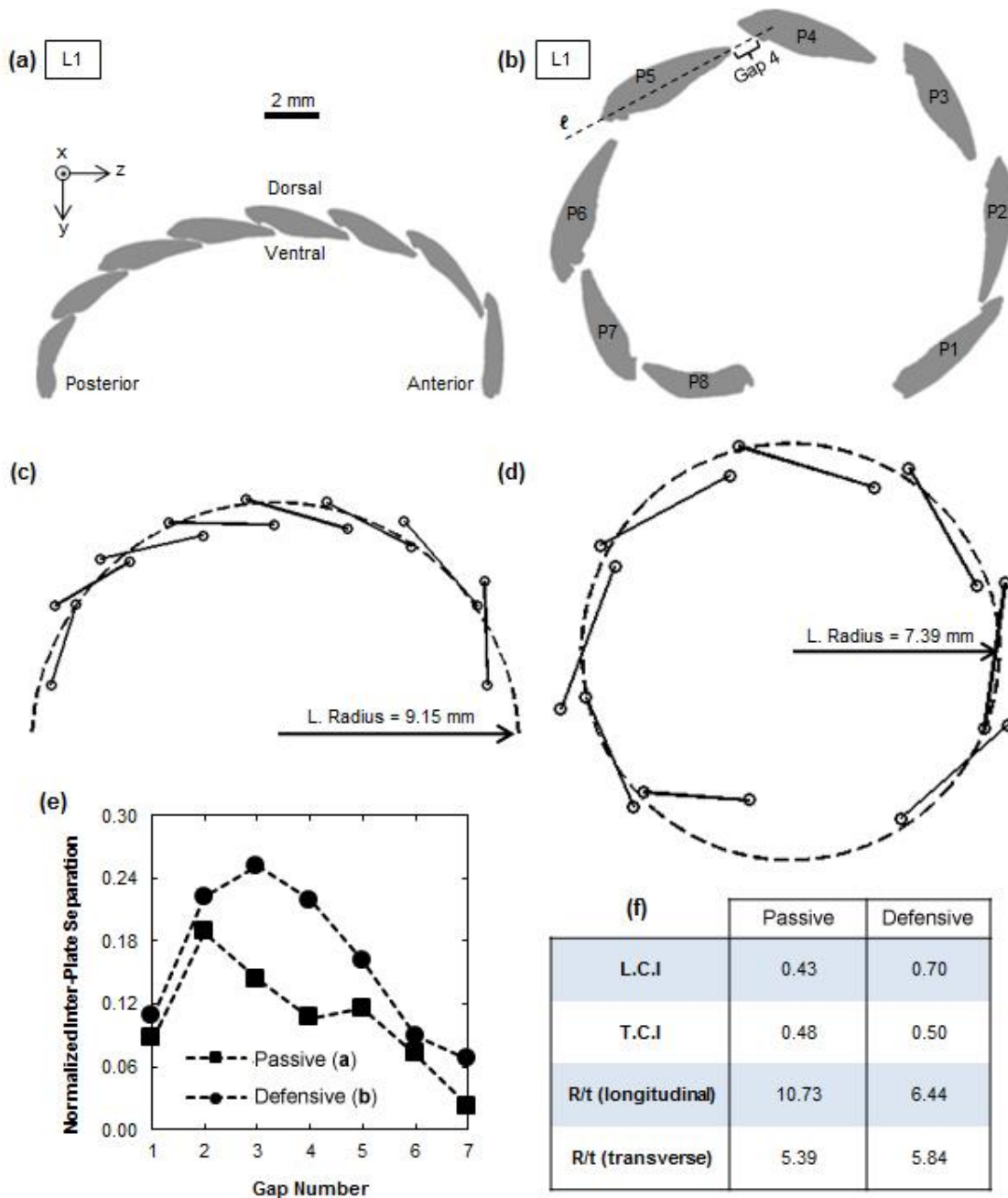
Figure 4-6| L1 (longitudinal bisector) cross-sectional geometry of the armor plate assembly of the chiton *Tonicella marmorea*. a and **b**, L1 cross-sectional geometry of the passive and defensive conformations, respectively. **c** and **d**, Circles fit to 16 landmark points from each assembly. **e**, Normalized inter-plate separation distance vs. gap number. Gap number ''n'' corresponds to the gap between plate number ''n'' and ''n + 1''. The inter-plate separation distance of gap ''n'' was measured along the long axis of plate number ''n + 1'', and normalized by dividing by the length of the fourth plate of the respective assembly. **f**, Curvature indices and shell thickness ratios. The L.C.I is calculated by dividing the length of plate 4 by the longitudinal radius of curvature of the plate assembly in cross section L1. The T.C.I is calculated by dividing the width of plate 4 by its transverse radius of curvature in cross section T1. Abbreviations: L.C.I., longitudinal curvature index; T.C.I., transverse curvature index; R, radius of curvature; t, average thickness.

77

Fig. 4-6e shows how the inter-plate separation distance changes as a function of gap number for the plate assemblies in the passive and defensive conformations. Gap number "n" corresponds to the gap between plate number "n" and "n+1". The inter-plate separation distance of gap "n" was measured along the long axis of plate number "n+1" in cross section L1. For example, the separation distance between plates 4 and 5 (gap 4) was measured along the long axis, ℓ, of plate 5 (Fig. 4-6b). To account for the size disparity between the two assemblies, the separation distances were normalized by dividing each one on by the length of the fourth plate of the respective assembly. As seen in Fig. 4-6e, the normalized separation distances of gaps 1 and 2 are similar in both plate assemblies. However, the normalized separation distances of gaps 3, 4, and 7 are approximately 75%, 100%, and 200% greater, respectively, in the defensive conformation (Fig. 4-6b) relative to the passive conformation (Fig. 4-6a). The normalized separation distances of gaps 5 and 6 are also larger in the defensive conformation, although the increase is not as pronounced. In both conformations, the trend of normalized separation distance vs. gap number is asymmetric; the separation distance of gap 2 is ~160% larger than that of gap 6.

The tops of Fig. 4-7a and b show the geometry of the T1 cross section of the plate assemblies in the passive and defensive conformations, respectively. Transverse cross section T1 was taken in the region in which plates four and five overlap. Longitudinal cross sections L2-L5 were taken at 20% increments along the line segment which runs diagonally from the midpoint of cross section L1 to the lateral edge of plate 4. A similar line segment was named k by J. Bergenhayn[97], so we adopt this notation (Fig. 4-7a). Fig. 4-7c displays how the cross-sectional overlap percentage evolves laterally from L1 to L5. In both the passive and defensive conformations, overlap is heterogeneous in nature, although the heterogeneity is more pronounced in the defensive conformation. The total overlap percentage of the fourth plate of the passive conformation is ~60% in cross sections L1 and L2, and ~82.5% in cross sections L3-L5. In contrast, the total overlap percentage of the fourth plate of the defensive conformation is ~0% in cross sections L1 and L2, and increases approximately linearly from ~50% to ~90% across cross sections L3-L5. In addition, the average total overlap of the fourth plate of the defensive conformation, ~45%, is much less than that of the passive conformation, ~75%.
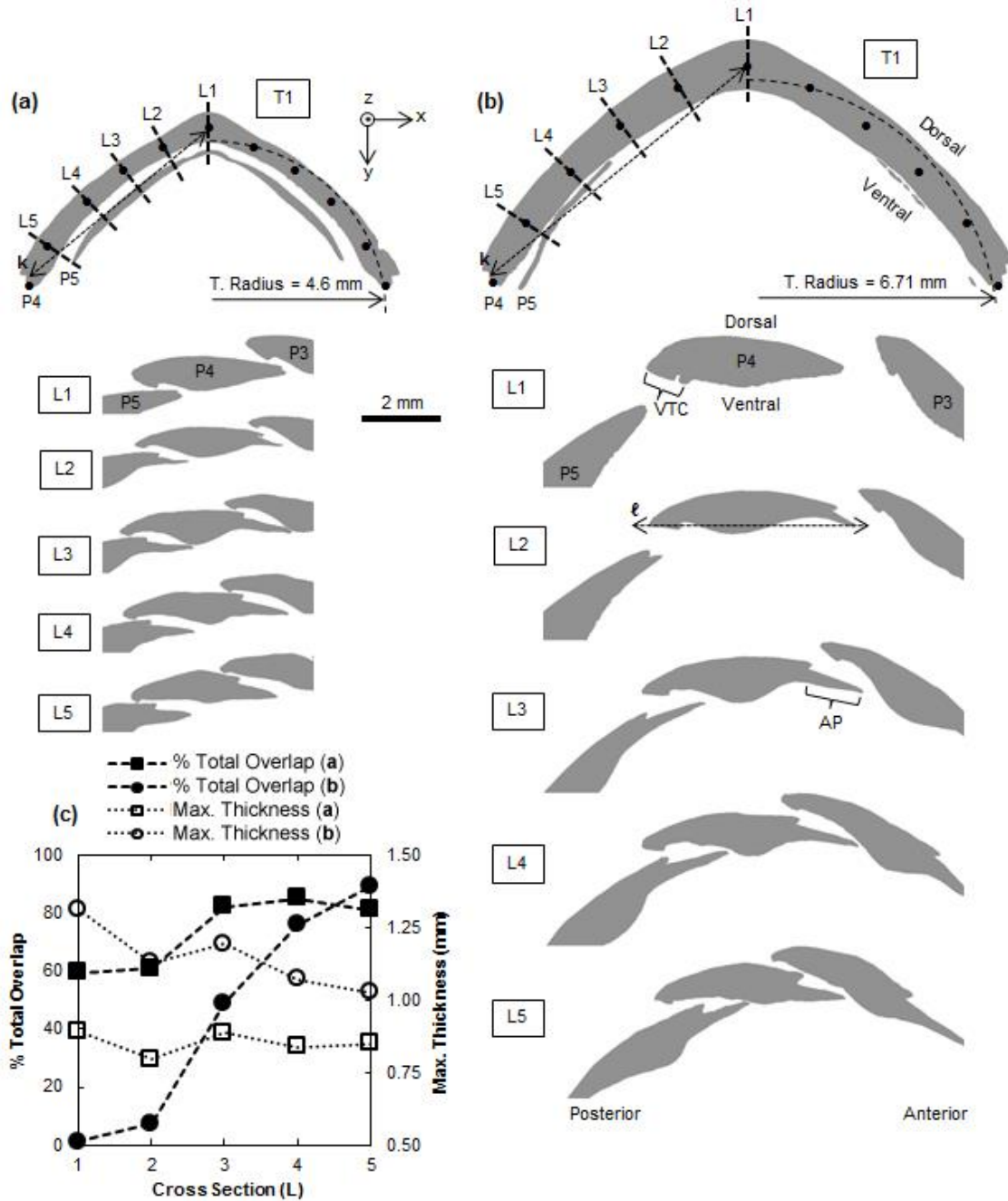
Figure 4-7 | Cross-sectional morphology of the armor plate assembly of the chiton *Tonicella mamorea*. Top of **a** and **b**, T1 transverse cross sections of passive and defensive conformations, respectively. Black circles indicate the eleven points used to calculate the transverse radii of curvature. Bottom of **a** and **b**, Morphology of the longitudinal cross sections L1-L5 of plate 4 of each assembly. Cross sections L1–L5 were taken at 20% increments along line segment *k*. **c**, Total overlap percentage and maximum thickness of plate 4 vs. longitudinal cross section number. Total overlap percentage was calculated by projecting the overlapping regions of plates 3 and 5 onto the long axis, ℓ, of plate 4, summing the two projected lengths, and expressing the sum as a percentage of the entire cross-sectional length of plate 4. Maximum cross-sectional thickness was measured perpendicular to ℓ. Abbreviations: AP, apophyses; VTC, ventral tegmental callus.

79

4.4 Discussion

In order to understand the functional designs of natural armor systems, it is important to consider that environment and types of predatory attacks experienced by the animal. Fields observations led P. Langer to suspect that the primary predators of *T. marmorea* were the sea star *Leptasterias littoralis* in shallow water (less than 6 m) and the wrasse *Tautogolabrus adspersus* and winter flounder *Pseudopleuronectes americanus* at greater depths[160]. Secondary predators include the crabs *Cancer borealis* and *Cancer irroratus*, and the lobster *Homarus americanus*. Possible predatory attacks include biting (fish), pinching with claws (lobsters and crabs), drilling with radulas (sea snails), inserting the cardiac stomach underneath or between the shell plates (sea stars), and smashing against rocks (birds).

Here we discuss the critical design aspects of the armor plate assembly of the chiton *T. marmorea*, including 1) the geometric design of the individual armor units, 2) the interconnections between armor units, and 3) the extent and heterogeneity of armor unit overlap.

4.4.1 Geometric Design Aspects of the Armor Units

The transverse curvature of the chitons plates, as observed cross sections parallel to the "x"-"y" plane, provides an arch-enhanced stiffness to resist bending from both top and lateral loading conditions. This geometric enhancement to mechanical robustness is consistent with the thickness distribution of the articulamentum and hypostracum layers of the intermediate plates (Fig. 2-1). In less curved conformations (e.g. when attached to a flat substrate) the cross-sectional shape of each plate, as observed in sections parallel to the "y"-"z" plane, creates a nearly continuous curved outer surface of the plate assembly. The centrally thickened heterogeneous cross-sectional shape of each plate, as observed in sections parallel to the "y"-"z" plane, generates a spatially uniform thickness of the plate assembly. This effect has also been observed in other segmented natural armor systems, including the lateral plate assembly of the marine three spine stickleback *Gasterosteus aculeatus*[161], and is likely a universal design principle. The continuous curvature and uniform thickness of the plate assembly geometrically enhance coverage and protection from penetration, bending, and pinching attacks.

4.4.2 The Interconnections between Armor Units

In contrast to the physically interconnected joints observed in a variety other segmented biological exoskeletons (e.g. the peg-and-socket joint of the scales the fish *Polypterus*

senegalus[162], the sliding hinge/ellipsoidal joint of the lateral plates of the marine three spine stickleback *Gasterosteus aculeatus*[161], and the ball-and-socket joint of sea urchin spines[163]), the chiton *T. marmorea* achieves motion by utilizing sandwich structures, each consisting of two rigid armor plates separated by a more compliant and actuating transverse muscle. Each transverse muscle is protected by a ventral tegmental callus, which likely functions to reduce the dorsal separation distance between adjacent intermediate plates. The contact of each pair of apophyses with the ventral surface of their anteriorly neighboring plate migrates laterally as the longitundal curvature of the plate assembly increases. The close proximity of the overlapping regions of adjacent plates appears to constrain the degrees of the freedom of the intermediate plates, particularly limiting translation parallel to the "x"-axis and rotation about the "y"-axis. Translation of the plates parallel to the "z"-axis is likely limited by the compliance of the underlying muscular system and surrounding girdle. Although the defensive conformation of the plate assembly protects the underlying soft parts of *T. mamorea* from potential predators, it creates local regions of vulnerability by dramatically increasing the size of inter-plate gaps 3 and 4 by 75% and 100%, respectively, relative to the passive conformation (Fig. 4-6e). This is consistent with observations that sea stars are capable of inserting their cardiac stomachs into the gaps between the plates of chitons that rolled into a ball after being captured[164].

4.4.3 The Extent and Heterogeneity of Armor Unit Overlap

As the L.C.I. of the plate assembly increases, plate-to-plate overlap decreases and becomes more heterogeneous. In the two plate assemblies with L.C.I. of 0.43 and 0.70, the total cross-sectional overlap percentage of the fourth plate ranged from approximately 60–82.5% (average = 73.9%) and 0–90% (average = 44.6%), respectively, between cross sections L1-L5. In addition, the average plate-to-plate overlap percentages (calculated from projections of the plates and overlapping regions onto the "y"-"z" plane) of the plate assemblies with L.C.I. of 0.43 and 0.70 were 62.3 ± 11.5 and 48.0 ± 9.1, respectively. The reduction of plate-to-plate overlap, along with the aforementioned increase in plate-to-plate separation distance, reduces the protectiveness of the plate assembly in the defensive conformation relative to less curved states. When dislodged and turned upside down by hand or an aquarium water jet, species *Cryptochiton stelleri* and *Chiton virgulatus* have occasionally exhibited a righting behavior in which the plate assemblies undergo a concave curvature and slight twisting motion. However, *Cryptochiton stelleri* always rolled into ball when dislodged and vigorously stimulated by touch. Perhaps in some species the defensive conformation serves as a last resort in the presence of an imminent threat when the chiton does not have enough time and/or security to right itself when dislodged.

4.5 Conclusion

This chapter elucidated the detailed mechanism of conformational change of the shell plate assembly of the chiton *T. marmorea* from a passive (flattened or slightly curved, attached to surface) to a defensive (rolled, detached from surface) state. The passive and defensive conformations exhibited differences in longitudinal curvature index (0.43 vs. 0.70), average plate-to-plate overlap (~62% vs. ~48%), cross-sectional overlap heterogeneity (60–82.5% vs. 0–90%, fourth plate), and plate-to-plate separation distance (100% increase in normalized separation distance between plates 4 and 5), respectively. In contrast to physically interconnected joints observed in some other natural segmented armors (e.g. peg-and-socket and ball-and-socket), *T. marmorea* achieves motion by utilizing sandwich structures, each consisting of two rigid armor plates separated by a more compliant and actuating transverse muscle. The sandwich structure is analogous to an engineering shear lap joint, albeit one that is geometrically structured. This work also provides an understanding of how *T. marmorea* achieves the required balance between mobility and protection in the passive and defensive states. In the passive state, the shape of the individual shell plates and plate-to-plate interconnections results in an approximately continuous curvature and constant armor thickness and, hence, spatially homogeneous protection. Mobility is limited but armor coverage and protection is maximized. When the chiton is detached from a surface and in the defensive state, the underlying soft tissues of the foot are covered and protected by the shell plates and the animal gains mobility through tidal flow, but regions of vulnerability are opened dorsally, due to increases in plate-to-plate separation distances and decreases in plate-to-plate overlap.

5 Comparative Morphology and Biomechanics of Chiton Scale Armor

5.1 Introduction

In certain chiton species, the tough tissue surrounding the shell plates is covered by overlapping scales[59] (Fig. 5.1). Despite these rigid elements, the girdle is flexible enough to conform to rough surfaces[165,166], and as well as to locally wrinkle to form channels that allow water to circulate over the ctendia during respiration[67]. The degree of flexibility is remarkable considering the scales are composed of ~97% aragonite by weight[123], densely packed, and often overlap substantially[69,70,167,168]. To the best of my knowledge, the dorsal girdle scales of chitons are the most mineralized armor units of all known natural scale armors. The ganoid fish scales of Polypteriformes possess a thin outer layer of an enamel-like tissue called ganoine, which has a hydroxyapatite content of approximately 93% by weight[169]. However, the scales consist primarily of bone, which typically has a hydroxyapatite content of ~65% by weight[170].
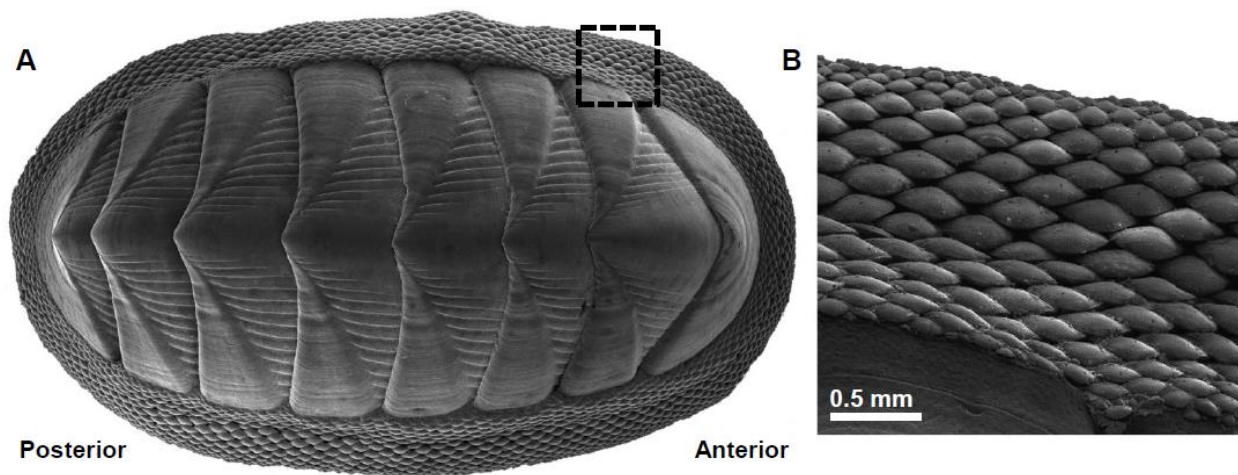
Figure 5-1 | Wide-field scanning electron microscopy image of the chiton *Rhyssoplax canariensis*. a, dorsal view of the shell plates and peripheral scale-covered girdle. **b,** enlargement of the region of the girdle enclosed with the dashed box in (**a**) highlighting the dorsal girdle scales.

The fine structural features (e.g. striations and bumps) of the dorsal surface of the scales are often used as a taxonomic aid. Consequently, hand-drawn illustrations[75,171,172], light micrographs[41], and SEM images[59] of the dorsal surface of the scales from a number of species are available. Less is known about the three-dimensional morphology of the scales. In a comprehensive study of the genus *Chiton*, R. Bullock provides scanning electron microscopy images of individual scales that have been removed from the girdle[71]. These images reveal that although the scales appear as overlapping discs from

above, the lower half of each scale is shaped like a rhombic prism. The transition from the prismatic base to the rounded overlapping upper region creates a "hook" shape.

The objectives of this study were 1) to quantify the 3D morphology of the dorsal girdle scales of chitons from a variety of species, 2) to investigate how the scales are embedded in the soft underlying tissue, and 3) to quantify the anisotropic flexibility of the girdle resulting from the geometry of the scales. To accomplish these goals, synchrotron X-ray micro-computed tomography was used to obtain the shape of dorsal girdle scales from five members each of the families Chitonidae and Ischnochitonidae. Scanning electron microscopy was used to study the fine structural features of the scales, and energy-dispersive X-ray spectroscopy was employed to determine the depth that the scales are embedded in girdle. Next, key structural features of the scale assemblies were combined in three-dimensional models of the scale armors. A multiple-material 3D printer was used to fabricate two-component prototypes of one model armor inspired by the scales of *Ischnochiton contratus* (Fig. 5-2). Finally, a bending test was developed to quantify the anisotropic stiffness of the scale armor prototypes.

Figure 5-2 | Light micrograph of the dorsal girdle scales of the chiton *Ischnochiton contractus*.

5.2 Materials and Methods

5.2.1 Sample Preparation

Entire dried shells of *Rhyssoplax canariensis* and *Chiton cumingsii* were purchased from Conchology, Inc. (Philippines). Girdles from *Rhyssoplax jugosa*, *Rhyssoplax tulipa*, *Radsia barnesii*, *Ischnochiton* (*Heterozona*) *fruticosus*, *Ischnochiton* (*Ischnoradsia*) *australis*, *Ischnochiton* (*Haloplax*) *lentiginosus*, and *Ischnochiton contractus* were separated from the plates and stored in a 70% ethanol solution until use. *Lepidozona mertensii* was also stored in a 70% ethanol solution, but was not previously disarticulated.

For synchrotron X-ray micro-computed tomography, rectangular girdle sections were prepared using a razor. Samples were gently rinsed with a 50% ethanol solution to

remove salt and detritus. For cross-sectional imaging and energy-dispersive X-ray spectroscopy, girdle samples of *R. canariensis* were embedded in a room temperature curing epoxy. After curing for ~24 hours, samples were sectioned with a diamond saw (IsoMet 5000, Buehler, Lake Bluff, IL), polished (Model 920, South Bay Technology, CA) stepwise with aluminum oxide pads (15 μm, 5 μm, and 3 μm), and then finely polished with 50 nm silica nanoparticles on cloth (MultiTex, South Bay Technology, CA).

5.2.2 Micro-Computed Tomography (μCT) & Morphometric Measurements

Girdle samples were scanned with an energy of 20.4-23.8 kV and a resolution of 2.84 μm/voxel at beamline 2-BM of the Advanced Photon Source at Argonne National Laboratory. Image processing software package Mimics (Version 15.0, Materialise, Belgium) was used for segmentation and construction of 3D triangulated surface meshes (binary STL format). The dorsal scales used in the morphometric study were selected from the middle (between the proximal and distal margins) of the girdles. The scales were segmented using a threshold brush technique which allows the user to highlight pixels over a specific grayscale range in an area defined by the brush location, size, and shape. Additional manual segmentation was limited to the removal of ring artifacts. To create scale armor models, the surface meshes of the scales were first reduced in file size as needed via the smooth, reduce, and remesh functions of 3-matic (Materialise, Belgium). Cross-sectional meshes were created using the cut function of the simulation module Mimics. Open source image analysis software ImageJ[157] was used to identify landmarks and make measurements from 2D cross-sectional images.

5.2.3 Light Microscopy

Micrographs of the dorsal girdle scales were captured with a Nikon ECLIPSE LV100 optical microscope (Tokyo, Japan). Polished cross-sectional samples were imaged with polarized light using a Nikon Eclipse L150 (Tokyo, Japan).

5.2.4 Scanning Electron Microscopy (SEM)

A Helios Nanolab 600 Dual Beam (FEI, OR) was used for SEM imaging at an accelerating voltage of 2-4 kV and a working distance of ~4 mm.

5.2.5 Energy-Dispersive X-ray Spectroscopy (EDX)

EDX was performed on polished cross sections with a Helios Nanolab 600 Dual Beam (FEI, OR) equipped with an INCA EDX system (Oxford Instruments) at an accelerating voltage of 20 kV.

5.2.6 Chiton Scale Armor Models

A 3D model of the scale armor of each species was created using 3D modeling software Rhinocerus (Robert McNeel & Associates). Each model consisted of two components, an array of scales and a flat underlying layer in which the scales were embedded. The arrays were created using the surface meshes of representative scales from each species, which we obtained directly from synchrotron micro-computed tomography. Each representative scale was replicated on a diamond-shaped grid, creating an array of identical scales that mimicked the physiological scale arrangement (Fig. 5-15). In each model, the scales were packed as densely as possible by minimizing the inter-scale spacing distance, s (Fig. 5-14).

5.2.7 Multi-Material 3D Printing of Scale Armor Prototypes

Scale armor prototypes inspired by *I. contractus* were fabricated using an OBJET Connex500 3D Printer (Stratasys, Minnesota, USA). The STL files for each of the two components, the scales and the substrate, were imported into the OBJET Studio software and assigned a material. The scales were printed with a rigid polymer called VerroWhite, while the substrate was printed with a compliant rubber-like polymer called TangoPlus. VerroWhite and TangoPlus have elastic moduli of 2.02 GPa and 0.7 MPa, respectively[173]. Bending tests were designed with pin boundary conditions, so each prototype was printed with VerroWhite pins attached to either side (Fig. 5-16a). Each prototype had a span and width of 135 mm and 63 mm, respectively. The embedded height of the scales, h_1, which was also the thickness of the TangoPlus substrate, was 4.1 mm (Fig 5-16d). The individual scale width, W, and inter-scale spacing distance, s, of the prototypes were 10 mm and 0.5 mm, respectively. The prototypes were scaled-up ~30× relative to the actual girdle of *I. contractus*.

5.2.8 Bending Tests of Scale Armor Prototypes

Bending tests were conducted with a Zwick Z2.5 (Zwick/Roell, Germany). The prototypes were initially compressed with the loading axis approximately parallel to their span. A buckling transition from compression to bending was observed at the start of every test. The dorsal surface of the scales was on the concave side of each prototype during testing. The tests were performed with pin boundary conditions under displacement control with a rate of 0.5 mm/s. Side profile images of the tests were taken at rate of 0.5 fps (VicSnap, Correlated Solutions). Force (F) vs. displacement (d) data was collected from each test.

5.3 Results

5.3.1 Fine Structural Features of the Scale Armor

Rhyssoplax canariensis (Fig. 5-1 and Fig. 5-3a) was chosen as a model system to investigate the fine structure and composition of the scale armor of chitons. As shown in Fig. 5-3c and d, the scale armor of chitons consists of three layers: dorsal scales, the soft tissue of the girdle, and ventral scales. From the proximal to the distal margins, the dorsal scales decrease in size and the girdle decreases in thickness (Fig. 5-3c). Each dorsal scale hooks dorsally, overlapping its proximal neighbor. The gaps between neighboring scales can clearly be seen in cross sections, but are not visible dorsally (Fig. 5-1 and Fig. 3b). In girdles that had be stored in a 70% ethanol solution, the soft tissue of the girdle was able to be removed without destroying the integrity of the assembly of dorsal girdle scales (Fig. 5-4). Organic material appeared to be present between the scales, which were still robustly connected even though they had been removed from the substrate.
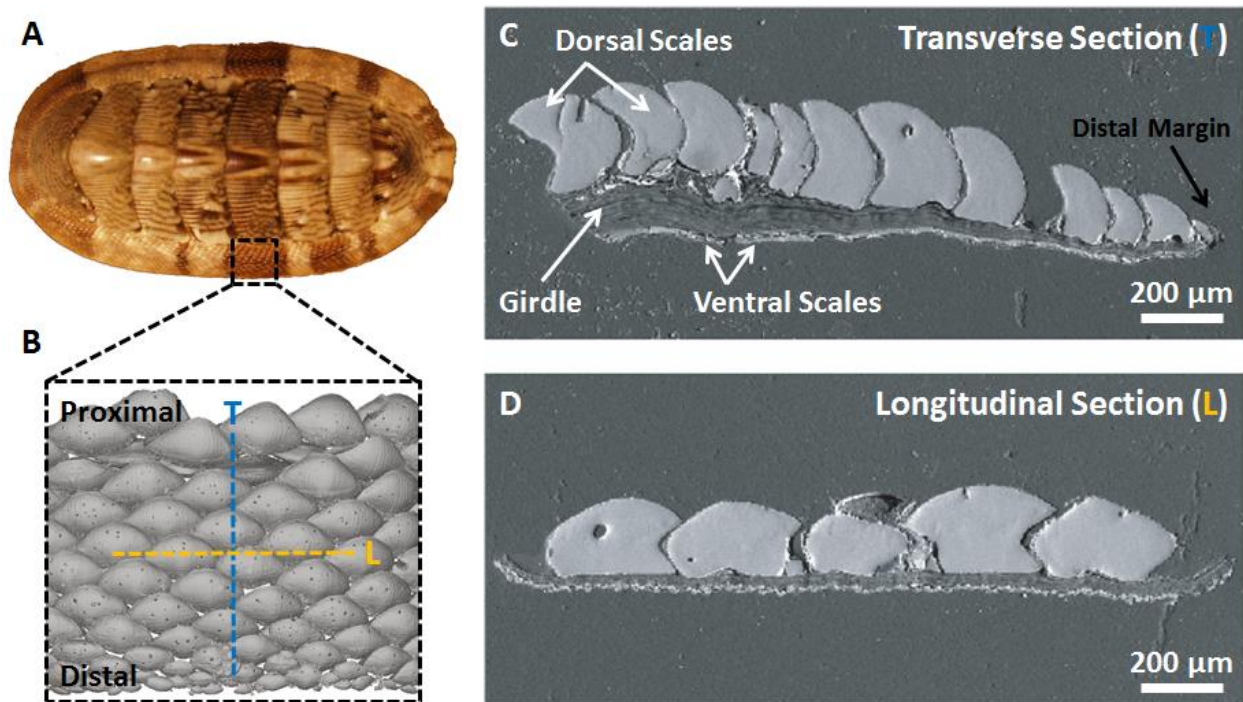
Figure 5-3 | Cross-sectional structure of the scale armor of *Rhyssoplax canariensis*. a, Light micrograph of the dorsal side of a dried shell of *R. canariensis*. The scale-covered girdle surrounds the eight central plates. **b,** Synchrotron μCT reconstruction of the dorsal girdle scales. Note that the scales hook towards the body of the chiton. **c** and **d,** SEM images of polished transverse and longitudinal, respectively, cross sections of the girdle.
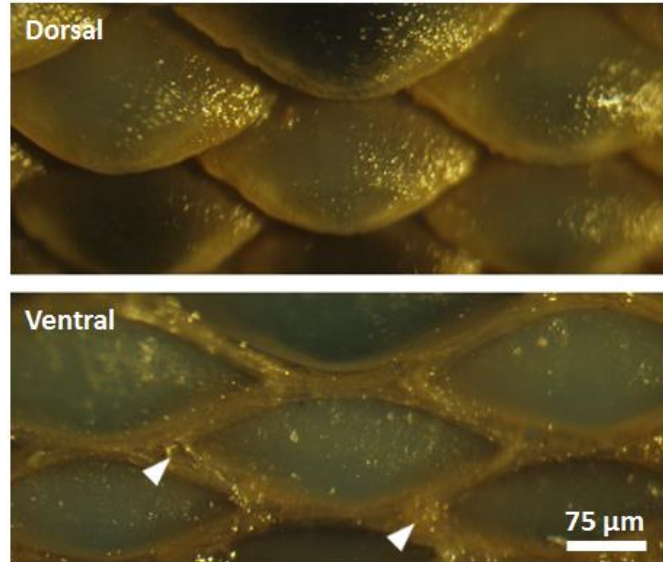
Figure 5-4 | Light micrographs of the dorsal girdle scales of *Chiton* **sp. after removing the underlying soft tissue of the girdle**. Note that in the ventral image, organic material (indicated by white triangles) is present between the scales, robustly connecting them together.

To determine if organic material is present between the dorsal scales, we used energy-dispersive X-ray spectroscopy (EDX). EDX revealed that nitrogen was present underneath and between the scales, but not in the surrounding epoxy (Fig. 5-5, top right, "N" map). This confirmed the presence of a nitrogen-containing organic material between the scales. EDX also indicated that the organic matter of the girdle and inter-scale material is not calcified, as evident by the absence of calcium in these regions (Fig. 5-5, top right, "Ca" map). SEM images of fractured pieces of the girdle showed that the inter-scale material extends from the base of each scale to the height at which the overlapping dorsal hook begins to form (Fig. 5-6a). We later refer to this height as h_1.

Closely examining the girdle via SEM showed that it is composed of layers of fibers (Fig. 5-5 and Fig. 5-6b). High resolution SEM revealed that some of the fibers are striated (Fig. 5-5, bottom right), suggesting the presence of collagen. In comparison to the dorsal scales, the ventral scales are roughly an order of magnitude smaller. They are cylindrically shaped, with a diameter of ~20 μm (Fig. 5-6c).
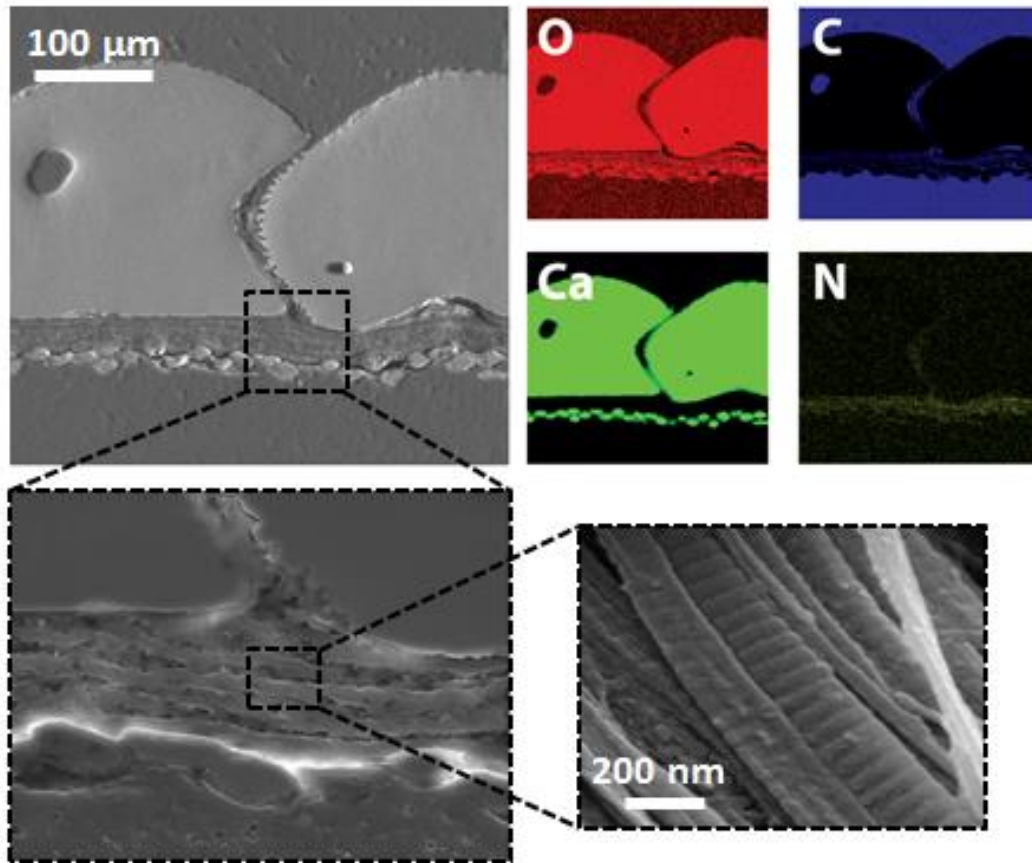
Figure 5-5| Energy-dispersive X-ray spectroscopy maps and high resolution SEM images of the scale armor of the chiton *Rhyssoplax canariensis*. **top left**, SEM image of a polished longitudinal cross section showing the dorsal scales, girdle, and ventral scales. **bottom left**, Enlargement of the region enclosed by the dashed box in the top left image. The layers of the girdle are clearly visible. **bottom right**, high resolution SEM image of individual fibers from the girdles showing their striated structure. **top right**, Oxygen, carbon, calcium, and nitrogen EDX maps of the top left image. Note that nitrogen is present between the scales and in the girdle, but not in the surrounding epoxy.
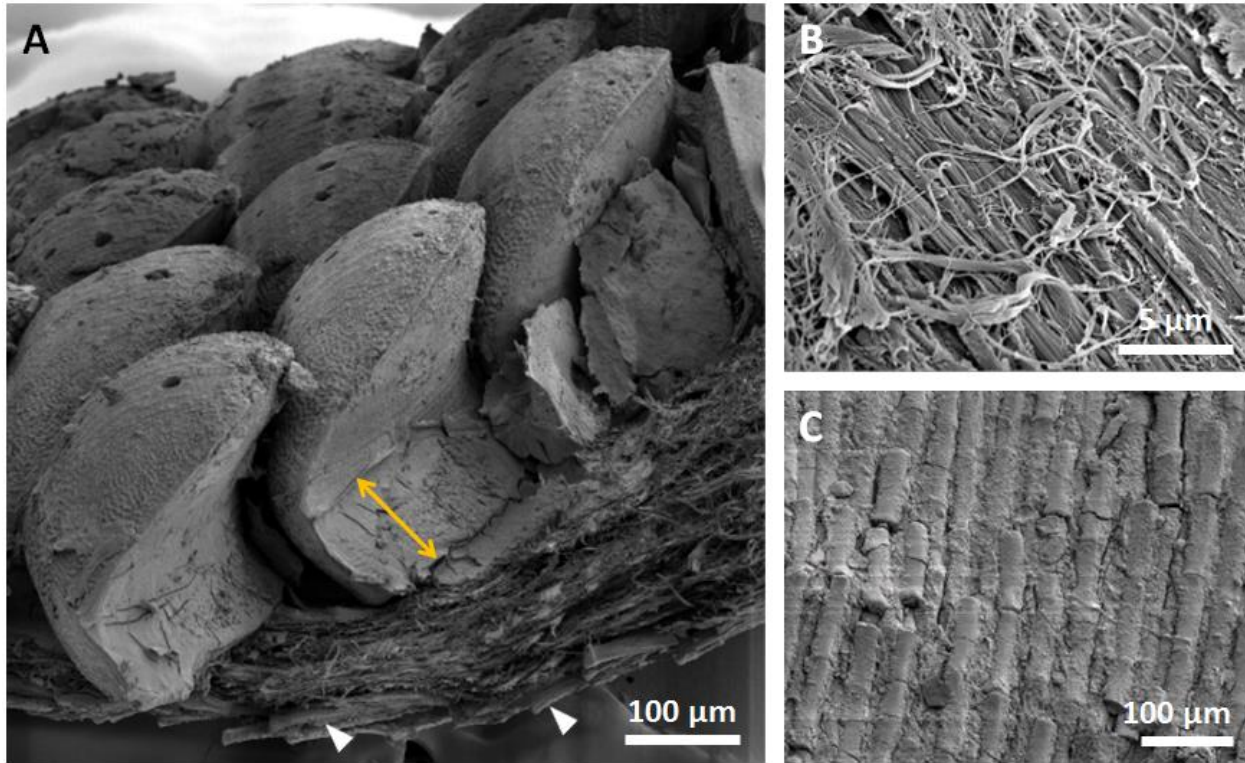
Figure 5-6| SEM images of the scale armor of the chiton *Rhyssoplax canariensis*. **a**, Fractured cross section of the armor. The orange line indicates the height of the inter-scale organic material. White arrows point to the ventral scales. **b**, The fibrous structure of the organic material of the girdle. **c**, The small cylindrically shaped ventral scales.

Light microscopy of a polished transverse cross section of the scale armor indicated that a triangular suture interface is present between the posterior surface of each dorsal girdle scale and the inter-scale organic material (Fig. 5-7a). SEM showed that the triangular suture has a height and wavelength of ~5 μm (Fig. 5-7b). To further examine the interface, individual scales were removed from the girdle (Fig. 5-8a). As shown in Fig. 5-8b, the cross-sectional triangular suture interface results from conical bumps which cover the posterior surface of each dorsal scale. R. Bullock denotes similar features observed in the genus *Chiton* as "sculpture of the ventro-lateral area"[71].
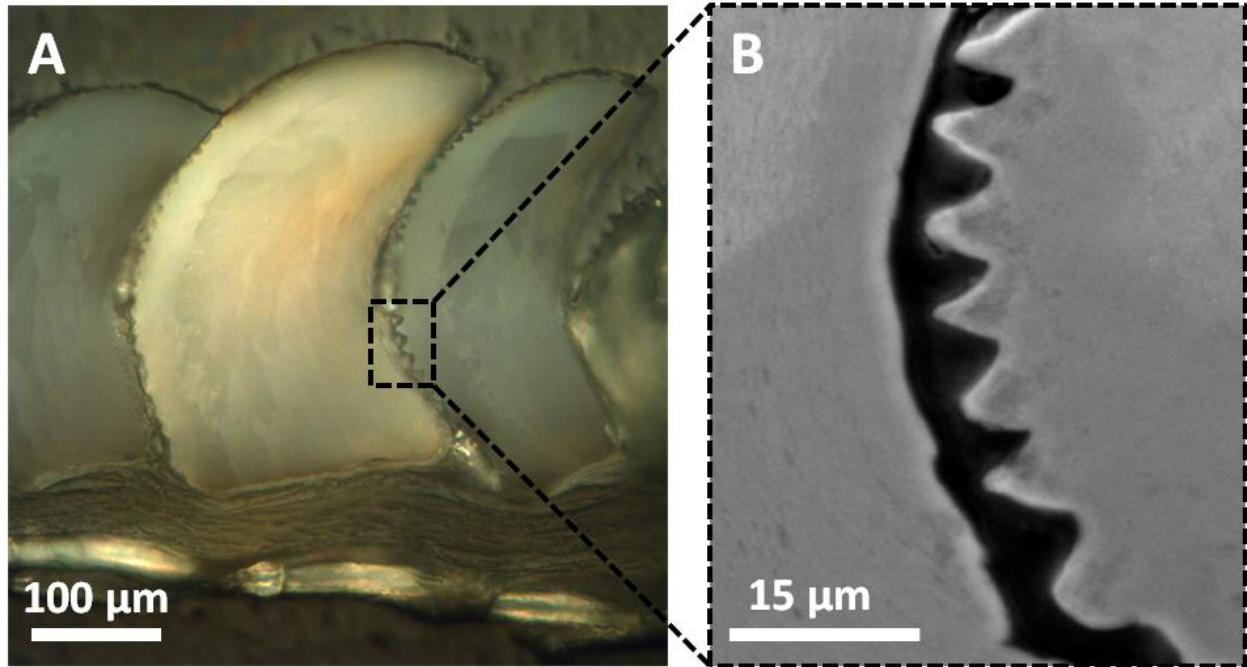
Figure 5-7 | The triangular suture interface between the posterior surface of each dorsal scale and the inter-scale organic material. **a**, Polarized light micrograph of a polished transverse cross-section of the girdle. **b**, SEM image of the triangular suture interface.
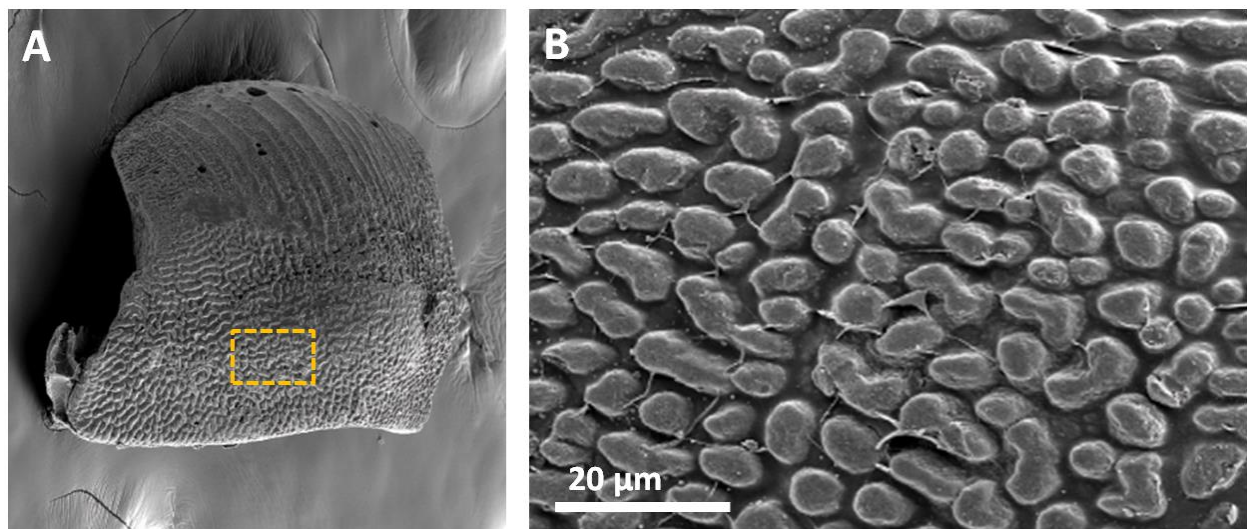
Figure 5-8 | The posterior surface of dorsal girdle scales. **a**, SEM image of the posterior surface of a scale. **b**, enlargement of the region enclosed with the orange box in (**a**). The cross-sectional triangular suture interface seen in Fig. 5-7b corresponds to the conical surface bumps seen in (**b**).

5.3.2 Comparative Morphology of Chiton Dorsal Girdle Scales

Synchrotron X-ray micro-computed tomography was used to investigate the three-dimensional shape of dorsal girdles scales from ten species of chitons. Girdle samples for μCT were generally a few millimeters in length and width, and included scales at the proximal and distal margins. The highly X-ray absorbent mineralized scales were easily segmented from the non-mineralized substrate and inter-scale materials. 3D μCT reconstructions of the scale assemblies revealed the diamond mosaic patterns of their ventral surfaces, which have not been previously observed with light microscopy or SEM (Fig. 5-9). The scales of *R. canariensis* are tightly packed despite a clear gradient in scale size (Fig. 5-9, top right).

Next, we segmented individual scales from each sample. Fig. 5-10 displays representative dorsal girdle scales from ten species of chitons. The scales ranged in volume from approximately 0.1 mm³ (*R. tulipa*) to 0.005 mm³ (*L. mertensii*). To compare the morphology of scales from different species, morphometric dimensions were established (Fig. 5-11 and Table 5-1).
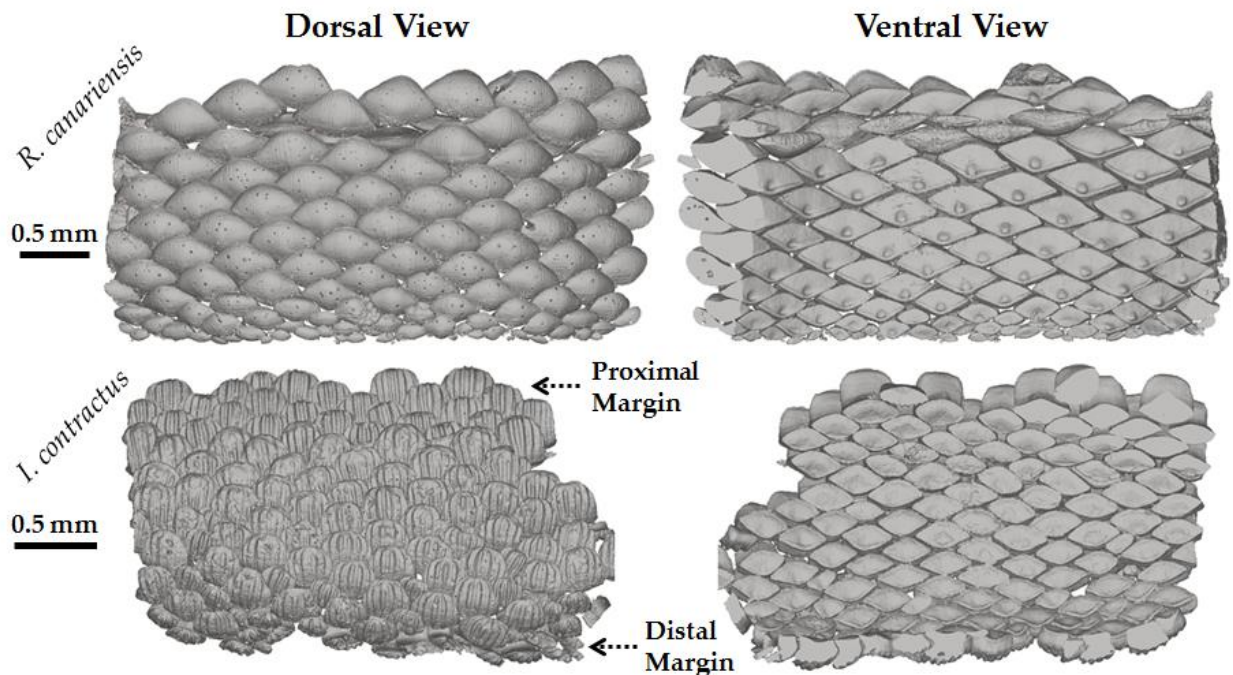
Figure 5-9| Micro-computed tomography reconstructions of the scale assemblies of the chitons *Rhyssoplax canariensis* and *Ischnochiton contractus*. The dorsal scales appear as overlapping discs from above and as a diamond mosaic from below.
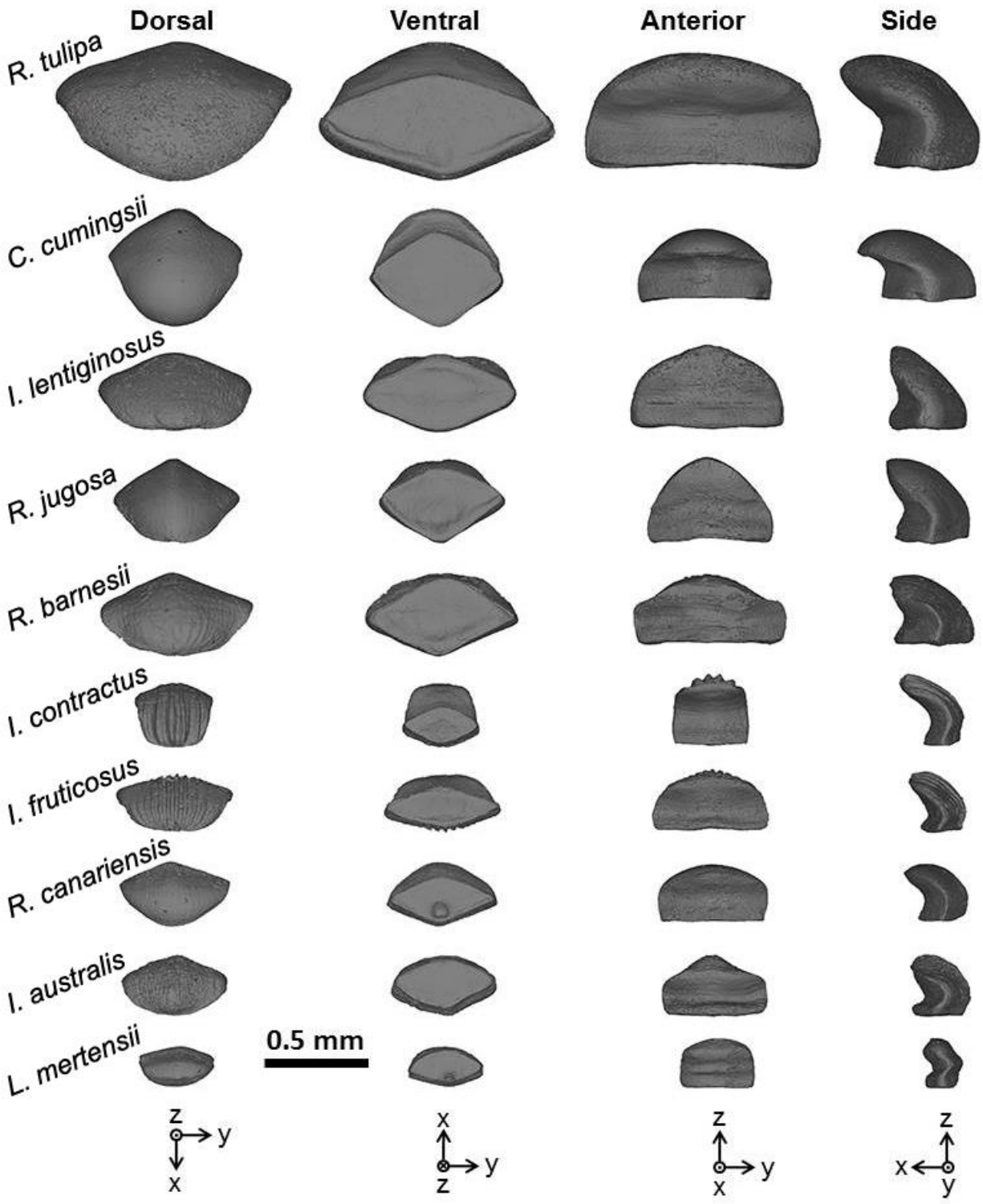
Figure 5-10| Micro-computed tomography reconstructions of individual dorsal girdle scales from ten species of chitons.
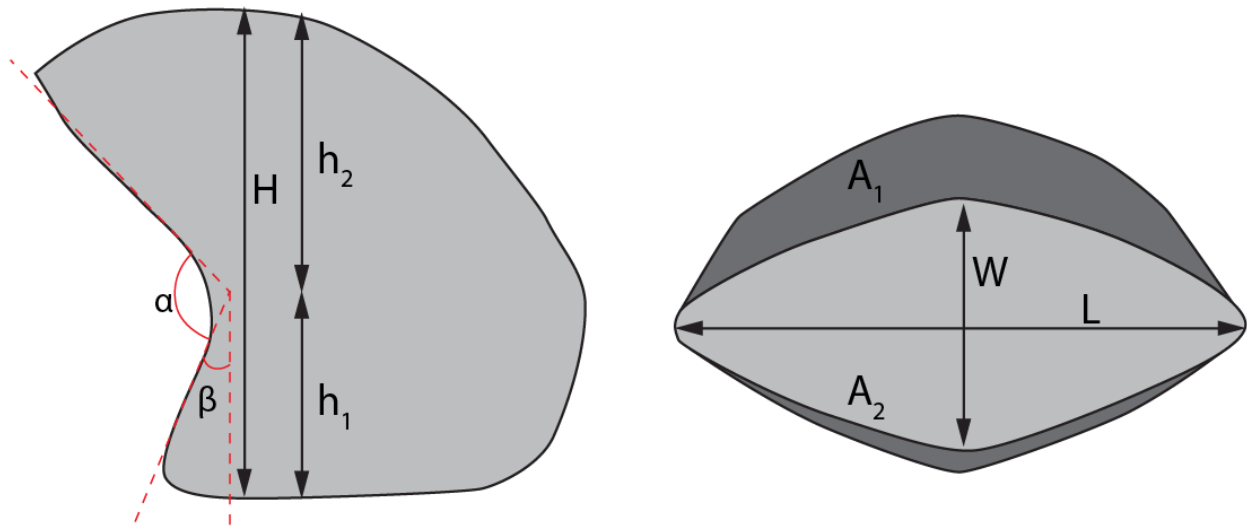
Figure 5-11| Schematic diagrams illustrating the morphometric dimensions of individual scales. **left**, cross-sectional (along the transverse bisector) side view. **right**, ventral view. Descriptions of the symbols can be found in Table 5-1.

Dimension	Description
H	height; $H = h_1 + h_2$
h_1	height of the base
h_2	height of the upper region
W	width of the base
L	length of the base
α	imbrication angle; h_1 and h_2 are separated by the vertex of α
β	inclination angle
A_{total}	total projected area of the scale when viewed ventrally
A_1	$A_1 = A_{total} - A_2$
A_2	area of the base

Table 5-1| Descriptions of the morphometric dimensions of individual scales.
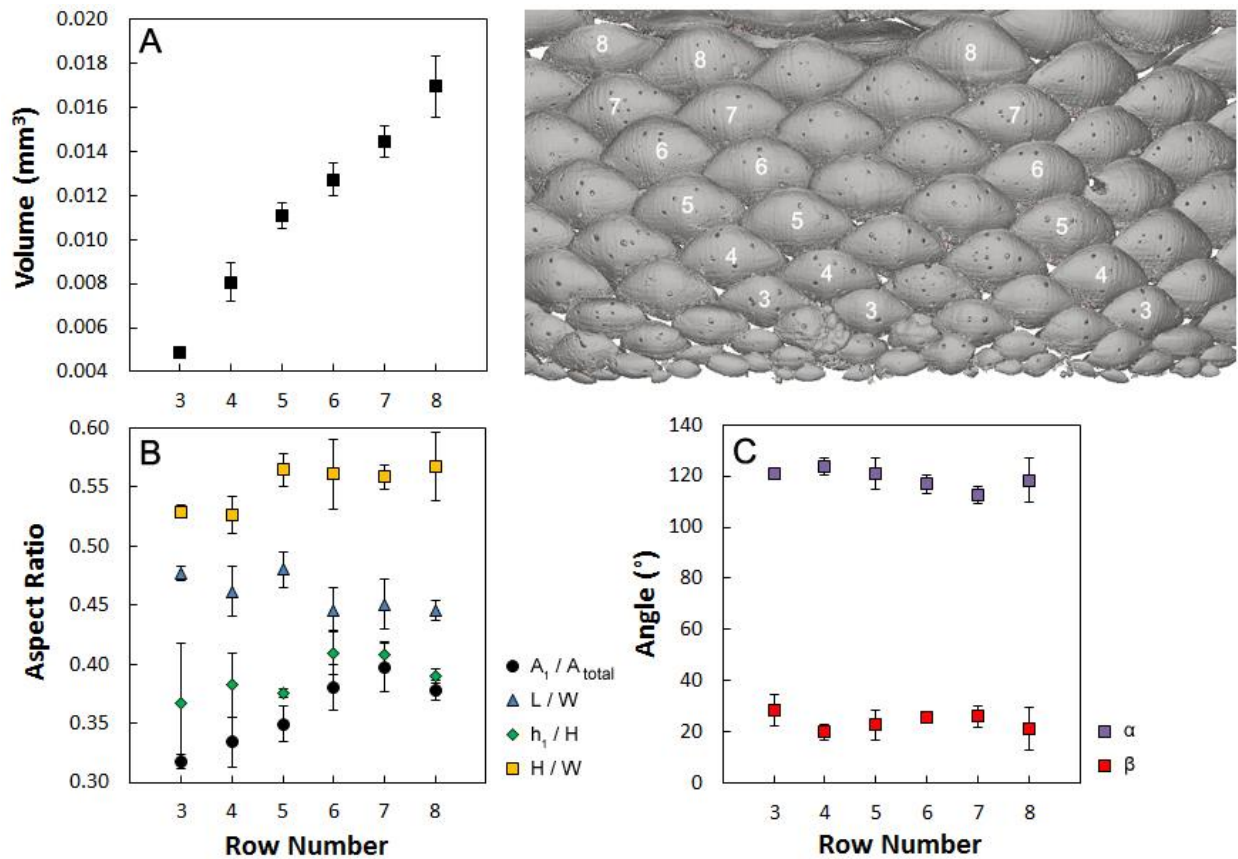
Figure 5-12│ Morphometric measurements of the dorsal girdle scales of the chiton *Rhyssoplax canariensis*. Each data point and error bar represents the average and standard deviation, respectively, of measurements from three scales of one row. **upper right**, Dorsal view of a synchrotron μCT reconstruction of the dorsal scales of *R. canariensis*. The scales used in the morphometric study are labeled according to their row. **a**, Volume vs. row number. **b**, Various dimensionless aspect ratios vs. row number. **c**, Angles α and β vs. row number.

The scales of some species proximally increase in size (e.g. *R. canariensis*, Fig. 5-9, top). Therefore, I checked whether or not scales of different sizes from one species were geometrically similar using *R. canariensis* as a model system (Fig. 5-12). Three scales were segmented from each row 3-8 (Fig. 5-12, upper right), and their morphometric dimensions were measured. Although the average scale volume decreases by ~70% from row 8 to row 3 (Fig. 5-12a), most of the aspect ratios and angles did not significantly change relative to standard deviations of the measurements (Fig. 5-12b and c). The exception was the ratio A_1/A_{total}, which linearly increased by 25% from row 3 to row 7 (Fig. 5-12b).

Species	Volume (mm³)	A_1 (mm²)	A_{total} (mm²)	L (μm)	W (μm)	h_1 (μm)	H (μm)	α (°)	β (°)
I. fruticosus	0.014 ± 0.002	0.038 ± 0.003	0.098 ± 0.004	179 ± 15	486 ± 18	77 ± 10	275 ± 19	114 ± 13	39 ± 9
I. australis	0.013 ± 0.001	0.027 ± 0.003	0.087 ± 0.007	215 ± 20	421 ± 21	76 ± 4	264 ± 14	91 ± 6	58 ± 5
I. lentiginosus	0.038 ± 0.002	0.020 ± 0.006	0.183 ± 0.011	330 ± 9	695 ± 13	126 ± 11	363 ± 15	128 ± 9	34 ± 7
I. contractus	0.0085 ± 0.0008	0.043 ± 0.002	0.076 ± 0.005	148 ± 10	312 ± 24	126 ± 6	253 ± 19	110 ± 6	21 ± 5
L. mertensii	0.0060 ± 0.0008	0.013 ± 0.002	0.045 ± 0.005	143 ± 6	304 ± 23	85 ± 12	221 ± 12	87 ± 6	51 ± 6
R. jugosa	0.029 ± 0.002	0.033 ± 0.007	0.140 ± 0.007	315 ± 15	526 ± 17	138 ± 6	359 ± 20	124 ± 5	24 ± 4
R. tulipa	0.11 ± 0.02	0.130 ± 0.03	0.387 ± 0.045	429 ± 28	931 ± 54	189 ± 5	448 ± 46	120 ± 4	15 ± 3
R. canariensis	0.013 ± 0.001	0.036 ± 0.004	0.092 ± 0.005	196 ± 6	434 ± 19	102 ± 8	248 ± 9	112 ± 4	22 ± 2
C. cumingsii	0.046 ± 0.006	0.065 ± 0.008	0.240 ± 0.029	433 ± 9	592 ± 46	151 ± 10	320 ± 9	108 ± 6	12 ± 2
R. barnesii	0.029 ± 0.005	0.029 ± 0.01	0.167 ± 0.023	335 ± 18	641 ± 49	109 ± 11	299 ± 17	116 ± 5	37 ± 5

Table 5-2| Morphometric measurements of the dorsal girdle scales of ten species of chitons. Values indicate the averages and standard deviations of measurements from 5 scales. The morphometric symbols are illustrated in Fig. 5-11 and described in Table 5-1.
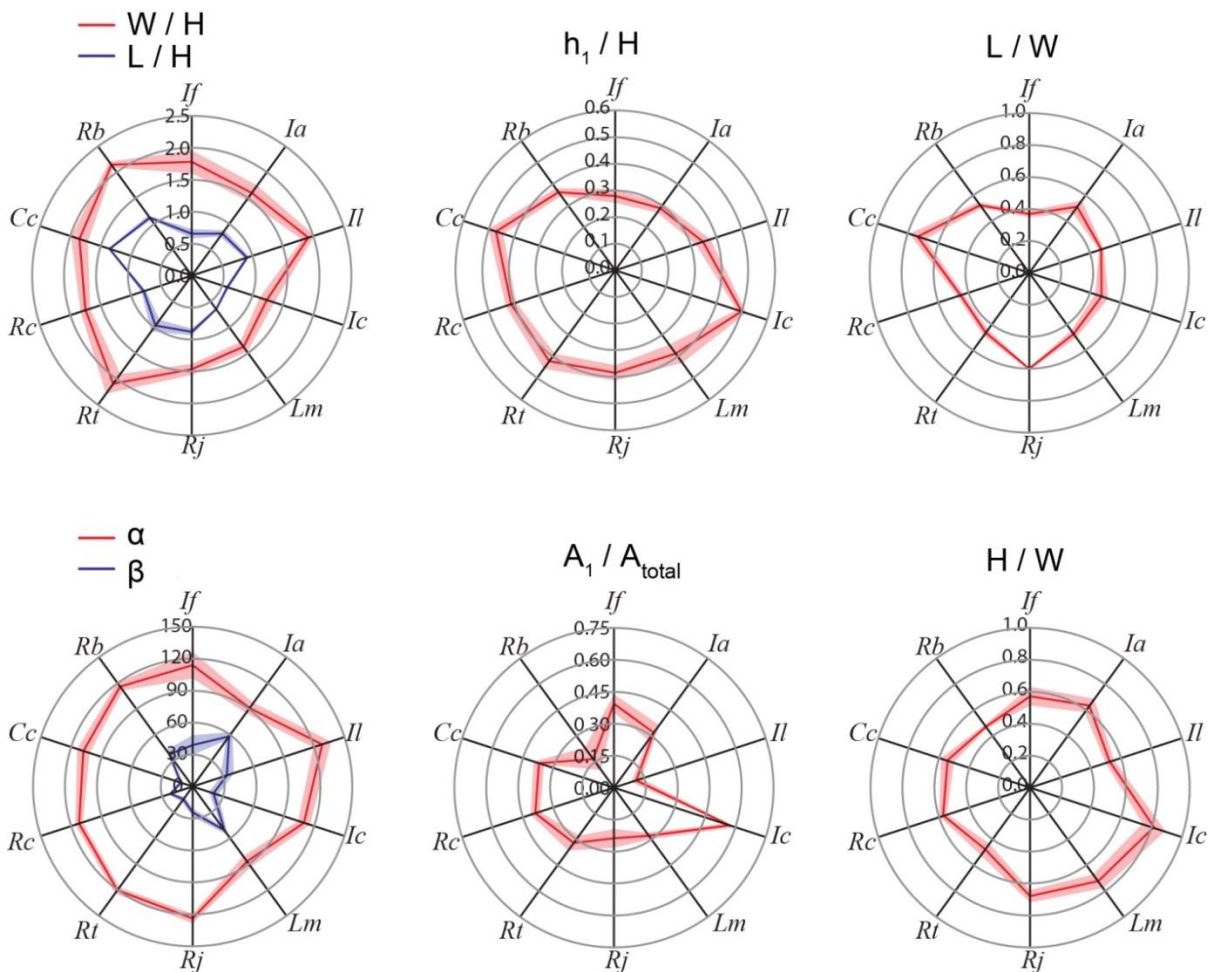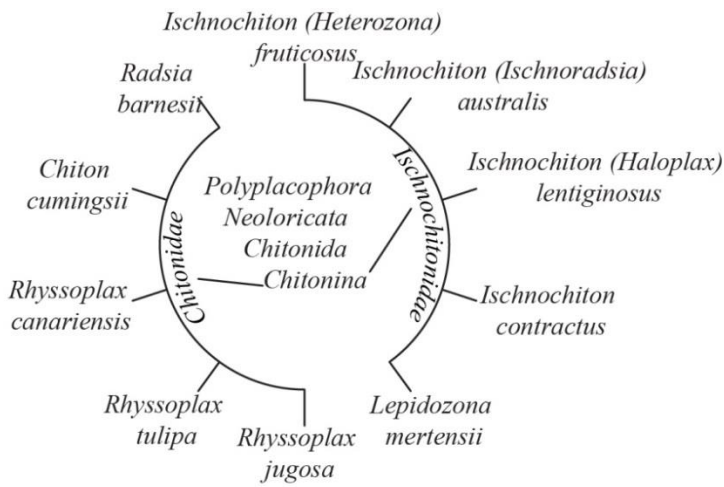
Figure 5-13 | Comparative morphology of the dorsal girdle scales of ten species. The thin dark red and blue lines represent the average measurements from five scales. The thicker light red and blue lines, which encompass the thin lines, represent the standard deviations of the measurements. The morphometric symbols are illustrated in Fig. 5-11 and described in Table 5-1.

Next, five scales were segmented from the μCT data of each of the ten species seen in Fig. 5-10, and their morphometric dimensions were measured (Table 5-2). The scales were selected from middle area of the girdles (approximately equidistant from the proximal and distal margins). Selected angles and aspect ratios are compared in the polar plots of Fig. 5-13. In most species, the prismatic base of the dorsal scales accounts for ~30-40% of their height (in other words, h_1/H ranges from ~0.3-0.4). However, the prismatic base is ~50% of the total height in *C. cumingsii* and *I. contractus*. The imbrication angle, α, ranges from ~90° in *I. australis* and *L. mertensii* to ~130° in *I. lentiginosus*. As illustrated in Fig. 5-13, the inclination angle, β, is much larger in Ischnochitonidae than in Chitonidae. β ranges from ~60° in *I. australis* to ~10° in *C. cumingsii*. In all species, the sum of the imbrication and inclination angles is less than 180°. The *W/H*, *L/H*, and *L/W* aspect ratios of the scales range from ~1.25-2, ~0.5-1.25, and ~0.45-0.75, respectively.

5.3.3 Chiton Scale Armor Models

To create models of the scale armors, the 3D surface meshes (obtained via μCT) of one representative scale from each of the ten species were arranged in a rectangular grid (Fig. 5-14a). Thus, each scale armor model is an array of identical scales (Fig. 5-15) The inter-scale spacing distance, *s*, was minimized to maximize scale overlap (Fig. 5-14b). We define *s* such that it is orthogonal to the sides of the diamond-shaped base of the scales. The minimum *s/W* ratios geometrically permitted by the shape of the scales ranged from 0.01 (*I. lentiginosus* and *R. jugosa*) to 0.08 (*R. canariensis*). Note that W is the scale width (Fig. 15-14b), not the width of the entire model.

A

s

W
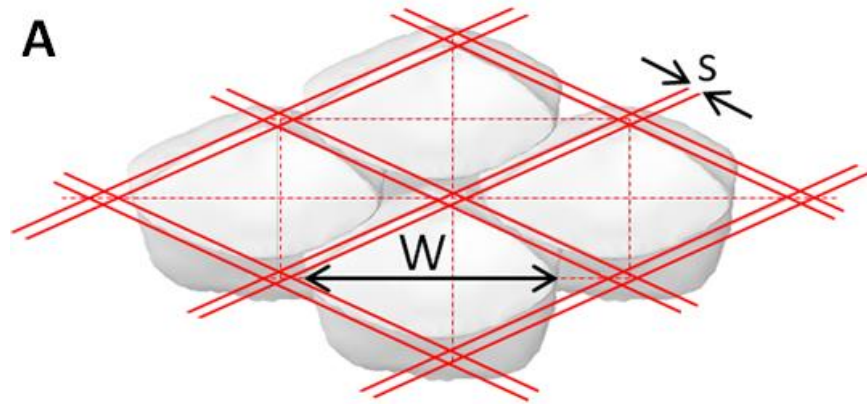
B

Species	$(s/W)_{Minimum}$
I. fruticosus	0.05
I. australis	0.07
I. lentiginosus	0.01
I. contractus	0.05
L. mertensii	0.07
R. jugosa	0.01
R. tulipa	0.07
R. canariensis	0.08
C. cumingsii	0.04
R. barnesii	0.05

Figure 5-14| The assembly grid and inter-scale spacing distance of chiton scale armor models. **a**, Ventral view of a 2 × 2 scale armor model of *I. contractus*. The dotted red lines indicate the rectangular assembly grid. **b**, Table displaying the minimum *s/W* aspect ratios geometrically permitted in the models. Definitions: *s*, inter-scale spacing distance; W, scale width.
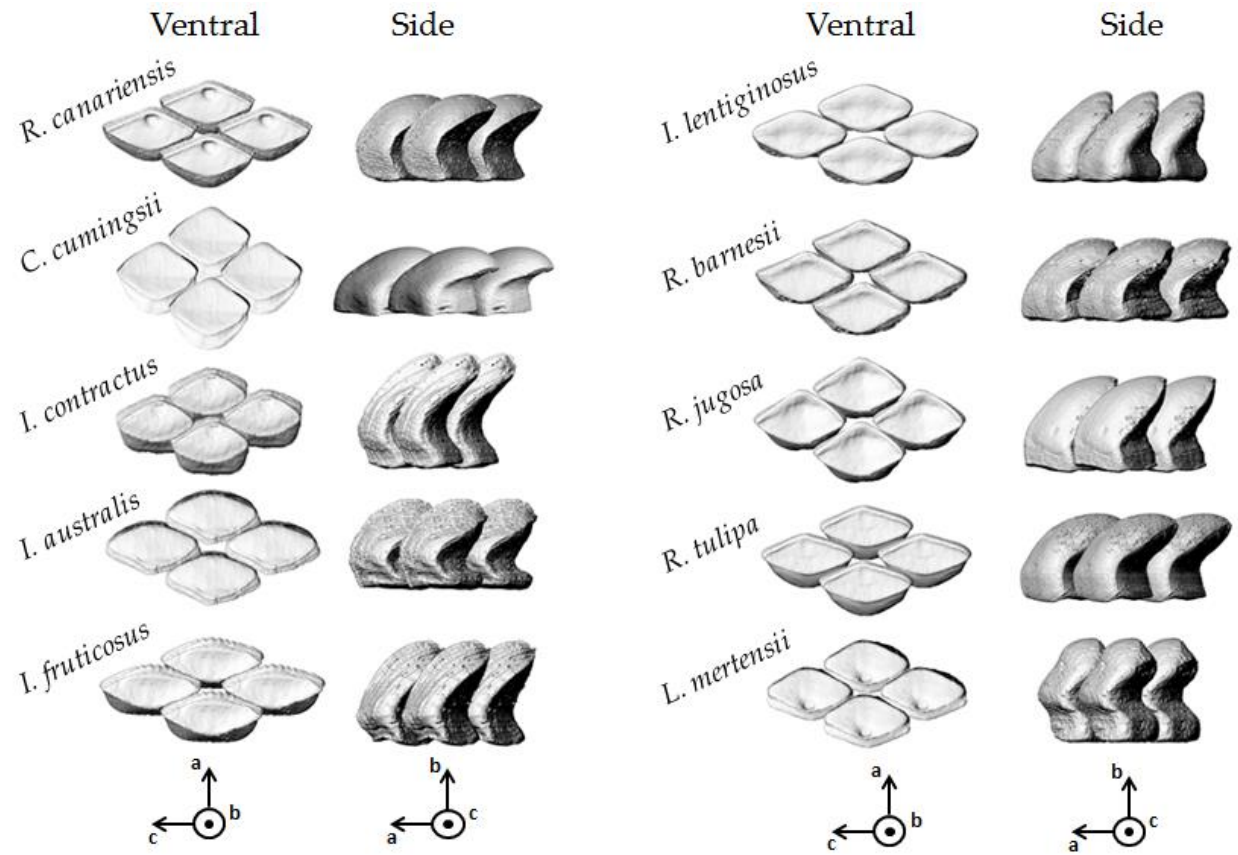
Figure 5-15 | 2 × 2 chiton scale armor models. The arrays were created using the surfaces meshes of one representative scale from each species. Each representative scale was replicated on a diamond-shaped grid, creating an array of identical scales.

5.3.4 Bending Tests of Chiton Scale Armor Prototypes

To determine the anisotropic flexibility of chiton scale armor, a bending test was developed (see section 5.2.8 of Materials and Methods). *I. contractus* was chosen as a model system because its scales had the largest A_1/A_{total} ratio, which suggested a high degree of imbrication. Multi-material 3D printing was used to fabricate prototypes for bending tests (see section 5.2.7 of Materials and Methods). The bending tests were conducted with pin boundary conditions, so each prototype was printed with rigid pins attached to either side (Fig. 5-16a). As shown in Fig. 5-16b, the prototypes consisted of two components: rigid overlapping scales (E = 2.02 GPa) and a compliant substrate (E = 0.7 Mpa). The scales had a width, *W*, of 10 mm, a spacing distance, *s*, of 0.5 mm, and an embedded height, h_1, of 4.1 mm (Fig. 5-16d). Two prototypes were printed. One had a scale orientation angle, ϕ, of 0°, while the other had ϕ = 90°. I define ϕ as the angle between the initial loading axis of the prototype and the overlapping ("hook") direction of the scales (Fig. 5-17). A transparency effect was used to quantify the imbrication of the scales in 3D models of the prototypes (Fig. 5-18a and b). When viewed dorsally, the ratio of the projected area of the overlapping regions to total area was ~40% (Fig. 5-18c and d).

Force-displacement curves from the bending tests of the prototypes with ϕ = 0° and 90° are displayed in the top left region of Fig. 5-19. The tests of both prototypes had an initial linear region. In these regions, the stiffness of the prototype with ϕ = 90°, 0.54 N/mm, was approximately an order of magnitude larger than that of the prototype with ϕ = 0°, 0.059 N/mm. In the test of the prototype with ϕ = 90°, the mechanical response of the prototype changed significantly around a displacement of 20 mm. Post-test images indicate that there was considerable interface failure (Fig. 5-19, top right), although no single crack extended through the entire width of the sample. In contrast, no plastic deformation could be detected in the prototype with ϕ = 0° after testing.
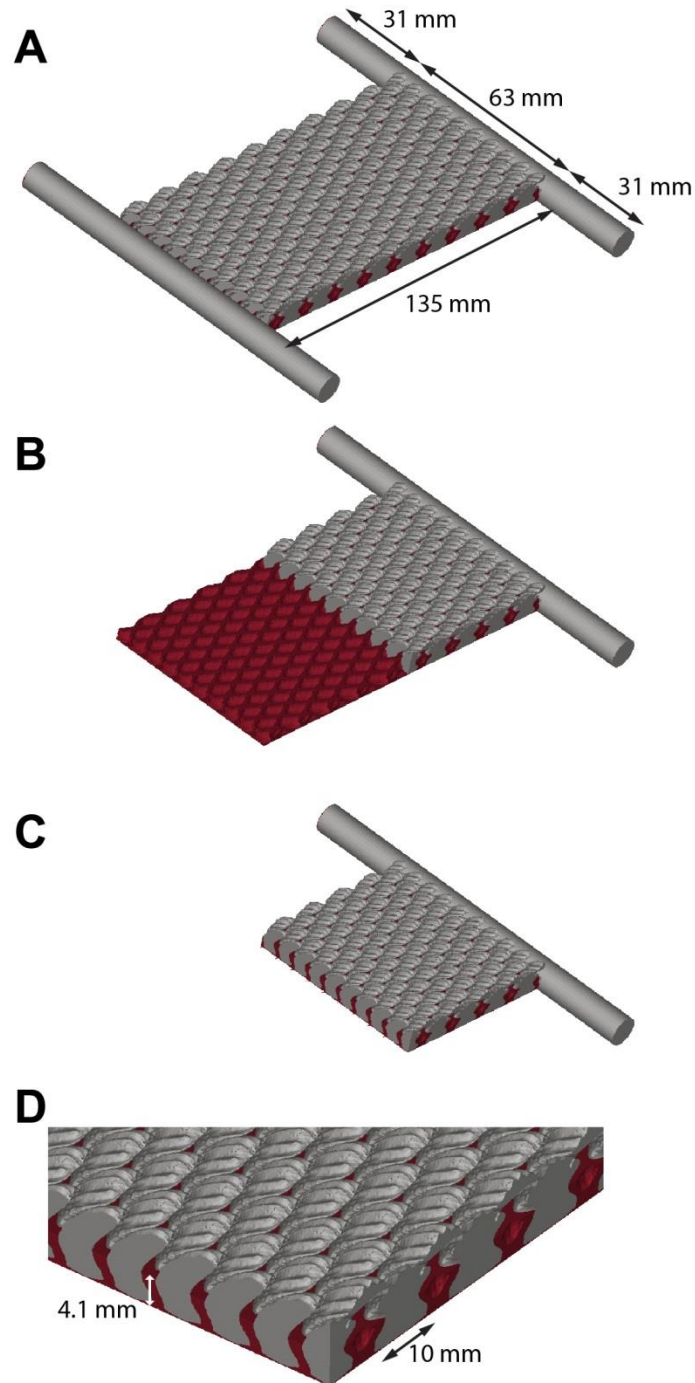
Figure 5-16| Chiton scale armor prototype designed for bending tests. The prototype has two components: rigid scales (grey, printed with VerroWhite, E = 2.02 GPa) and a compliant substrate (red, printed with TangoPlus, E = 0.7 MPa). This prototype corresponds to the right image of Fig. 5-17, in which ϕ = 90°. **a**, Illustration of the dimensions of the prototype. The pins (printed with VerroWhite, diameter = 10 mm) extend 31 mm to each side. **b**, Section of the prototype highlighting the cellular shape of the substrate. **c**, cross section of the prototype. **d**, enlargement of the edge of (**c**) showing the embedded height of the scales (h_1 = 4.1 mm) and the width of each scale (W = 10 mm).
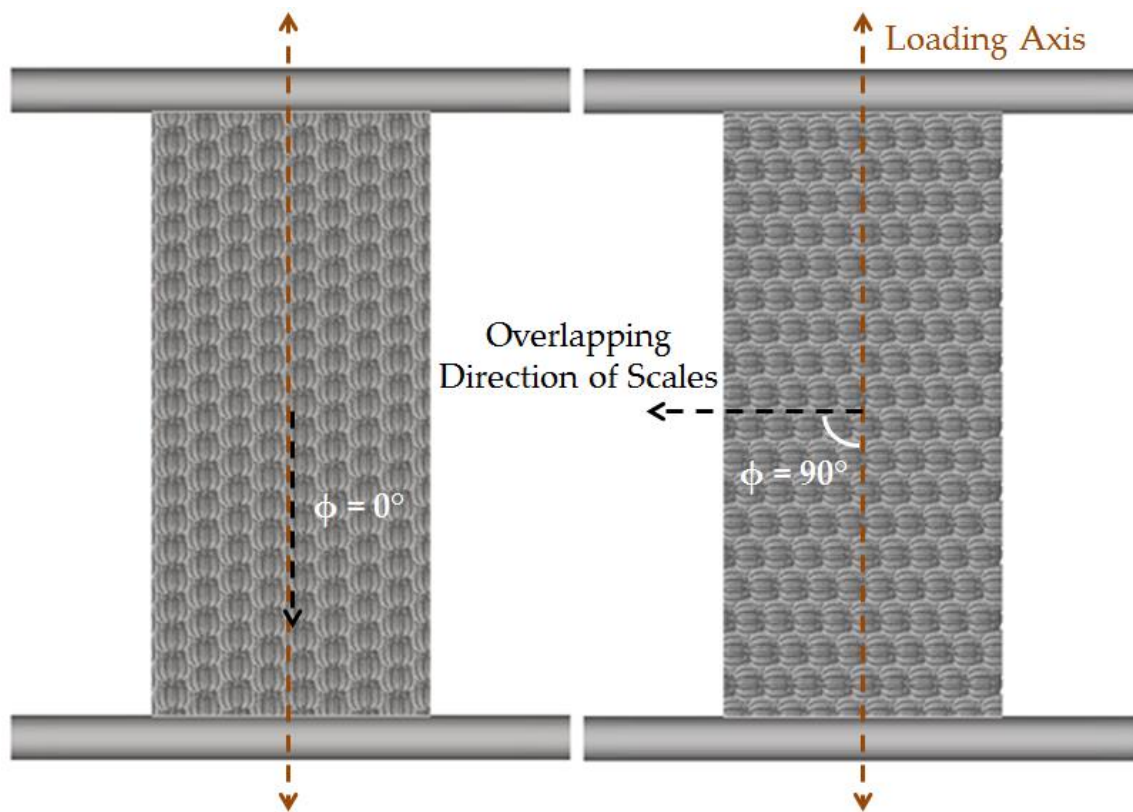
Figure 5-17| Dorsal view of two scale armor prototypes with φ = 0° and φ = 90°. φ is the angle between the loading axis of the bending tests and the overlapping ("hook") direction of the scales.
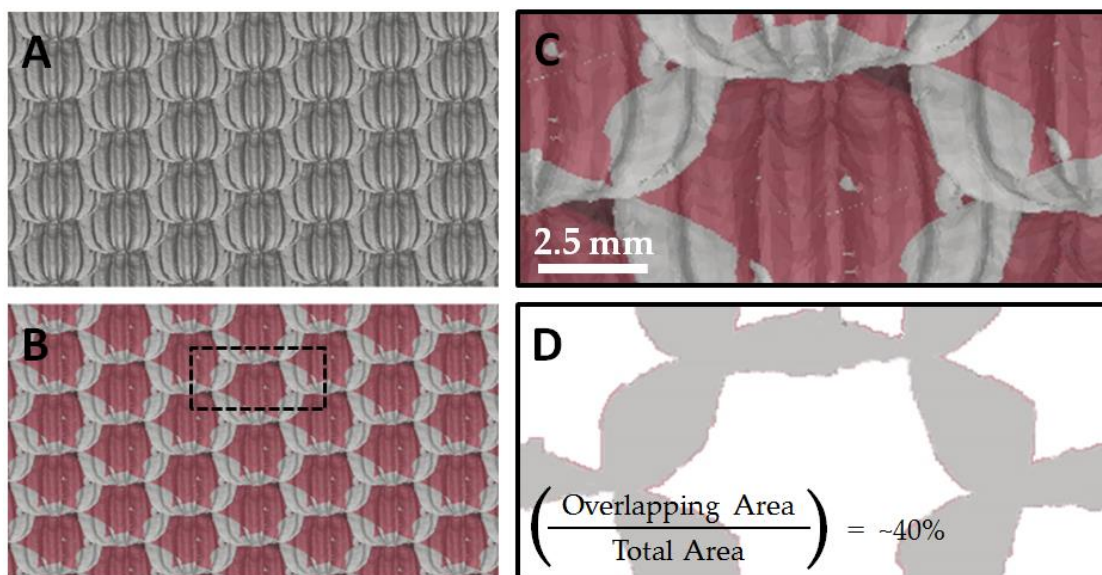
Figure 5-18| Imbrication of the scales of the prototypes. **a**, dorsal view of the overlapping scales of the prototypes. **b**, transparent image corresponding to (**a**) highlighting the overlapping regions (grey) and the non-overlapping regions (red). **c**, Enlargement of the area enclosed with the dashed black box in (**b**). **d**, Binary representation of (**c**). The overlapping and non-overlapping regions of (**d**) are grey and white, respectively.
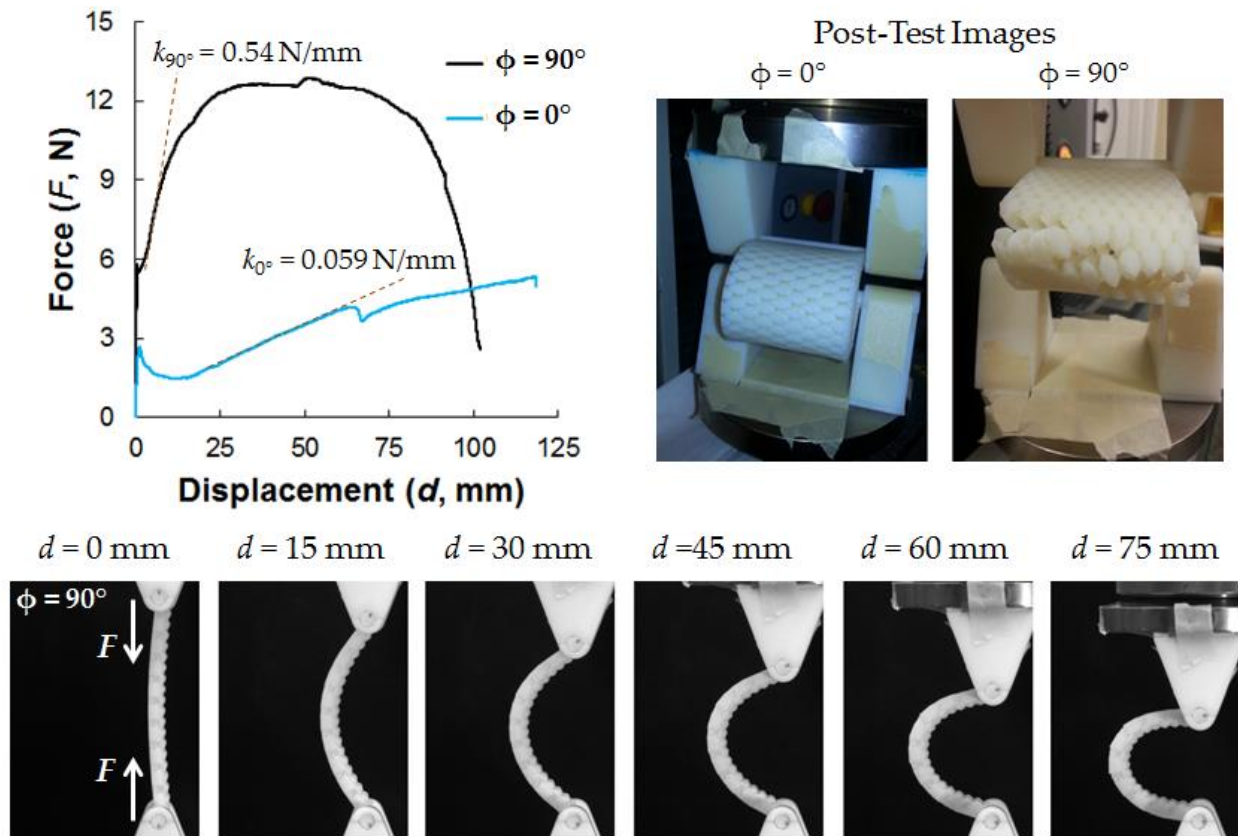
Figure 5-19 | Bending tests of scale armor prototypes inspired by the chiton *Ischnochiton contractus*. top left, Force-displacement curves for two prototypes with $\phi = 0°$ (blue) and $\phi = 90°$ (black). **top right**, post-test photographs of the ventral surfaces of the two prototypes. Scale-substrate interface failure is clearly visible in the prototype with $\phi = 90°$. **bottom**, Chronological side profile images of the prototype with $\phi = 90°$ during testing.

5.4 Discussion

Here I discuss the following design aspects of the scale armor of chitons: 1) the interface between the dorsal scales and the girdle, and 2) the shape and imbrication of the dorsal scales. The design principles are compared to those of other natural and man-made scale armors.

5.4.1 The Interface between the Dorsal Scales and the Girdle

The dorsal scales of chitons can be considered to be embedded a depth of h_1 in the soft underlying girdle. While the surface of the non-embedded upper region of each scale is relatively smooth at the micro-scale, the posterior surface in the embedded region is densely covered with small conical bumps approximately 5 μm in height. These bumps increase the interfacial area between the mineralized scales and the inter-scale organic material. The cross-sectional saw-tooth geometry of bumps likely enhances the strength of the interface[174]. I suspect that the bumpiness of the posterior surface likely functions to resist scale pull-out during compression.

Curiously, the conical bumps are absent from the anterior surface of the scales in the embedded region. This suggests a structural response to different loading conditions experienced by the two surfaces. During compression (e.g. during a biting attack), I hypothesize that the "hook" geometry of the scales creates a torque which facilitates scale pull-out on the poster side of each scale, but not on the anterior side (Fig. 5-20).
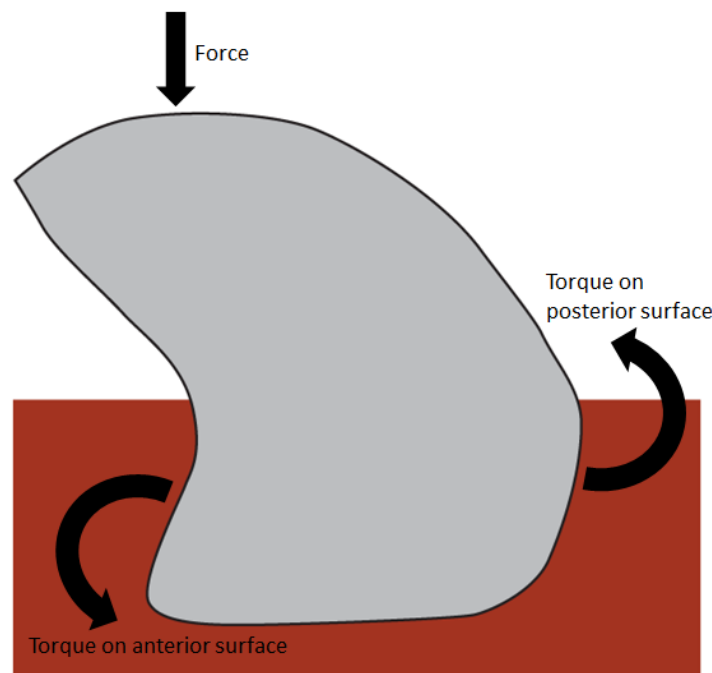
Figure 5-20| Hypothetical mechanical response of an individual dorsal scale to compression.

As previously observed by R. Bullock[71], the base of each scale is slightly concave, which likely functions to increase surface area for attachment to the girdle. In addition, the scales of *R. canariensis* and *L. mertensii* possess a pronounced basal depression, which may further increase the robustness of the girdle-scale interface.

5.4.2 The Shape and Imbrication of the Dorsal Scales

The dorsal scales overlap in a fashion such that the inter-scale organic material is not visible dorsally. This conformation protects the weak interfaces from direct damage during predatory attacks, and is likely a universal design principle of natural scale armor. I am unaware of any segmented natural armor in which the weak interfaces between armor units are exposed externally.

The dorsal girdle scales of chitons bear a striking resemblance to the placoid scales of sharks, which also consist of a diamond-shaped base and a dorsal overlapping hook (referred to as a "crown")[175]. The size and shape of shark scales vary interspecifically, and even across the body of individual animals[175]. As demonstrated in this chapter, the same is true of the dorsal girdle scales of chitons. The size the scales of *R. canariensis* linearly increases towards the proximal margin from 0.005 mm^3 (row 3) to 0.017 mm^3 (row 8) (Fig. 5-12a). In addition, the A_1/A_{total} aspect ratio of the scales increases 25% from row 3 to row 8. Assuming that the inter-scale separation distance, s, proximally increases by about the same factor as the scale volume, A_1/A_{total} will be directly proportional to the amount of scale overlap. Thus, we can reasonably assume that scale overlap increases from the distal to proximal margin of the girdle. The gradation in scale size and imbrication likely reflects different levels of protection and flexibility which are desired in different areas of the armor. At the distal margin, a relatively high degree of flexibility is needed to conform to rough surfaces, so small scales with a relatively low amount of overlap are used. In contrast, at the proximal margin near the body of the chiton, a high degree of protection is desired, so large highly overlapping scales are present. The fish *Polypterus senegalus* also controls the local balance of flexibility and protection by tailoring the size and shape of its scales[176], and it's likely that other scaled animals do as well. Scythians were aware of this body armor design principle well over two thousand years ago. They generally used small scales in areas intended to bend (e.g. elbows and shoulders), and large scales in vital areas of the torso[177]. Japanese samurai armor makers also used several sizes of scales, sometimes arranged in gradients, to construct different protective elements of the armor[178].

The dorsal girdle scales of chitons are arranged such they always overlap (hook) proximally, towards the body. This geometry may function to deflect attacks which are oriented towards the body of the chiton. Designers of ancient human lamellar armor used this design principle. In combat, the majority of stabs (from a spear or sword) to the torso tend to be oriented upward[20]. Thus, the armor units were constructed to overlap upwards, to deflect attacks and prevent penetration between the armor units. However, stabs at the thighs are always oriented downwards, so armor units covering the legs were often inverted, overlapping downwards[20].

Similar to the plates of chitons, the arrangement of the overlapping scales creates an effective uniform thickness of ceramic armor, resulting in spatially homogeneous protection. This feature is also found in the scale[179] and plate[161] armor of fish. Teleost fish scales have been demonstrated to distribute concentrated loads over large areas[179], and I hypothesize that the same is true of the scales of most natural segmented armors, including the dorsal girdle scales of chitons.

The surfaces of the dorsal scales are often ribbed or striated. These surfaces features likely increase resistance to fouling. In a study of 36 mollusk shells, five key surface parameters were identified which were positively correlated to antifouling[180]. In order of importance, the parameters were low fractal dimension, high skewness of roughness and waviness, higher values of isotropy, and lower values of mean surface roughness. Topographies inspired by the ribbed surfaces of shark scales (Shark AF™ surfaces[181]), which are similar in size and shape to chiton scales, have been demonstrated to successfully reduce the attachment of a number of fouling organisms[182].

The flexibility of the 3D printed scale armor inspired by the dorsal girdle scales of *I. contractus* was significantly anisotropic. The resistance to bending of the prototype with the overlapping (hook) direction of the scales initially perpendicular to the loading axis ($\phi = 90°$) was approximately an order of magnitude greater than that of the prototype with the overlapping direction of the scales initially parallel to the loading axis ($\phi = 0°$) (Fig. 5-19). The prototype with $\phi = 90°$ also exhibited interface failure at relatively small displacements, which was not observed in the prototype with $\phi = 0°$. These results are consistent with orientation of the peripheral scale armor relative to the eight central plates. The central plates constrain bending of the girdle about axes parallel to the overlapping direction of the scales. Thus, the bending resistance of the scales about these axes should not significantly affect the overall flexibility of the girdle, so here the scales are rigid to maximize protection. In contrast, bending of the girdle about axes perpendicular to the overlapping direction of the scales is unconstrained by the central plates. Thus, the bending resistance of the scales about these axes is relatively small to increase flexibility, which will help the chiton conform to uneven surfaces.

6 Conclusion

The numerous and diverse types of biological armor systems, developed through the process of evolution, provide engineers with an abundance of design strategies for protection against specific predatory and environmental threats. This thesis investigated the design principles (structure-property-function relationships) of the multifunctional shell of chitons (Mollusca: Polyplacophora). The shell consists of two completely different segmented armors, central plates and peripheral scales, which are seamlessly integrated together in one system. The plates and scales differ in size, degrees of freedom, and level of protection. The plates contain a system of aragonite-based lens eyes, which can form images, enabling spatial vision. Chitons are able to achieve a flexible, multifunctional armor by locally tailoring the size and shape of its armor units and the crystallography of its armor material, aragonite.

Shelled-mollusks face the tough challenge of being both heavily armored and able to sense, signal, and interact with their environments. Certain mollusks (Table 1-1) have solved this problem by integrating optical elements directly into their shells. These unique armors should inspire us to consider integrated design solutions to satisfy the current set of functional requirements of today's standard soldier equipment. Functionally integrated armor may add new functions (e.g. a self-healing ballistic vest), or maintain the current level of functionality while reducing the overall weight or number of devices (e.g. a ballistic vest with an integrated electrical power supply). In the last five years, armor engineers have already begun to explore functional integration. Patents for body armor with integrated electronic components[183,184,185] and batteries[186,187,188] have been applied for or issued. Care should be taken to ensure that functional integration does not decrease mechanical protection.

Significant improvements in the fabrication technology of ballistic ceramics and composites may enable a return of human scale armor. One ballistic scale armor, Dragon Skin® (Pinnacle Armor, Fresno, CA), is already commercially available. The armor consists of imbricating silicon carbide ceramic discs held in place by a high-strength, high-temperature adhesive[189]. Pinnacle Armor claims that Dragon Skin® is flexible[190], although I have been unable to find quantitative measurements of its flexibility. Initial ballistic testing by Pinnacle Armor and independent experts indicated that Dragon Skin® exhibited smaller and more localized damage in comparison to the rigid interceptor body armor (composed of monolithic ceramic and composite backing plates) used by the U.S. Army[190,191]. However, rigorous testing by the U.S. Army indicated that Dragon Skin® suffered failure of the ceramic disk containment adhesive at extreme temperatures, had unreliable penetration resistance under certain

environmental conditions, and was relatively heavy compared to the interceptor body armor[192]. These claims were disputed by Pinnacle Armor[193], and the effectiveness of Dragon Skin® remains controversial.

Compared to the structural complexity of natural scale armor, Dragon Skin® is a relatively simple system. Future designers of ballistic scale armor could ultilize the geometric design principles of the plate and scale armor of chitons, as well as those of other segmented biological exoskeletons. For example, armor units could have joints which could help to improve the robustness of the unit-unit interconnections. Certain joint geometries (e.g. an anti-trapezoidal[194]) may allow an assembly of armor units to maintain a high degree of structural integrity even if polymer adhesives fail. The joints could also be used to tailor an anisotropic bending response, only enabling flexibility in directions it is needed. Spatial variation in joint geometry and/or armor unit size could be employed to create flexibility gradients. For example, the extremities could be covered with small units, which could increase in size towards to the torso. Futhermore, a constant overall thickness of the assembly could be achieved by tailoring the thickness distribution of each unit to correspond to the geometry of unit-unit overlap. This design strategy avoids heterogeneous penetration resistance. Modeling will be necessary to identify the optimal armor unit sizes and shapes to simultaneously generate a desired amount of flexibility and protect against specific ballistic threats[195]. On a smaller length scale, attachment between the ceramic armor units and the polymer adhesive could be strengthened by introducing interfacial geometric interlocking designs[174,196], as seen in the scale armor of chitons.

References

[1] B. David. *Memoirs of the Life, Writings, and Discoveries of Sir Isaac Newton Vol. 2*. Edmonston and Douglas, 1860.

[2] P. Fratzl. Biomimetic materials research: what can we really learn from nature's structural materials? *Journal of the Royal Society Interface* 4(15): 637-642, 2007.

[3] R. Lakes. Materials with structural hierarchy. *Nature* 361(6412): 511-515, 1993.

[4] P. Fratzl and R. Weinkamer. Nature's hierarchical materials. *Progress in Materials Science* 58(8): 1263-1334, 2007.

[5] W. Yang, I. H. Chen, B. Gludovatz, E. A. Zimmermann, R. O. Ritchie, and M. A. Meyers. Natural flexible dermal armor. *Advanced Materials* 25(1): 31-48, 2013.

[6] F. Barthelat, J. E. Rim, and H. D. Espinosa. A review on the structure and mechanical properties of mollusk shells – perspectives on synthetic biomimetic materials. In: B. Bhushan and H. Fuchs (Eds.). *Applied Scanning Probe Methods XIII*, Springer Berlin Heidelberg, pp. 17-44, 2009.

[7] C. Ortiz and M. C. Boyce. Bioinspired structural materials. *Science* 319(5866): 1053-1054, 2008.

[8] S. Kamat, X. Su., R. Ballarini, and A. H. Heuer. Structural basis for the fracture toughness of the shell of the conch *Strombus gigas*. *Nature* 405(6790): 1036-1040, 2000.

[9] B. F. Bruet, J. Song, M. C. Boyce, and C. Ortiz. Materials design principles of ancient fish armour. *Nature Materials* 7(9): 748-756, 2008.

[10] H. D. Espinosa, A. L. Juster, F. J. Latourte, O. Y. Loh, D. Gregoire, and P. D. Zavattieri. Tablet-level origin of toughening in abalone shells and translation to synthetic composite materials. *Nature Communications* 2(173), 2011.

[11] L. Li and C. Ortiz. Pervasive nanoscale deformation twinning as a catalyst for efficient energy dissipation in a bioceramic armor. *Nature Materials*, advanced online publication, 2014.

[12] S. Deville, E. Saiz, R. K. Nalla, and A. P. Tomsia. Freezing as a path to build complex composites. *Science* 311(5760): 515-518, 2006.

[13] L. J. Bonderer, A. R. Studart, and L. J. Gauckler. Bioinspired design and assembly of platelet reinforced polymer films. *Science* 319(5866): 1069-1073, 2008.

[14] A. Browning, C. Ortiz, and M. C. Boyce. Mechanics of composite elasmoid fish scale assemblies and their bioinspired analogues. *Journal of the Mechanical Behavior of Biomedical Materials* 19: 75-86, 2013.

[15] S. H. Reichert. Reverse engineering nature: Design principles for flexible protection inspired by ancient fish armor of Polypteridae. Master's Thesis, Department of Architecture, Massachusetts Institute of Technology, 2010

[16] F. J. Vernerey and F. Barthelat. On the mechanics of fishscale structures. *International Journal of Solids and Structures*. 47(17): 2268-2275.

[17] J. Duro-Royo, K. Zolotovsky, L. Mogas-Soldevila, S. Varshney, N. Oxman, M. C. Boyce, and C. Ortiz. MetaMesh: a hierarchical computational model for design and fabrication of biomimetic armor surfaces. *Computer-Aided Drawing* (accepted).

[18] F. J. Vernerey, K. Musiket, and F. Barthelat. Mechanics of fish skin: a computational approach for bio-inspired flexible composites. *International Journal of Solids and Structures* 51(1): 274-283, 2014.

[19] H. R. Robinson. *Oriental Armour*. Walker and Co., New York, 1967.

[20] T. Dawson. *Armour Never Wearies, Scale and Lamellar Armour in the West, from the Bronze Age to the 19th Century*. The History Press, 2013

[21] R. I. C. Spearman. On the nature of the horny scales of the pangolin. *Journal of the Linnean Society of London* 46(310): 267-273, 1967.

[22] H. W. Greene. *Snakes: the evolution of mystery in nature*. University of California Press, 1997.

[23] A. Warén, S. Bengtson, S. K. Goffredi, and C. L. Van Dover. A hot-vent gastropod with iron sulfide dermal sclerites. *Science* 302(5647): 1007, 2003.

[24] K. Liu and L. Jiang. Bio-inspired design of multiscale structures for function integration. *Nano Today* 6(2): 155-175, 2011.

[25] Y. J. M Bréchet. Architectured materials: an alternative to microstructure control for structural materials design? A possible playground for bio-inspiration? In: P. Fratzl, J. W. C. Dunlop, and R. Weinkamer (Eds.). *Materials Design Inspired by Nature: Function through Inner Architecture*, The Royal Society of Chemistry, 2013.

[26] R. O. Ritchie. The conflicts between strength and toughness. *Nature Materials* 10(11): 817-822, 2011.

[27] L. Li and C. Ortiz. Biological design for simultaneous optical transparency and mechanical robustness in the shell of *Placuna placenta*. *Advanced Materials* 25(16): 2344-2350, 2013.

[28] K. M. Towe. Trilobite eyes: calcified lenses in vivo. *Science* 179(4077): 1007-1009, 1973.

[29] A. Andersson and D.-E. Nilsson. Fine structure and optical properties of an Ostracode (*Crustacea*) nauplius eye. *Protoplasma* 107(3-4): 361-374, 1981.

[30] G. Tanaka. Functional morphology and light-gathering ability of podocopid ostracod eyes and the palaeontological implications. *Zoological Journal of the Linnean Society* 147(1): 97-108, 2006.

[31] J. Aizenberg, A. Tkachenko, S. Weiner, L. Addadi, and G. Hendler. Calcitic microlenses as part of the photoreceptor system in brittlestars. *Nature* 412(6849): 819-822.

[32] D. D. Deheyn and N. G. Wilson. Bioluminescent signals spatially amplified by wavelength-specific diffusion through the shell of a marine snail. *Proceedings of the Royal Society B: Biological Sciences* 278(1715): 2112-2121, 2011.

[33] T. L. Tan, D. Wong, and P. Lee. Iridescence of a shell of mollusk *Haliotis Glabra*. *Optics Express* 12(20): 4847-4854, 2004.

[34] L. Li, S. Kolle, M. Kolle, J. C. Weaver, C. Ortiz, and J. Aizenberg. Functional structural color in the mineralized shell of the blue-rayed limpet, *Patella pellucida* (submitted).

[35] D. R. Lindberg, M. G. Kellogg, and W. E. Hughes. Evidence of light reception through the shell of *Notoacmea persona* (Rathke, 1833) (Archaeogastropoda : Acmaeidae). *The Veliger* 17(4): 383-386, 1975.

[36] D. R. Lindberg and M. G. Kellogg. A note of the structure and pigmentation of the shell of *Notoacmea persona* (Rathke). The Veliger 25(2): 173-174, 1982.

[37] M. E. Watson and P. W. Signor. How a clam builds windows: shell microstructure in Corculum (Bivalvia: Cardiidae). *The Veliger* 28(4): 348-355, 1986.

[38] J. G. Carter and J. A. Schneider. Condensing lenses and shell microstructure in Corculum (Mollusca: Bivalvia). *Journal of Paleontology* 71(1): 56-61, 1997.

[39] D. I. Speiser, D. J. Eernisse, and S. Johnsen. A chiton uses aragonite lenses to form images. *Current Biology* 21(8): 665-670, 2011.

[40] E. Schwabe. A catalogue of recent and fossil chitons (Mollusca: Polyplacophora). Addenda. *Novapex* 6(4): 89-105, 2005.

[41] T. D. Stebbins and D. J. Eernisse. Chitons (Mollusca: Polyplacophora) known from benthic monitoring programs in the Southern California Bight. *The Festivus* 41: 53-100, 2009.

[42] S. S. Puchlaski, D. J. Eernisse, and C. C, Johnson. The effect of sampling bias on the fossil record of the chitons (Mollusca, Polyplacophora)*. *American Malacological Bulletin* 25(1): 87-95, 2008.

[43] B. Runnegar, J. Pojeta Jr., M. E. Taylor, and D. Collins. New species of the Cambrian and Ordovician chitons Matthevia and Chelodes from Wisconsin and Queensland: evidence for the early history of polyplacophoran mollusks. *Journal of Paleontology* 53(6): 1374-1394, 1979.

[44] J. D. Sigwart. Morphological cladistic analysis as a model for character evaluation in primitive living chitons (Polyplacophora, Lepidopleurina)*. *American Malacological Bulletin* 27(1/2): 95-104, 2009.

[45] D. J. Eernisse and P. D. Reynolds. Polyplacophora. In: F. W. Harrison and A. J. Kohn (Eds.). *Microscopic Anatomy of Invertebrates, Volume 5*. Wiley-Liss, New York, pp. 56–110, 1994.

[46] G. E. MacGinitie and N. MacGinitie. Notes on *Cryptochiton stelleri* (Middendorff, 1846). *The Veliger* 11(1): 59-61, 1968.

[47] E. Schwabe and A. Wanninger. Polyplacophora. In: C. F. Sturm, T. A. Pearce, and A. Valdés (Eds.). *The Mollusks: A Guide to Their Study, Collection, and Preservation*, American Malacological Society, pp. 217-228, 2006.

[48] D. J. Eernisse. Chitons. In: M. W. Denny and S. D. Gaines (Eds.). *Encyclopedia of tidepools and rocky shores*. University of California Press, Berkeley, California, pp. 127-133, 2007.

[49] J. Voltzow. The organization of limpet pedal musculature and its evolutionary implications for the Gastropoda. *Malacological Review*, Supplement 4: 273-283, 1988

[50] S. Kuroda, I. Kunita, Y. Tanaka, A. Ishiguro, R. Kobayashi, and T. Nakagaki. Common mechanics of mode switching in locomotion of limbless and legged animals. *Journal of the Royal Society Interface* 11(95): 20140205, 2014.

[51] G. H. Parker. The locomotion of chiton. *Contributions from the Bermuda Biological Station for Research* 31: 1-2, 1914.

[52] M. J. Thorne. Homing in the chiton *Acanthozostera gemmata* (Blainville). *Proceedings of the Royal Society of Queensland* 79(9); 99-108, 1967.

[53] R. C. Newell. *The Biology of Intertidal Animals*, 3rd Edition, Marine Ecological Surveys, 1979.

[54] S. Focardi and G. Chelazzi. Ecological determinants of bioeconomics in three intertidal chitons (Acanthopleura spp.). *Journal of Animal Ecology* 59(1): 347-362, 1990.

[55] H. A. Lowenstam and S. Weiner. *On biomineralization*. Oxford University Press, 1989.

[56] H. A. Lowenstam. Magnetite in denticle capping in recent chitons (Polyplacophora). *Geological Society of America Bulletin* 73(4): 435-438, 1962.

[57] J. C. Weaver, Q. Wang, A. Miserez, A. Tantuccio, R. Stromberg, K. N. Bozhilov, P. Maxwell, R. Nay, S. T. Heier, E. DiMasi, and D. Kisailus. Analysis of an ultra hard magnetic biomineral in chiton radular teeth. *Materials Today* 13(1): 42-52, 2010.

[58] G. W. Marshall, M. Balooch, R. R. Gallagher, S. A. Gansky, and S. J. Marshall. Mechanical properties of the dentinoenamel junction: AFM studies of nanohardness, elastic modulus, and fracture. *Journal of Biomedical Materials Research* 54(1): 87-95, 2001.

[59] E. Schwabe. Illustrated summary of chiton terminology. *Spixiana* 33(2): 171-194, 2010.

[60] F. Neues, A. Ziegler, and M. Epple. The composition of the mineralized cuticle in marine and terrestrial isopods: a comparative study. *CrystEngComm* 9(12): 1245-1251, 2007.

[61] B. D. E. Chatterton and M. Campbell. Enrolling in trilobites: a review and some new characters. *Memoirs of the Association of Australasian Palaeontologists* 15: 103-123, 1993.

[62] M. E. Heath and S. L. Vanderlip. Biology, husbandry, and veterinary care of captive Chinese pangolins (Manis pentadactyla). *Zoo Biology* 7(4): 293-312.

[63] J. Murie. III. On the habits, structure, and relations of the three-banded armadillo (Tolypeutes conurus, Is. Geoff). *Transactions of the Linnean Society of London* 30(1): 71-132, 1874.

[64] P. L. F. N. Mouton, A. F. Flemming, and E. M. Kanga. Grouping behavior, tail-biting behavior and sexual dimorphism in the armadillo lizard (*Cordylus cataphractus*) from South Africa. *Journal of Zoology* 249(1): 1-10, 1999.

[65] R. R. Tenaza. Pangolins rolling away from predation risks. *Journal of Mammalogy* 56(1): 257, 1975.

[66] Scholtz, G. Scarab beetles at the interface of wheel invention in nature and culture? *Contributions to Zoology* 77(3): 139-148, 2008.

[67] C. M. Yonge. On the mantle cavity and its contained organs in the Loricata (Placophora). *Quarterly Journal of Microscopical Science* 81: 367-380, 1939.

[68] D. J. Eernisse, R. N. Clark, and A. Draeger. Polyplacophora. In: J. T. Carlton (Ed.). *Light and Smith Manual: Intertidal Invertebrates from Central California to Oregon, 4th Edition*. University of California Press, Berkeley, California, pp. 701-713, 2007.

[69] B. Dell'Angelo, B. Sabelli, M. Taviani, and A. Bonfitto. New data on the Polyplacophora of Madagascar (Western Indian Ocean) (Mollusca: Polyplacophora). *Archiv für Molluskenkunde* 139(1): 35-43, 2010.

[70] B. Dell'Angelo, S. Gori, L. Baschieri, and A. Bonfitto. Chitons (Mollusca, Polyplacophora) from the Maldive islands. *Zootaxa* 2673: 1-38, 2010.

[71] R. C. Bullock. The genus *Chiton* in the new world (Polyplacophora: Chitonidae). *The Veliger* 31(3): 141-191, 1988.

[72] B. Sirenko. New outlook on the system of chitons (Mollusca: Polyplacophora). *Venus* 65(1-2): 27-49, 2006.

[73] J. M. Serb and D. J. Eernisse. Charting evolution's trajectory: using molluscan eye diversity to understand parallel and convergent evolution. *Evolution: Education and Outreach* 1(4): 439-447, 2008.

[74] M. J. Vendrasco, C. Z. Fernandez, D. J. Eernisse, and B. Runnegar. Aesthete canal morphology in the Mopaliidae (Polyplacophora). *American Malacological Bulletin* 25(1): 51-69, 2008.

[75] A. T. von Middendorff. Beiträge zu einer Malakozoologia Rossica. Chitonen. *Mémoires Sciences Naturelles de l'Académie Impériale des Sciences St. Petersburg* 6(1): 69-215.

[76] W. Marshall. Note sur l'histoire naturelle des chitons. *Archives Neerlandaises des Sciences Exactes et Naturelles* 4: 1-14, 1869.

[77] H. N. Moseley. On the presence of eyes in the shells of certain Chitonidæ, and on the structure of these organs. *Quarterly Journal of Microscopical Science* 25: 37-60, 1885.

[78] M. Nowikoff. Über die rückensinnesorgane der placophoren nebst einigen bemerkungen über die schale derselben. *Zeitschrift für Wissenschaftliche Zoologie* 88: 153-186, 1907.

[79] P. R. Boyle. Rhabdomeric ocellus in a chiton. *Nature* 222: 895-896, 1969.

[80] D. I. Speiser, D. J. Eernisse, and S. Johnsen. A chiton uses aragonite lenses to form images. *Current Biology* 21(8): 665-670, 2011.

[81] S. Reindl, W. Salvenmoser, and G. Haszprunar. Fine structural and immunocytochemical studies on the eyeless aesthetes of *Leptochiton algesirensis*, with comparison to *Leptochiton cancellatus* (Mollusca, Polyplacophora). *Journal of Submicroscopic Cytology and Pathology* 29(1): 135-151, 1997.

[82] J. Blumrich. Das integument der chitonen. *Zeitschrift für Wissenschaftliche Zoologie* 52: 404-476, 1891.

[83] W. J. Crozier and L. B. Arey. On the significance of the reaction to shading in chiton. *The American Journal of Physiology* 46(5): 487-492, 1918.

[84] P. Omelich. The behavioral role and structure of the aesthetes of chitons. *The Veliger* 10(1): 77-82, 1967.

[85] P. R. Boyle. The aesthetes of chitons: 1. Role in the light response of whole animals. *Marine and Freshwater Behavior and Physiology* 1(1-4): 171-184, 1972.

[86] F. P. Fischer. The ultrastructure of the aesthetes in *Lepidopleurus cajetanus* (Polyplacophora: Lepidopleurina). *American Malacological Bulletin* 6(1): 153-159, 1988.

[87] J. E. Randall. *Food habits of reef fishes in the West Indies*. Institute of Marine Sciences, University of Miami, 1967.

[88] C. Cox, J. H. Hunt, W. G. Lyons, and G. E. Davis. Nocturnal foraging of the Caribbean spiny lobster (*Panulirus argus*) on offshore reefs of Florida, USA. *Marine and Freshwater* 48(8): 671-680, 1997.

[89] A. C. F. Silva, S. J. Hawkins, D. M. Boaventura, E. Brewster, and R. C. Thompson. Use of the intertidal zone by mobile predators: influence of wave exposure, tidal phase and elevation on abundance and diet. *Marine Ecology Progress Series* 406: 197-210, 2010.

[90] J. A. Mather. Foraging, feeding and prey remains in the middens of juvenile *Octopus vulgaris* (Mollusca: Cephalopoda). *Journal of Zoology* 224(1): 27-39, 1991.

[91] S. M. Louda. Distribution, movement and diet of the snail *Searlesia dira* in the intertidal community of San Juan Island, Puget Sound, Washington. *Marine Biology* 51(2): 119-131, 1979.

[92] P. K. Dayton, R. J. Rosenthal, L. C. Mahen, and T. Antezana. Population structure and foraging biology of the predaceous Chilean Asteroid *Meyenaster gelatinosus* and the escape biology of its prey. *Marine Biology* 39(4): 361-370, 1977.

[93] M. Hori and T. Noda. An unpredictable indirect effect of algal consumption by gulls on crows. *Ecology* 82(11): 3251-3256, 2001.

[94] M. J. Connors, H. Ehrlich, M. Hog, C. Godeffroy, S. Araya, I. Kallai, D. Gazit, M. Boyce, and C. Ortiz. Three-dimensional structure of the shell plate assembly of the chiton *Tonicella marmorea* and its biomechanical consequences. *Journal of Structural Biology* 177(2): 314-328, 2012.

[95] G. J. Vermeij. *A Natural History of Shells*. Princeton University Press, Princeton, N.J., 1993.

[96] O. B. Bøggild. The shell structure of mollusks. *Det Kongelige Danske Videnskabernes Selskabs Skrifter (Naturvidenskabelig og Mathematisk Afdeling)* 9(2): 235–326, 1930.

[97] J. R. M. Bergenhayn. Die loricaten von Dr. Sixten Bocks pazifik-expedition 1917–1918, mit spezieller berücksichtigung der perinotumbildungen und der schalenstruktur. *Göteborgs Kungliga Vetenskaps-och Vitterhets-Samhälles Handlingar Series B* 1: 1-52, 1930.

[98] J. S. K. Sulanowski. Shell structure of the Polyplacophora (Mollusca). Master's Thesis, Wayne State University, 1972.

[99] W. Haas. Untersuchungenüber die Mikro- und Ultrastruktur der Polyplacophorenschale. *Biomineralisation* 5: 3–52, 1972.

[100] G. F. Laghi and F. Russo. Structtura ed architettura delle piastre di *Chiton olivaceus* Spengler (Polyplacophora, Mollusca). *Bollettinodella Società Paleontologica Italiana* 17: 272-291, 1978.

[101] G. F. Laghi and F. Russo. Struttura ed architettura delle piastre di Lepidopleurus cajetanus (Poli) (Mollusca: Polyplacophora). *Annali dell'Universita di Ferrara, Sezione 9, Science geologiche e paleontologiche* 6: 321-338, 1980.

[102] J. M. Baxter and A. M. Jones. Valve structure and growth in the Chiton *Lepidochitona cinereus* (Polyplacophora: Ischnochitonidae). *Journal of the Marine Biology Association of the United Kingdom* 61(1): 65-78, 1981.

[103] B. Kreusch. Etude Comparée de la Structure et de la Composition Chimique des Formations Squelettiques chez les Mollusques Polyplacophores. Mémoire de Licence en Sciences Zoologiques, Faculté des Sciences, University de Liége, 1981.

[104] J. G. Carter and R. M. Hall. Part 3, Polyplacophora, Scaphopoda, Archaeogastropoda, and Paragastropoda (Mollusca). In: J. G. (Ed.), *Skeletal Biomineralization: Patterns, Processes and Evolutionary Trends, Vol. 2, Atlas and Index*, Van Nostrand Reinhold, New York, pp. 29–31, 49, pls. 122–125, 1990.

[105] D. R. Currie. Aesthete channel morphology in three species of Australian chitons (Mollusca: Polyplacophora). *Journal of the Malacological Society of Australia* 13(1): 3-14, 1992.

[106] D. Chen. Microstructure and element composition of the shell plates of *Liolophura japonica*. *Wuhan University Journal of Natural Sciences*, 15(2): 176-184, 2010.

[107] V. Cornish and P. F. Kendall. IV. —On the mineralogical constitution of calcareous organisms. *Geological Magazine (Decade III)* 5(2): 66-73, 1888.

[108] H. Yao, M. Dao, T. Imholt, J. Huang, K. Wheeler, A. Bonilla, S. Suresh, and C. Ortiz. Protection mechanisms of the iron-plated armor of a deep-sea hydrothermal vent gastropod. Proceedings of the National Academy of Sciences 107(3): 987-992, 2010.

[109] J. D. Taylor and M. Layman. The mechanical properties of bivalve (Mollusca) shell structures. *Palaetonology* 15(1): 73-87, 1972.

[110] J. G. Carter and G. R. Clark II. Classification and phylogenetic significance of molluscan shell microstructure. In: D. J. Bottjer, C. S. Hickman, and P. D. Ward (organizers), and T. W. Broadhead (Ed.). *Mollusks: Notes for a Short Course*. University of Tennessee Department of Geological Sciences, Studies in Geology 13, Knoxville, TN, USA, pp. 50–71, 1985.

[111] C. M. Zaremba, D. E. Morse, S. Mann, P. K. Hansma, and G. D. Stucky. Aragonite-hydroxyapatite conversion in Gastropod (Abalone) Nacre. *Chemistry of Materials* 10: 3813-3824, 1998.

[112] N. M. Neves J. F. Mano. Structure/mechanical behavior relationships in crossed-lamellar sea shells. *Materials Science & Engineering: C* 25(2): 113-118, 2005.

[113] P. A. C. Gane, C. J. Ridgway, E. Lehtinen, R. Valiullin, I. Furó, J. Schoelkopf, H. Paulapuro, and J. Daicic. Comparison of NMR cryoporometry, mercury intrusion porosimetry, and DSC thermoporosimetry in characterizing pore size distributions of compressed finely ground calcium carbonate structures. *Industrial & Engineering Chemistry Research* 43(24): 7920-7927, 2004.

[114] H. Ehrlich, M. Maldonado, K.-D. Spindler, C. Eckert, T. Hanke, R. Born, C. Goebel, P. Simon, S. Heinemann, and H. Worch. First evidence of chitin as a component of the skeletal fibers of marine sponges. Part I. Verongidae (Demospongia: Porifera). *Journal of Experimental Zoology Part B: Molecular and Developmental Evolution* 308(4): 347-356, 2007.

[115] E. Brunner, H. Ehrlich, P. Schupp, R. Hedrich, S. Hunoldt, M. Kammer, S. Machill, S. Paasch, V. V. Bazhenov, D. V. Kurek, T. Arnold, S. Brockmann, M. Ruhnow, and R. Born. Chitin-based scaffolds are an integral part of the skeleton of the marine Demosponge *Ianthella basta*. *Journal of Structural Biology* 168(3): 539-547, 2009.

[116] E. Poulicek and B. Kreusch. Evolutionary trends in the skeletal structures of the Polyplacophora. *Proceedings of the Eighth International Malacological Congress (Budapest, Hungary)*, 207-212, 1983.

[117] J. D. Currey and A. J. Kohn. Fracture in the crossed-lamellar structure of *Conus* shells. *Journal of Materials Science* 11(9): 1615-1623, 1976.

[118] J. D. Taylor and D. G. Reid. Shell microstructure and mineralogy of the Littorinidae: ecological and evolutionary significance. *Hydrobiologia* 193(1): 199-215, 1990.

[119] N. V. Wilmot, D. J. Barber, J. D. Taylor, and A. L. Graham. Electron microscopy of molluscan crossed-lamellar microstructure. *Philosophical Transactions of the Royal Society of London. Series B: Biological Sciences* 337(1279): 21-35, 1992.

[120] T. Furuhashi, A. Beran, M. Blazso, Z. Czegeny, C. Schwarzinger, and G. Steiner. Pyrolysis GC/MS and IR spectroscopy in chitin analysis of molluscan shells. *Bioscience, Biotechnology, and Biochemistry* 73(1): 93-103, 2009.

[121] H. Ehrlich. *Biological Materials of Marine Origin*. Heidelberg, Springer, 2010.

[122] H. Ehrlich, M. Ilan, M. Maldonado, G. Muricy, G. Bavestrello, Z. Kljajic, J. L. Carballo, S. Schiaparelli, A. Ereskovsky, P. Schupp, R. Born, H. Worch, V. V. Bazhenov, D. Kurek, V. Varlamov, D. Vyalikh, K. Kummer, V. V. Sivkov, S. L. Molodtsov, H. Meissner, G. Richter, E. Steck, W. Richter, S. Hunoldt, M. Kammer, S. Paasch, V. Krasokhin, G. Patzke, and E. Brunner. Three-dimensional chitin-based scaffolds from Verongida sponges (Demospongiae: Porifera). Part 1. Isolation and identification of chitin. *International Journal of Biological Macromolecules* 47(2): 132-140, 2010.

[123] K. Treves, W. Traub, S. Weiner, and L. Addadi. Aragonite formation in the chiton (Mollusca) girdle. *Helvetica Chimica Acta* 86(4): 1101-1112, 2003.

[124] H. Ehrlich. Chitin and collagen as universal and alternative templates in biomineralization. *International Geology Review* 52(7-8): 661-699, 2010.

[125] L. Wang, J. Song, C. Ortiz, and M. C. Boyce. Anisotropic design of a multilayered biological exoskeleton. *Journal of Materials Research* 24(12): 3477-3494, 2009.

[126] M. Teleford. Domes, arches and urchins: the skeletal architecture of echinoids (Echinodermata). *Zoomorphology* 105(2): 114-124, 1985.

[127] L. T. Kuhn-Spearing, H. Kessler, E. Chateau, R. Ballarini, A. H. Heuer, and S. M. Spearing. Fracture mechanisms of the *Strombus gigas* conch shell: implications for the design of brittle laminates. *Journal of Materials Science* 31(24): 6583-6594, 1996.

[128] S. Kamat, X. Su, R. Ballarini, A. H. Heuer. Structural basis for the fracture toughness of the shell of the conch *Strombus gigas*. *Nature* 405(6790): 1036-1040, 2000.

[129] S. Kamat, H. Kessler, R. Ballarini, M. Nassirou, and A. H. Heuer. Fracture mechanisms of the *Strombus gigas* conch shell: II-micromechanics analysis of multiple channel cracking and large-scale crack bridging. *Acta Materialia* 52(8): 2395-2406, 2004.

[130] F. Barthelat, H. Tang, P. D. Zavattieri, C.-M. Li, and H. D. Espinosa. On the mechanics of mother-of-pearl: a key feature in the material hierarchical structure. *Journal of the Mechanics and Physics of Solids* 55(2): 306-337, 2007.

[131] W. Haas. Evolution of calcareous hardparts in primitive mollusks. *Malacologia* 21(1-2): 403-418, 1981.

[132] J. P. Thomas and M. A. Qidwai. The design and application of multifunctional structure-battery materials systems. *JOM: Journal of the Minerals, Metals and Materials Society* 57(3): 18-24, 2005.

[133] J. Liu, C. Xie, X. Dai, L. Jin, W. Zhou, and C. M. Lieber. Multifunctional three-dimensional macroporous nanoelectronic networks for smart materials. *Proceedings of the National Academy of Sciences* 110(17): 6694-6699.

[134] M. D. Hager, P. Greil, C. Leyens, S. van der Zwaag, and U. S. Schubert. Self-Healing Materials. *Advanced Materials* 22(47): 5424-5430, 2010.

[135] W. L. Bragg. The refractive indices of calcite and aragonite. *Proceedings of the Royal Society of London. Series A, Containing Papers of a Mathematical and Physical Character* 105(732): 370-386, 1924.

[136] C. C. Davis. *Lasers and electro-optics: fundamentals and engineering*. Cambridge University Press, 1996.

[137] H. F. de Carvalho and B. de Campos Vidal. Polarized microscopy study of an antennal sensillum of *Triatoma infestans*: an ordered distribution of chitin fibrils and associated components. *Comptes rendus de l'Academie des sciences. Serie III, Sciences de la vie* 319(1): 33-38, 1996.

[138] H. L. Merten and G. L. Bachman. Stabilized amorphous calcium carbonate. U.S. Patent No. 4,237,147, issued on December 2, 1980.

[139] K. Lee, W. Wagermaier, A. Masic, K. P. Kommareddy, M. Bennet, I. Manjubala, S.-W. Lee, S. B. Park, H. Cölfen, and P. Fratzl. Self-assembly of amorphous calcium carbonate microlens arrays. *Nature Communications* 3(725), 2012.

[140] D.-E. Nilsson, L. Gislén, M. M. Coates, C. Skogh, and A. Garm. Advanced optics in a jellyfish eye. *Nature* 435(7039): 201-205, 2005.

[141] E. L. Dereniak and T. D. Dereniak. *Geometrical and Trigonometric Optics*. Cambridge University Press, 2008.

[142] M. F. and D.-E. Nilsson. *Animal Eyes*. Oxford University Press, 2012.

[143] E. J. Warrant and D.-E. Nilsson. Absorption of white light in photoreceptors. *Vision Research* 38(2): 195-207, 1988.

[144] P. R. Boyle. Fine structure of the eyes of Onithochiton neglectus (Mollusca: Polyplacophora). *Zeitschrift für Zellforschung und Mikroskopische Anatomie* 102(3): 313-332, 1969.

[145] M. S. Bruno, S. N. Barnes, and T. H. Goldsmith. The visual pigment and visual cycle of the lobster, *Homarus*. *Journal of Comparative Physiology A* 120(2): 123-142, 1977.

[146] W. C. Oliver and G. M. Pharr. An improved technique for determining hardness and elastic modulus using load and displacement sensing indentation experiments. *Journal of Materials Research* 7(6): 1564-1583, 1992.

[147] L. Addadi, S. Raz, and S. Weiner. Taking advantage of disorder: amorphous calcium carbonate and its role in biomineralization. *Advanced Materials* 15(12): 959-970, 2003.

[148] R. D. Fernald. The optical system of fishes. In: R. Douglas and M. Djamgoz (Eds.). *The Visual System of Fish*. Chapman and Hall, pp. 45-61, 1990.

[149] L. R. Brooker. Revision of *Acanthopleura* Guilding, 1829 (Mollusca: Polyplacophora) based on light and electron microscopy. PhD Thesis, Murdoch University, Western Australia, 2003.

[150] O. Shoval, H. Sheftel, G. Shinar, Y. Hart, O. Ramote, A. Mayo, E. Dekel, K. Kavanagh, and U. Alon. Evolutionary trade-offs, Pareto optimality, and the geometry of phenotype space. *Science* 336(6085): 1157-1160, 2012.

[151] D.-E. Nilsson. Eyes as optical alarm systems in fan worms and ark clams. *Philosophical Transactions of the Royal Society B: Biological Sciences* 346(1316): 195-212, 1994.

[152] L. B. Arey and W. J. Crozier. The sensory responses of chiton. *Journal of Experimental Zoology* 29(2): 157-260, 1919.

[153] G. Haszprunar and A. Wanninger. Molluscan muscle systems in development and evolution. *Journal of Zoological Systematics and Evolutionary Research* 38: 157-163, 2000.

[154] K. G. Wingstrand. On the anatomy and relationships of recent Monoplacophora. *Galathea report* 16: 7-94, 1985.

[155] T. Arciszewski and J. Cornell. "Bio-inspiration: Learning creative design principia." In: F. C. Ian (Ed.). *Intelligent Computing in Engineering and Architecture*. Springer Berlin Heidelberg, pp. 32-53, 2006.

[156] P. Kaas and R. A. Van Belle. *Monograph of Living Chitons (Mollusca: Polyplacophora), Vol. 2, Suborder Ischnochitonina, Ischnochitonidae: Schizoplacinae, Callochitoninae and Lepidochitoninae*. E.J. Brill, Leiden, 1985.

[157] C. A. Schneider, W. S. Rasband, and K. W. Eliceiri. NIH Image to ImageJ: 25 years of image analysis. *Nature Methods* 9(7): 671-675, 2012.

[158] M. L. Bouxsein, S. K. Boyd, B. A. Christiansen, R. E. Guldberg, K. J. Jepsen, and R. Müller. Guidelines for assessment of bone microstructure in rodents using micro- computed tomography. *Journal of Bone and Mineral Research* 25(7): 1468-1486, 2010.

[159] V. Pratt. Direct least-squares fitting of algebraic surfaces. *Computer Graphics* 21(4): 145-152, 1987.

[160] P. D. Langer. Some aspects of the biology of three Northwestern Atlantic Chitons: *Tonicella rubra*, *Tonicella marmorea*, and *Ischnochiton albus* (Mollusca: Polyplacophora). PhD Thesis, Department of Zoology, University of New Hampshire, 1978.

[161] J. Song, S. Reichert, I. Kallai, D. Gazit, M. Wund, M. C. Boyce, and C. Ortiz. Quantitative microstructural studies of the armor of the marine threespine stickleback (*Gasterosteus aculeatus*). *Journal of Structural Biology* 171(3): 318-331, 2010.

[162] D. M. Pearson. Functional aspects of the integument in polypterid fishes. *Zoological Journal of the Linnean Society* 72(1): 93-106, 1981.

[163] K. Takahashi. The ball-and-socket joint of the sea-urchin spine: geometry and its functional implications. *Journal of the Faculty of Science, the University of Tokyo, Section IV, Zoology* 11: 131-135, 1967.

[164] J. C. Town. Aspects of the biology of *Astrostole scabra* (Hutton, 1872). PhD Thesis, Department of Zoology, University of Canterbury, 1979.

[165] creu007. Moving Chiton Video. Uploaded on March 22, 2011. Retrieved from https://www.youtube.com/watch?v=fsA1gJPy6sc. Accessed on April 16, 2014.

[166] VideotecaFaunaPR. Quitón (Chiton tuberculatus) - Chiton. Uploaded on May 12, 2013. Retrieved from https://www.youtube.com/watch?v=yRqLsR6rKO8. Accessed on April 16, 2014.

[167] M. H. B. O'Neill. The genus *Rhyssoplax* Thiele in the New Zealand region (Mollusca: Polyplacophora). *New Zealand Journal of Zoology* 16(1): 81-92, 1989.

[168] E. Schwabe and P. Lozouet. Chitons (Mollusca, Polyplacophora) from Rapa, the southernmost island of Poynesia. *Zoosystema* 28(3): 617-633.

[169] T. Ørvig. Phylogeny of tooth tissues: Evolution of some calcified tissues in early vertebrates. In: A. E. W. Miles (Ed.). *Structural and Chemical Organization of Teeth, Vol. 1*. Academic Press, New York, pp. 45-100, 1967.

[170] J. D. Currey, J. D. Mechanical properties and adaptations of some less familiar bony tissues. *Journal of the Mechanical Behavior of Biomedical Materials* 3(5): 357-372, 2010.

[171] A. M. Jakovleva. Shell-bearing Mollusks (Loricata) of the seas of the U.S.S.R. In: *Keys to the Fauna of the U.S.S.R.* 45, Zoological Insitute of the Academy of Sciences of the U.S.S.R., pp. 1-127, 1952. Translated from Russian to English by the Israel Program for Scientific Translations, 1965.

[172] P. Kaas and R. A. Van Belle. *Monograph of Living Chitons (Mollusca: Polyplacophora), Vol. 1, Order Neoloricata: Lepidopleurina*. E.J. Brill, Leiden, 1985.

[173] E. Lin, Y. Li, C. Ortiz, and M. C. Boyce. 3D printed, bio-inspired prototypes and analytical models for structured suture interfaces with geometrically-tuned deformation and failure behavior (in review).

[174] Y. Zhang, H. Yao, C. Ortiz, J. Xu, and M. Dao. Bio-inspired interfacial strengthening strategy through geometrically interlocking designs. *Journal of the Mechanical Behavior of Biomedical Materials* 15: 70-77, 2012.

[175] P. Motta, M. L. Habegge, A. Lang, R. Hueter, and J. Davis. Scale morphology and flexibility in the shortfin mako *Isurus oxyrinchus* and the blacktip shark *Carcharinus limbatus*. *Journal of Morphology* 273(10): 1096-1110, 2012.

[176] S. Varshney, J. Song, Y. Li, K. Zolotovsky, S. Reichert, M. C. Boyce, and C. Ortiz. Tailored 2D and 3D morphometric diversity of a natural armor assembly investigated by continuum strain analysis (in preparation).

[177] E. V. Cerenko, A. McBride, and M. V. Gorelik. *The Scythians, 700-300 BC*, Men-at-Arms Series, 137, Osprey Publishing, 1983.

[178] A. J. Bryant. *Early Samurai AD 200-1500*. Osprey Publishing, 1991.

[179] D. Zhu, L, Szewciw, F. Vernerey, and F. Barthelat. Puncture resistance of the scaled skin from striped bass: Collective mechanisms and inspiration for new flexible armor designs. *Journal of the Behavior of Biomedical Materials* 24: 30-40, 2013.

[180] A. J. Scardino, D. Hudleston, Z. Peng, N. A. Paul, and R. de Nys. Biomimetic characterization of key surface parameters for the development of fouling resistant materials. *Biofouling* 25(1): 83-93, 2009.

[181] M. L. Carman, T. G. Estes, A. W. Feinberg, J. F. Schumacher, W. Wilkerson, L. H. Wilson, M. E. Callow, J. A. Callow, and A. B. Brennan. *Biofouling* 22(1): 11-21, 2006.

[182] C. M. Kirschner and A. B. Brennan. Bio-inspired antifouling strategies. *Annual Review of Materials Research* 42: 211-229, 2012.

[183] M. McElroy, E. Hoenes, L. Sengupta, S. Sengupta, V. Horvatich, A. McNeish, and J. W. Coltman III. Body armor plate having integrated electronic modules. U.S. Patent No. 7,805,767 B2, issued on October 5, 2010.

[184] F. O. Fortson, K. E. Johnson, J. D. Jorge Jr., L. A. Schwope, and A. K. Gupta. Smart Armor. U.S. Patent Application Publication No. US 2009/0027229 A1, published on January 29, 2009.

[185] A. Balzano. Safety vest assembly including a high reliability communication system. U.S. Patent Application Publication No. US 2012/0174299 A1, published on July 12, 2012.

[186] G. F. Walquist, C. L. Horvath, T. J. Imholt, and H. Barteld VanRees. Method and apparatus for armor having integrated battery power. U.S. Patent Application Publication No. US 2013/0084473 A1, published on April 4, 2013.

[187] D. J. Vavrick and N. V. Nechitailo. Body armor with electrical power supply. U.S. Patent No. 7,921,757 B1, issued on April 12, 2011.

[188] M. McElroy, V. Horvatich, J. W. Coltman III, D. Furth, K. Sego Jr., K. L. Von Der Ahe, and E. Hoenes. Portable electrical power source for incorporation with an armored garment. U.S. Patent No. 8,502,506 B2, issued on August 6, 2013.

[189] D. Crane. Dragon skin armor passes more tests: Dr. Gary Roberts and 'test lab' video. *DefenseReview.com*, October 20, 2006. http://www.defensereview.com/dragon-skin-armor-passes-more-tests-dr-gary-roberts-and-test-lab-video/. Accessed on April 25, 2014.

[190] J. Wells, N. Rupert, and M. Neal. Impact damage analysis in a level III flexible body armor vest using XCT diagnostics. In: J. J. Swab (Ed.). *Advances in Ceramic Armor V*, John Wiley & Sons, Inc., Hoboken, New Jersey, pp. 171-179, 2010.

[191] A. Ciralsky, L. Myers. Are U.S. soldiers wearing the best body armor? NBC News Investigation, May 20, 2007. Retrieved from http://www.nbcnews.com/id/18720550/ns/nbc_nightly_news_with_brian_williams-nbc_news_investigates/t/are-us-soldiers-wearing-best-body-armor/#.U1r_cPldWSo. Accessed on April 25, 2014.

[192] Project manager solider equipment briefing on the May 2006 evaluation of Pinnacle Armor SOV 3000 "Dragon Skin". Retrieved from http://www.professionalsoldiers.com/files/dragon_skin_release_000121may07.pdf. Accessed on April 25, 2014.

[193] Information paper. Subject: Pinnacle Body Armor – SOV/Dragon Skin™ (Flexible Body Armor), October 24, 2006. Retrieved from http://www.defensetech.org/archives/rebuttal%20to%20Unofficial%20Army%20Info%20Paper%20_8%20Mar%2007_.pdf. Accessed on April 25, 2014.

[194] Y. Li, C. Ortiz, and M. C. Boyce. A generalized mechanical model for suture interfaces of arbitrary geometry. *Journal of the Mechanics and Physics of Solids* 61(4): 1144-1167, 2013.

[195] P. J. Hogg. Composites in armor. *Science* 314(5802): 1100-1101, 2006.

[196] Y. Li, C. Ortiz, and M. C. Boyce. Stiffness and strength of suture joints in nature. *Physical Review E* 84(6): 062904, 2011.